Indirect Exchange Coupling in Sputtered Magnetic Multilayers.

Christopher Hugh Marrows

Submitted in accordance with the requirements of the degree of Doctor of Philosophy.

The University of Leeds
Department of Physics and Astronomy
September 1997

The candidate confirms that the work submitted is his own and that appropriate credit has been given where reference has been made to the work of others.

ABSTRACT

This thesis describes the design, construction, and use of a sputter deposition facility at the University of Leeds for the growth of magnetic multilayer samples. Now completed, the machine is a UHV sputtering facility, capable of growing up to 15 samples of arbitrary complexity under computer control in a single vacuum cycle. The system currently has five sputter targets.

The system was used to grow Co/Cu multilayers. It was found that the level of residual gas in the chamber is of primary importance in determining the final quality of the samples. A good vacuum is required to achieve good antiferromagnetic coupling between adjacent Co layers in the multilayer stack. Consequentially the giant magnetoresistance of such samples is very high. A poor vacuum leads to poor coupling between Co layers, and the magnetoresistance of such samples is minimal.

When grown under clean conditions the giant magnetoresistance of the Co/Cu multilayers was very high - as much as 75% at room temperature, rising to 130% at 4.2K. Coupling oscillations as the Cu spacer thickness was varied were strong, whilst none were detected as a function of Co thickness.

It was found that the Cu spacer layer was the part of the multilayer where the effects of damage by residual gases were most severe, and that damage to this area could cause biquadratic coupling. This form of the coupling arranges spins in adjacent layers at 90° to one another, rather than antiparallel, reducing the giant magnetoresistance response of the sample. The saturation magnetisation, bilinear and biquadratic coupling energies of 180° and 90° coupled samples were measured. These three quantities were found to scale as a function of temperature.

ACKNOWLEDGEMENTS

Modern science is very much a team effort - a full list of all the people who have assisted me over the previous three years is long. I owe a debt of gratitude to my PhD supervisor Dr Bryan Hickey. Invaluable technical support and advice was received from John Turton and Leigh Harris. Trevor Haynes, Steve Caddick, Trevor Sitlinton, Mansukh Patel and Andrew Price all also built some part of the sputtering machine.

I was fortunate to spent two months working at INESC in Lisbon, Portugal, learning the basics of sputtering GMR structures – thanks are due to Prof. Paulo Freitas and everyone at INESC for making me feel welcome.

Christian Mény and M Malinowska at ICPMS-GEMME in Strasbourg performed the NMR measurements and analysis, which will be found in Chapter 4 of this thesis. Christian also helped me with the initial stages of the sputterer design during his time at Leeds.

X-ray scans performed at SRS Daresbury on samples I had grown are detailed in part in Chapter 4, and these measurements and much of quantitative analysis was performed by Tom Hase and Prof. Bryan Tanner of The University of Durham. A number of their results have had to be included here as they have an important bearing on the work presented.

In spring of this year I visited Michigan State University as a guest of Prof. Bill Pratt Jr. I performed the SQUID magnetometer measurements presented in Chapter 5 during my stay , assisted by Reza Loloee.

On a more personal note, I must also thank all my family, and especially my parents, who have supported me in every way throughout my University career. I am also indebted to my girlfriend Christine, who never fails to remind me that there is more to life than physics alone.

I was supported over these three years by a University of Leeds Henry Ellison scholarship.

CONTENTS

1. INTRODUCTION

1.1 ARTIFICIAL MAGNETIC NANOSTRUCTURES

Miniaturisation has been the dominant trend of modern microelectronics. Each new generation of devices has performed better than the last, and has been physically smaller than previous generations, as well as being both faster and cheaper.

Moore's law, named for Intel co-founder Gordon Moore, states that the storage capacity of memory chips doubles every eighteen months, first proposed in 1965. This growth rate still holds good today. A similarly rapid and exponential growth has occurred in the field of long-term data storage. Ten years ago a 50Mb capacity hard drive was considered more than any user would ever require in a PC. Today with the advent of graphical computing and multimedia such a drive would not even be able to store the computer's operating system. Hard disk capacities have improved by over an order of magnitude in the previous five years. Yet the physical size has remained unchanged, the 3½" hard disk remains standard.

The explosive rate of growth in storage density was made possible by the introduction of a new technology, that of the magnetoresistive head. Prior to 1990 all data were read from hard disks and tapes with inductive heads, where the head flying over the magnetised medium induces emfs into the pickup coil which is the readback part of the head. These emfs are of course proportional to the velocity of the disk below the head. As the physical length and breadth of the written bits becomes smaller and smaller, the magnetic fields become proportionally weaker, and the disk must spin faster to achieve the same output signal. Towards the centre of the disk the problem is particularly acute, as the angular velocity of the spinning disk must be very high to achieve a usable linear velocity.

Magnetoresistive heads bypass this problem by reading back the signal

directly, rather than it's derivative with time. A magnetoresistive element is a small piece of material whose electrical resistance varies depending on the applied magnetic field. It is thus a natural sensor. Modern hard disks incorporate such heads based on a physical principle called the anisotropic magnetoresistance (AMR), where the angle between current and magnetisation in the material determines the resistance. This effect was discovered in 1857 by William Thomson, who later went on to become Lord Kelvin[1]. This magnetisation direction may be moved around by the application of an external field. The introduction of this technology to generally available hard disks in 1990 by IBM boosted the annual growth rate in storage density from 30% to 60%. These new heads are made from thin films of ferromagnetic metal, most typically permalloy. In turn these AMR heads will be replaced by spin-valve heads utilising the giant magnetoresistance (GMR)[2], which will allow higher still storage densities.

Yet the interest in magnetic systems is not purely technological. The fundamental study of the low-dimensional and nanostructured magnetic materials used in such devices, has also proved rich in new physics, as well as allowing investigation of effects which have been neglected or described only by assumptions in the past. The development of UHV conditions for the growth of samples has allowed good quality ultrathin films and even monolayers of magnetic materials to be prepared for study. Since the earliest studies of one- and two-dimensional magnetic systems[3] focusing on inorganic magnetic crystals containing planes or lines of spins, these UHV techniques have been in the ascendant. The discovery of the giant magnetoresistance in 1988[4], sparked off an intense world-wide research effort into the magnetotransport properties of such artificial structures.

Such a very thin film is of course almost entirely surface, and surface effects may be expected to dominate the physical properties. Such effects as surface anisotropy and indirect exchange coupling have also received much experimental[5] and theoretical[6] attention. Recent magnetism conferences have been dominated by thin film studies, and the Materials Research

Society has run special symposia on thin-film magnetism and published the proceedings. The first few years of this explosion of research are documented in a pair of books edited by Bland and Heinrich[7].

1.2 THE GIANT MAGNETORESISTANCE

The principle new technological application of such structures relies on the giant magnetoresistance phenomenon. A brief explanation of this effect is in order. Very large magnetoresistances were observed in the 1960s and 1960s in iron whiskers at cryogenic temperatures[8]. Fields as low as 10mT could decrease the resistance by up to an order of magnitude. As the field is applied the domain walls are swept out. Domain walls are sources of electron scattering, and hence make a contribution to the electrical resistivity of the material. Only at very low temperatures in a single crystal iron whisker are other sources of scattering sufficiently small to allow the domain wall contribution to be so easily detected. However we can see that the lower resistivity in a field is **due to the increased magnetic order in this case.**

The giant magnetoresistance is also a negative effect - the application of a field reduces the resistivity, and again it relies on increased magnetic order in a field. It requires that the material be formed from magnetic elements separated from each other by non-magnetic conductors - most commonly noble metals like Cu and Ag, although just about every non-magnetic transition metal has been used at one time or another. For best effect though the spacer should itself be as good as possible a conductor. Such materials are usually formed from thin layers of the different materials, although granular systems, consisting of magnetic clusters embedded in a host matrix also display this property.

The mechanism by which the magnetoresistance works is best understood by a simple resistor network model. The essential feature is that the likelihood of an electron being scattered in a magnetic material depends on that electron's spin relative to the material's magnetisation. This is due to the exchange splitting of the d-bands in transition metals which are

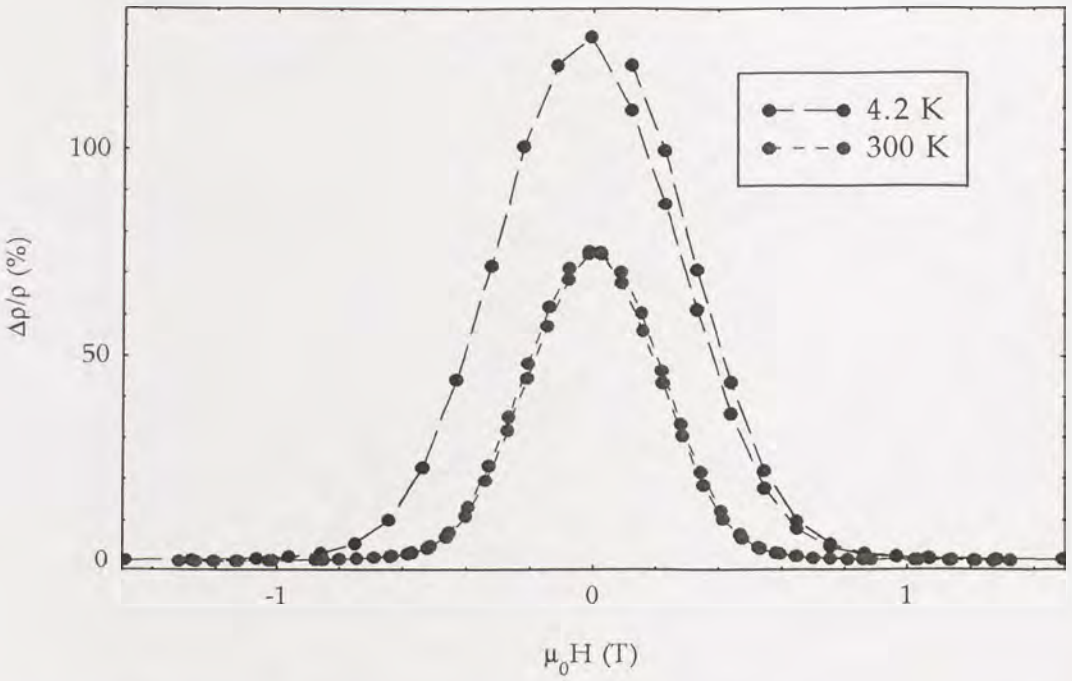

Figure 1.1 The giant magnetoresistance of a Co/Cu multilayer grown in the sputtering facility at the University of Leeds measured at room and helium temperature. The magnetoresistance is negative, the resistance drops sharply as the field is applied until the system saturates. The GMR ratio is normalised to the saturated resistivity of the sample, and the 4.2 K response is much larger as this value is reduced on cooling.

ferromagnetic - the majority spin band is more predominantly s-like at the Fermi level, and hence more conductive, as a consequence of Fermi's golden rule. If little or no spin-flip scattering is assumed then two parallel spin channels of conduction exist, with different resistivities.

The smallest possible unit of a GMR material is two pieces of magnetic metal, which are closely separated by a spacer material. They may take up configurations where the magnetisation vectors are anti-parallel, but may be made parallel by the application of a field. When the layers are aligned parallel the majority spin electrons are able to pass through both pieces of magnetic material with ease, and so provide a low resistance path for current, and the macroscopic resistance is low. When the field is removed, the layers will be able to return their anti-parallel state, and now neither spin

of electron enjoys easy passage through both pieces of magnetic material - the macroscopic resistance is high. One may consider this as a kind of polarisation experiment, where the first ferromagnet spin-polarises the electrons carrying the current - only if the second ferromagnet is aligned can the polarised current easily pass through. For well chosen and exactly crafted systems the fractional change in resistivity can be very large, see Fig 1.1. The fractional change or *GMR ratio* (often referred to as simply the GMR) is conventionally defined as the ratio of the change in resistance to the resistance in the saturated state. The value is normalised to the saturated state because that state is well defined - in real systems the anti-parallel state may well not be perfectly achieved.

This treatment of the GMR naturally skims over a number of the more subtle or detailed points. A good primer on the GMR effect is given by White[9], and a more detailed review by Dieny[10].

1.3 INDIRECT EXCHANGE COUPLING

This antiparallel state may arise by a number of mechanisms, one of which may well be considered the other most remarkable property of magnetic multilayer systems. This is oscillatory indirect exchange coupling, predicted in the 1960s, but only first observed in the late 1980s. When two magnetic layers are separated by very thin spacers then electrons may be shared between them, and the exchange interaction which couples spins together to allow ordinary ferromagnetism allows the two layers to become coupled. The coupling decays rapidly as the thickness of the spacer increases, and is negligible for thicknesses greater than about 50Å. It is strongest for spacers which are about 10Å thick, and successfully growing such very thin layers which are smooth on an atomic scale and without discontinuities is a severe challenge to thin film growth technology.

In fact this interlayer coupling is a form of *superexchange*, where a spin in one layer interacts via direct exchange with an itinerant electron, which then goes on into the second magnetic layer and interacts with another spin

there. The two spins are thus indirectly coupled - and the sense of this coupling oscillates with the spacer layer thickness. The Hamiltonian of the interaction may be written in the usual Heisenberg form, as being proportional to the scalar product of two unit vectors parallel to the two magnetisations. Thus for certain spacer thickness ranges the magnetic layers will naturally align in the antiparallel high resistance state. Application of a sufficiently large field will align the layers parallel again, and the kind of GMR curve seen in Fig 1.1 will be observed.

The physics of this oscillatory coupling is still not fully resolved. Many of its properties are determined by the properties of the spacer layer. It appears to be a universal phenomenon, exhibited by almost every kind spacer material, be it metal, semiconductor or insulator. The whole of Chapter 3 is dedicated to a discussion of various models of this indirect coupling.

1.4 THIS THESIS

The work described in this thesis was performed with one main goal in mind. A large old sputtering machine owned by the physics department would be renovated and improved to a state where it could be used to make magnetic multilayer samples of the kind already being grown in the molecular beam epitaxy (MBE) machine installed in the department in 1990. However the machine would be able to grow a large number of samples in a single vacuum cycle, and be fully automated. This work is described in Chapter 2, along with a brief description of the various experimental techniques used to characterise the samples.

The level of base pressure was found to be of crucial importance in growing high quality Co/Cu multilayer samples. This type of sample has been widely studied, and is particularly suited to sputter deposition. In a very clean growth environment very large magnetoresistances could be achieved, as shown in Fig1.1. For small amounts of residual gas the GMR would drop markedly, and it was found to be driven by much poorer

antiferromagnetic coupling between the layers. A review of the various theoretical models of this coupling is given in Chapter 3, as well as a description of the numerical model used to extract quantitative information about the coupling.

Investigations into the microstructure of the samples are described in Chapter 4, as we attempted to discover what morphological changes were caused by the impurity gas atoms which were contaminating the poor samples. No differences between good and poor samples were detected, but a very unusual microstructure in all the samples was discovered. The implications of this microstructure for the interlayer coupling are discussed.

Chapter 5 is concerned with the effects of residual gas contamination on the indirect exchange coupling between the Co layers through the Cu spacers. By using a selective probing technique, small amounts of residual gas were inserted into the multilayer stack. It was found that the purity of the spacer layer is of paramount importance in achieving good antiferromagnetic coupling. Damage to the spacers layers was found to cause a 90° alignment of the magnetisations of adjacent layers, referred to as *biquadratic* (as opposed to the more common Heisenberg-like *bilinear* coupling). The temperature dependence of this coupling was measured, and a temperature independent scaling behaviour was observed, with implications for the common temperature dependences of various physical quantities in the structure.

Finally, this work and possible future extensions are summarised in Chapter 6.

2. Sample Preparation and Measurement Techniques

2.1 Sputter deposition of magnetic multilayers

2.1.1 Principles of sputtering

The erosion of the cathode by sputtering in a gas discharge tube was discovered over 150 years ago by W R Grove[11]. In a glow discharge there is a ready supply of gas ions which are, of course, positively charged. These are attracted towards the cathode by the Coulomb force and will strike it with a large kinetic energy when the applied voltage is high. This will result in the removal of material from the cathode, which leaves with superthermal energies. This is the sputtering process. When this material impinges upon a surface it will nucleate into islands and then grow into a film. By having a target of the appropriate material upon the cathode it is possible to deposit a film of that material.

The simplest way of striking up a glow discharge is to merely have a pair of electrodes in a low pressure gas and to apply a large voltage across them. For many years this diode means of sputtering was the most commonly implemented, due to it's simplicity. Here the target is the cathode with the substrate and surrounding chamber walls forming the anode. Applied tension of several kV and a sputtering gas pressure of around 100mTorr are required to achieve an even barely acceptable deposition rate.

In order to assist the formation of a strong glow discharge a triode arrangement is sometimes used. Here a filament thermionically provides electrons, which are attracted across the target and into the plasma by an anode, the third electrode.

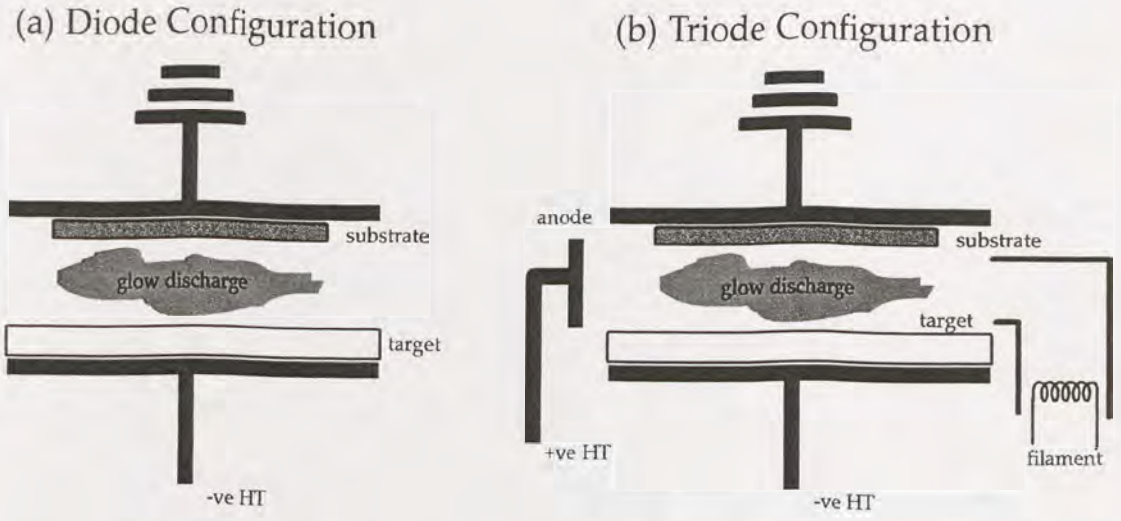

Figure 2.1 Diode (a) and Triode (b) sputtering arrangements. The triode has a thermionic filament, screened from deposits, to generate electrons which are pulled into the plasma by the anode. This helps to increase the rate and reduce the required voltage.

The gas used to provide the ions for sputtering is almost always Ar. It is essential to use a noble gas to prevent the target from reacting chemically with the energetic ions. Gases of low atomic mass are of little use as they impart little momentum to the atoms on the surface of the target, and Ar is the most readily available of the gases with an atomic mass comparable to that of the material to be sputtered. Interesting work has been carried out investigating the effects of using the different sputtering gases Kr & Xe. Different sputter yields for a target of a certain material will be achieved for the different gases, as the amount of energy transferred from the incoming noble gas atom to the atom in the target it strikes depends on their relative masses. An incoming atom of mass m_1 with energy E_1 colliding elastically at zero impact parameter with a stationary atom of mass m_2 will have a final energy E_1' given by

$$E_1' = E_1\left[\frac{m_2 - m_1}{m_2 + m_1}\right]^2.$$

The gas atom may be reflected back from the target with considerable energy. This may affect the characteristics of the growing film beneficially or

adversely; this will be discussed in greater detail below. Window suggested that the use of Xe was beneficial in the preparation of low stress W, Mo or Cr films, as it would be reflected with a much lower energy than say Ar, and proposed a novel system to allow economical use of this very expensive gas[12]. It has been found that the coercivity of Co/Pt multilayers can be increased by the use of heavier sputter gases[13], and that the GMR of multilayers[14] and spin-valves can be affected. However in large-scale processes Ar is almost always used.

These diode and triode methods produce poor quality films due to the low rates of deposition and high working pressures required. It is possible to use magnetic fields to concentrate the discharge plasma, in a manner based on the work of Penning over 50 years ago[15]. It has been refined over the years and been used in a series of different geometries, although by far the most common configuration now in use is the planar magnetron, introduced in the 1970s[16], although the basic means of plasma confinement was demonstrated 15 years previously[17]. The advantages of such a system are numerous; not only is film quality improved and the deposition rate increased, but it is a natural geometry for coating flat substrates in a uniform manner. In addition superthermal particles produce films which have a better adhesion to substrates, and do not require such high substrate temperatures as those produced by evaporation methods.

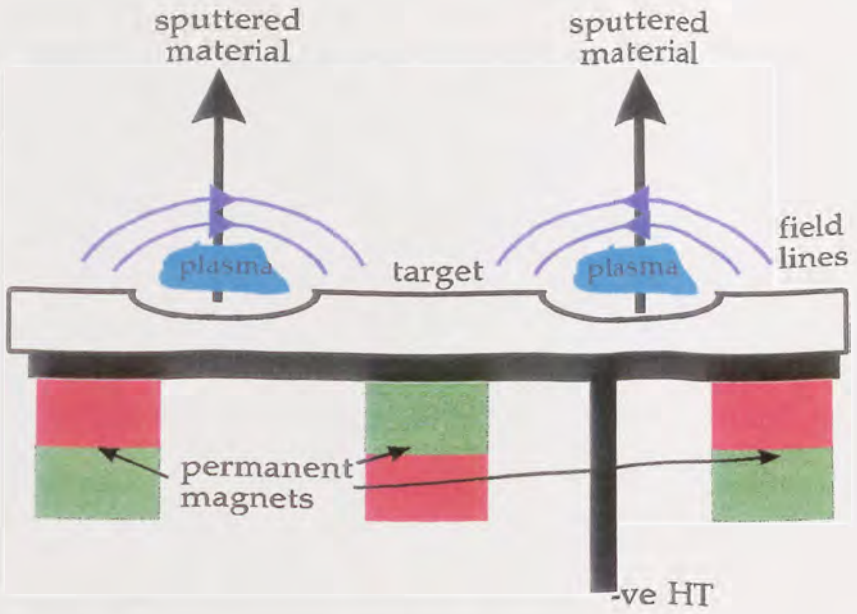

Figure 2.2 A magnetron cathode. The glow discharge plasma is confined closely above the target by the magnetic field. Most target bombardment occurs below this 'racetrack', resulting in non-uniform target erosion.

Most small planar magnetron sputter sources are circular in shape, and consist of the target, a disc of the material to be deposited, which is connected to a power supply as the cathode. It is backed by permanent magnets which provide a toroidal confinement field above it. The field strength is chosen such that electrons will have a Larmor radius of around 1-3 mm, confining them effectively above the target, whilst that of the much heavier ions will be at least an order of magnitude higher, allowing them considerable freedom. This helps to prevent unnecessary heating of the substrate by electron bombardment.

When the glow discharge is struck by the applied negative voltage, the ring shaped region defined by the field becomes dense in electrons, both those released from ionised gas atoms, and also secondary electrons released from the target by sputtering. They are affected by the Lorentz force from the electrode and permanaent magnets. Electrons travelling helically along the field lines towards the target centre are reflected by the negative potential, but also by the greater density of field lines in this region, in just the same way as charged particles are trapped in the Earth's Van Allen belts.

Once travelling radially outwards along the field lines they eventually reach the perimeter of the target. An anode is placed in this region to collect them and prevents them from reaching the substrate. The electrons also drift from one radial field line to the next resulting in a racetrack effect. The upshot of this complicated motion is to produce a long path length for these energetic electrons, resulting in a high plasma density closely over the racetrack. This ensures a ready supply of positive gas atoms, to be accelerated across the cathode dark space, typically a few mm, and sputter the target. This ensures a high deposition rate.

The magnetron is also favoured as a deposition source since it is easy to control. The magnetron drive is usually current regulated as the deposition rate is proportional to the sputter current. This is because mass flow of material from the target is proportional to the number of ions (charge carriers) striking it. Current generally has only a weak dependence on voltage of the form $I=kV^n$, where n is typically greater than 5, so the incoming energy of sputtering gas ions is not very much greater for larger currents.

All sputtering work performed at Leeds has been DC, although it is also possible to use an RF supply capacitively coupled to the cathode. This is essential when depositing non-conducting materials[18], in order to prevent a charge build up on the target surface which will stop the process. The higher mobility of the electrons means that there is a natural biasing voltage on the target, which provides the necessary potential for sputtering.

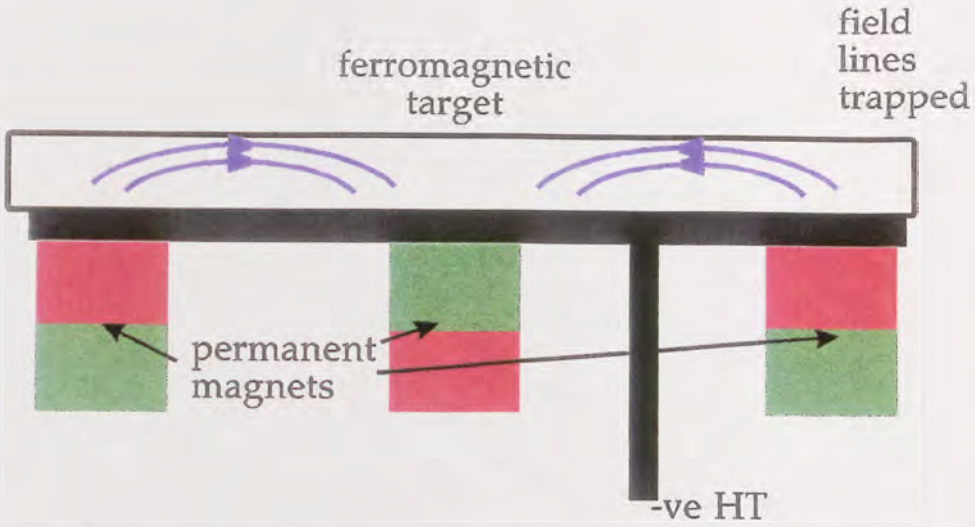

Figure 2.3 The effect of a thick ferromagnetic target. The highly permeable target traps the magnetic flux like a keeper. If the target is too thick, as in this case, then no flux will penetrate the target, and no plasma will be confined.

There is one major drawback to the use of magnetrons in our application however - if a ferromagnetic target is placed upon the cathode then a large amount of the flux from the magnets will be captured by the target and very little will penetrate through and capture electrons to form a plasma. This places a strict limit on the amount of magnetic material that can be used as a target, as a function of its permeability. Above a critical thickness the gun will fail to strike a plasma, and just below this thickness the plasma will be so weak as to be almost useless. This has presented a particular problem in the past, and the original IonTech magnetrons in our system are unable to sputter from Fe targets thicker than ~0.1mm. This is problematical for two reasons: the target will not last for more than one or two hours of continuous sputtering, and the target is now flexible enough that the localised heating in the racetrack area can cause the target to lift away from it's cooling block as it expands. Once it is no longer in contact it can heat extremely rapidly, and we have experienced melting of Fe in the racetrack area with the application of only moderate sputter currents. The melting point of Fe is 1540°C. The use of new, more powerful permanent magnet materials in modern magnetrons, in addition to improved design

now allows the use of thicker targets. A large production scale contemporary magnetron gun is capable of sputtering targets in excess of ½" thick.

2.1.2 Control of film properties

Historically sputtering has been associated with poor film quality in comparison with evaporation techniques. However advances in vacuum technology have allowed for the preparation of high quality metallic multilayers in the early 1980s[19], and for very high precision epitaxial superlattice growth more recently[20]. Sputtering is now the deposition method of choice in the emerging GMR sensor industry, and enjoys advantages of speed and cost-effectiveness over more exacting preparation techniques such as MBE. In addition the highest GMR values yet reported are in sputtered multilayers[21] and spin-valves[22]. This in part due to the control over incoming particle energy which is possible, as the technique does not rely on the fixed melting point of the metal being deposited.

The choice of deposition rate is important in determining overall film quality. High sputtering powers are associated with larger grain size, due to the greater available surface mobility of adatoms allowing them to settle into lattice sites, but also the lower impurity content in the faster growing film. No vacuum system ever achieves total cleanliness, and the contaminants remaining in the system at base pressure will be found in the film, as well as a small amount of the sputtering gas. The rate of impurities arriving at the substrate, or indeed any other surface in the system is proportional to their partial pressures, in a manner calculated in any text on surface science[23]. It takes less than a minute to achieve monolayer coverage of any contaminant when its partial pressure is 10^{-7} Torr, assuming a sticking coefficient of unity. If we deposit metal at say one monolayer per second, a typical sputtering rate, we can expect the film to contain a few percent of 'sticky' impurities such as oxygen & water, and these can have a drastic effect on sensitive film properties such as the GMR[24]. Indeed it is possible to form entirely new phases of materials by the inclusion of such innocent seeming accidental

dopants as nitrogen; e.g. β-Ta, a tetragonal phase not seen in bulk[25]. The importance of a clean vacuum is readily appreciated. Indeed we have found this aspect to be extremely important, and it will be discussed further below, and in Chapter 4 and 5.

A bias voltage can be applied to the substrate in order to modify the type of bombardment to which the growing film is subjected. A **negative** voltage will prevent electron **bombardment** , but this is not a problem in magnetron sputtering. A negative voltage will promote positive ion bombardment of the growing film. A bias voltage of only -30V is sufficient to entirely destroy any GMR at the first Cu peak in Co/Cu multilayers[26].

Control of substrate temperature is less important than in evaporation techniques such as MBE since the surface mobility of adatoms can be controlled: firstly the energy distribution of the incoming atoms themselves may be varied, and additional energy can be injected through the impact of high energy reflected neutrals. High substrate temperatures are associated with a lower GMR[27], as the layers tend to become more interdiffused. This is in line with the results of annealing experiments carried out on GMR multilayers[28]. Substrate temperatures as low as 100K can be used in order to produce a smoother film.

Epitaxial growth is also possible by sputtering[29], if the conditions are carefully chosen. High substrate temperatures for the deposition of a single crystal seed layer and a clean vacuum system are essential. The correct choice of a seed buffer layer will encourage epitaxial growth with the desired crystallographic orientation[30].

2.1.3 Structure zone models & reflected neutrals

In 1969 Movchan and Demchishin published details of their classification scheme relating the microstructure of vacuum deposited films to a particular deposition parameter - the substrate temperature[31]. They grew films of various metals and metallic oxides by high rate electron beam evaporation onto copper and niobium substrates upon which they had

established steep temperature gradients, and found that the form of the growth was different in three different zones on the substrate according to the temperature at that point. In particular they found that the transitions from one structure zone to the next occurred at common values of T/T_m, where T is the surface temperature of the growing film, and T_m is the melting point of the metal in question.

For values of $T<0.3T_m$ (Zone 1) they found that the film was in the form of tapered grains, with poorly defined boundaries, and domed tops. The grain size increased with temperature. For $0.3T_m<T<0.5T_m$ (Zone 2) there is a changeover to columnar grains with well defined boundaries, and the top surface of the film is smooth, and matt in appearance. The grains increased in width in accordance with the activation energies of surface diffusion. For $T>0.5T_m$ (Zone 3) the grains are **equiaxed** and have a bright surface. The structure and properties correspond to a fully annealed metal, the grain size increasing with the activation energies of bulk diffusion. Other properties such as the hardness and lateral tensile strength were found to be different in the different zones.

Thornton extended the model to sputtering by adding a second axis to the zone diagram to account for the sputtering gas pressure used, on the basis of the results of preparing metal films by magnetron sputtering[32,33]. He found that films grown in Zone 1 at low pressure were not as expected, but were better described by a transition zone between 1 and 2, which he called zone T. These films consisted of densely packed fibrous grains, without voided boundaries. The width of this zone decreased as the pressure of the working gas rose. The pressure had little effect on films grown at high T/T_m.

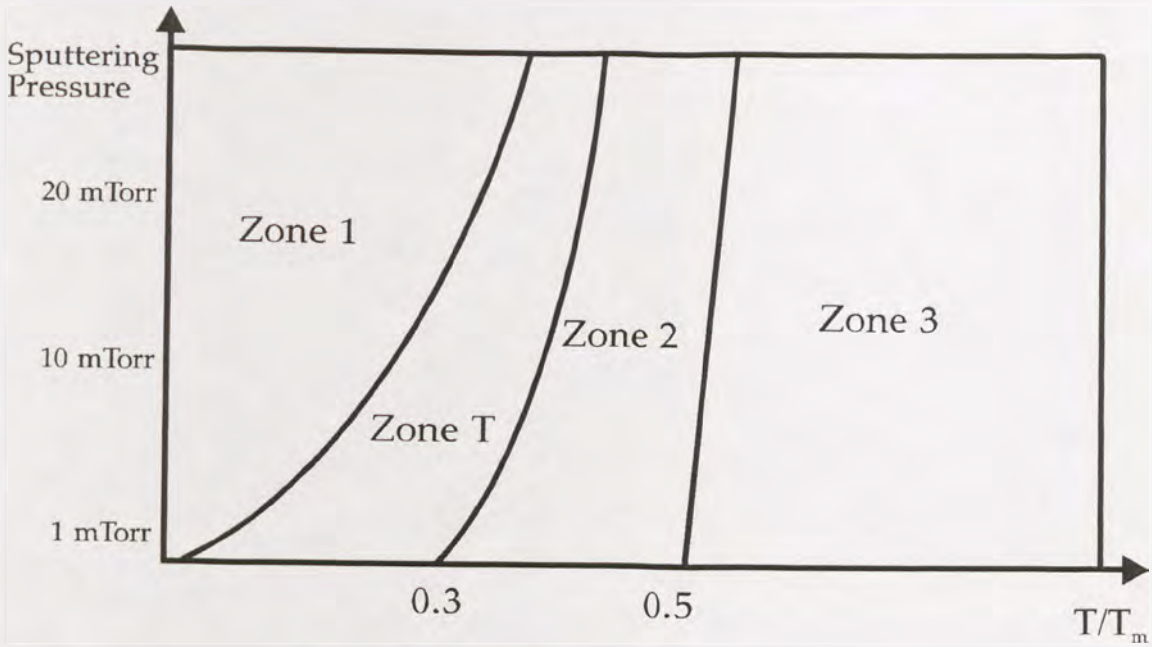

Figure 2.4 Zone diagram for films deposited by magnetron sputtering. T is the substrate temperature, and T_m is the melting temperature of the deposited metal.

These results can be readily interpreted in terms of the available energy of the adatoms. In Zone 1 there is little opportunity for atoms to diffuse, and the film properties are determined by self-shadowing effects, allowing larger grains to grow at the expense of smaller ones. If there is sufficient energy available for surface diffusion to occur there are fewer voids, and smoother surfaces. This has been successfully modelled by molecular dynamics simulations[34]. A simple model explaining the relative contribution of these two terms is given by Bales and Zangwill[35], in the limit of high working gas pressure (also applicable to IBS and MBE). It is correct to consider these two contributions to the mobility separately as the substrate temperature effects occur in thermal equilibrium, whilst the bombardment induced mobility does not. This is why zone T is required, rather than the additional mobility induced by heavy bombardment simply extending zone 2 at low pressures.

In zone 3 there is sufficient energy available to allow bulk diffusion and effectively anneal the sample as it is grown. As mentioned above, this bulk

diffusion is known to destroy the fine layering of GMR structures, and this zone will not be considered further.

These ideas were originally developed to discuss films much thicker than those of a few tens of Å involved in the production of GMR structures. The microstructure of the growing film develops rapidly from the original nucleation sites on the substrate, and this was recognised by Messier *et al.* who added a third axis within zone 1 (and its subset zone T) for the thickness of the film[36].

The product of the target-substrate distance and the sputtering pressure will determine the degree of thermalisation of the sputtered material and the reflected argon neutrals. The metal atoms leave the target with a so-called Sigmund-Thomson energy distribution[37]. A typical target voltage is ~400V, so that metal atoms sputtered from the target have energies ~10eV, whilst reflected neutrals have energies ~100eV[38]. If these particles collide with gas atoms they will give up energy in the collision and will eventually reach the thermal energy associated with the temperature of the gas. The number of collisions experienced by sputtered atoms and reflected neutrals is proportional to the product of the sputtering pressure and target-substrate distance. Lower pressures and shorter distances will result in less thermalisation leading to higher energies for incoming particles[39].

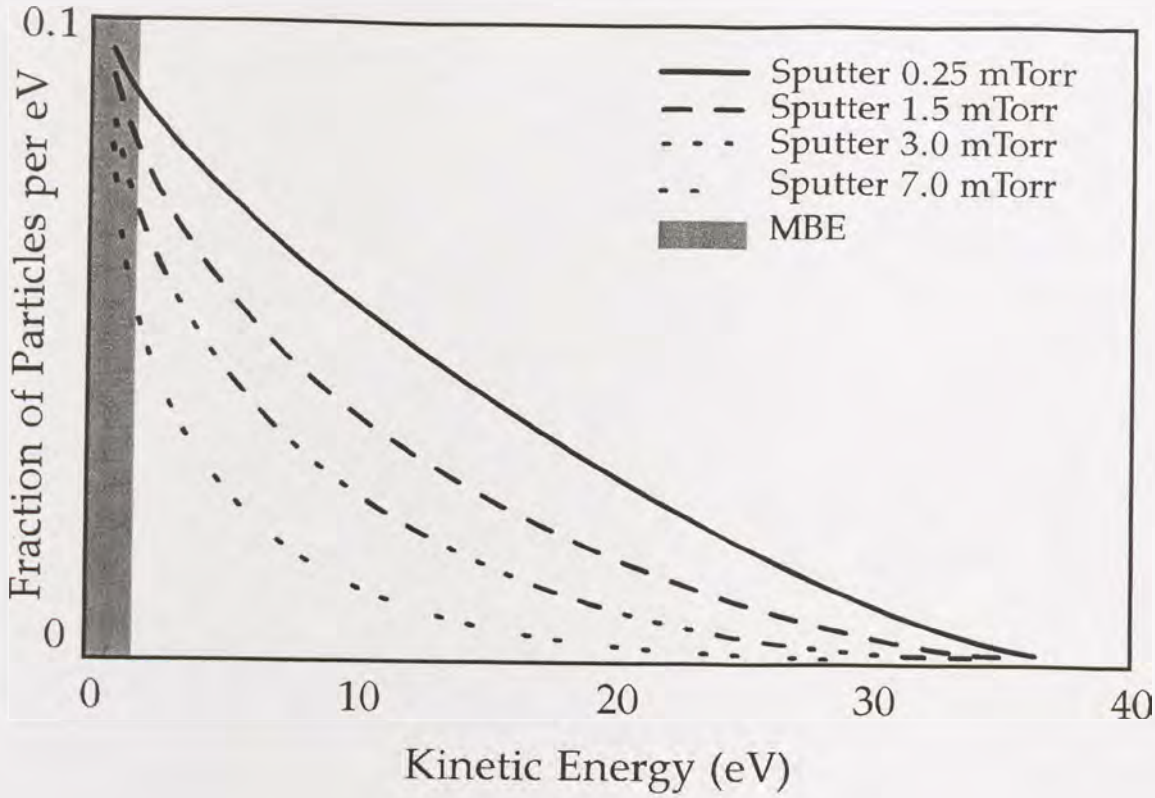

Figure 2.5 Kinetic energy distribution of sputtered atoms arriving at the substrate. At high pressures the energies are increasingly thermalised towards the MBE-like regime. At low pressures there are considerably amounts of medium-energy (~10eV) particles. Based on a calculation by Kools (ref 45).

Reflected neutrals play an important role in determining the final film properties, as they bring more energy to the growing film than the incoming sputtered atoms. There have been many studies, both computational and experimental, of the effects of energetic particle bombardment on thin film growth. In the 1960's Frerich showed that sputtered films of Nb were superconducting when exposed to ion bombardment during growth[40]. Maissel and Schaible found that the application of a negative bias to a growing Ta film would decrease the resistivity towards a bulk value, by virtue of encouraging positive ion bombardment[41]. This encourages surface mobility and also removes active gas from the film. This was confirmed by Winters and Kay, who measured directly the amount of nitrogen in films grown reactively with various applied biases[42]. The pressure of sputtering

gas has been shown to affect the structure of the growing film in both multilayers[43,44] and spin-valves[45]. Fullerton et al. showed that for increased sputtering pressure Fe/Cr superlattices would become considerably rougher, with interesting consequences for the GMR[46].

It is also possible to vary the sputter gas pressure upwards from the lower limit in order to control the deposition rate. Up to a certain point the sputtering rate will rise with the pressure as there will be more ions present. However the higher gas density between the target and substrate means that the mean free path of sputtered atoms is reduced. This not only decreases the energies of the incoming sputtered atoms by thermalisation, but also reduces the target voltage required to produce the magnetron current. This means that at high pressures the rate is reduced, as the sputtering energy of each incoming Ar atom is reduced. This also affects the energy of sputtered atoms and reflected neutrals at the growing film[47]. This interaction with the gas is partly responsible for the fact that sputtering is more effective at step coverage over substrate topography than UHV evaporation methods.

2.1.4 Magnetic multilayer deposition at Leeds

2.1.4.1 The original system

A sputter deposition system has been developed at Leeds for the preparation of magnetic GMR multilayers. It is based around an older system used for amorphous alloy research. The original system was installed around a decade ago, and contained four substrate stations and three targets. Only one of these sputter guns was capable of depositing magnetic materials - a Simard Tri-Mag gun, which operates on the triode sputtering principle with permanent magnets surrounding the target to concentrate the Ar plasma. This gun has since been removed from the system. The other two guns are standard planar magnetrons which sputter from 2" targets. These guns are arranged in a circle of 7" radius around the centre of the baseplate, facing directly upwards. This configuration prevents any wedging effects, ensures columnar growth is vertical[48], and prevents magnetic anisotropy in

deposited films due to stray fields from the magnetrons or canted growth modes.

The vacuum chamber itself is very large, 24" diameter by 24" high, and sealed entirely on viton O-rings. It is rough pumped into the milliTorr range by a rotary mechanical pump, at which point this pump is valved off, and an 8" gate valve opened onto a cryopump of equivalent diameter. After pumping for around twelve hours the base pressure of $\sim 2\times10^{-7}$ Torr is reached. Residual gas analysis (RGA) is performed with a **quadrupole** mass spectrometer, and at this point the mixture of residual gases is typically as follows:

H_2 1.0×10^{-9} Torr	He 0.5×10^{-9} Torr	H_2O 5.0×10^{-8} Torr
N_2 2.0×10^{-8} Torr	O_2 2.0×10^{-9} Torr	CO_2 2.0×10^{-8} Torr

It can be seen that the main residual gas is water vapour, which is well known for adhering to the walls of vacuum systems.

A needle valve is then opened to admit Ar gas, the pressure of which is measured by an ionisation gauge with a precision of 0.1×10-3 mbar. The cryopump can be throttled back to allow the sputtering pressure to be reached with a smaller mass flow of gas. The Tri-Mag gun had it s own gas supply injected directly over the target, as the triode requires a large local pressure directly over the cathode in order to function properly. In particular it was found that a very high pressure, ~100 mTorr, was required in order to strike the initial plasma. The magnetron guns start and run in the usual sputtering pressures of a few mTorr, except for when brand new targets of reactive metals have been installed. This requires the guns to be run at higher pressures, ~20 mTorr, for a few minutes, until the surface oxide layer has been sputtered away. These targets can then be sputtered at the usual gas pressures.

2.1.4.2 Substrate positioning & control

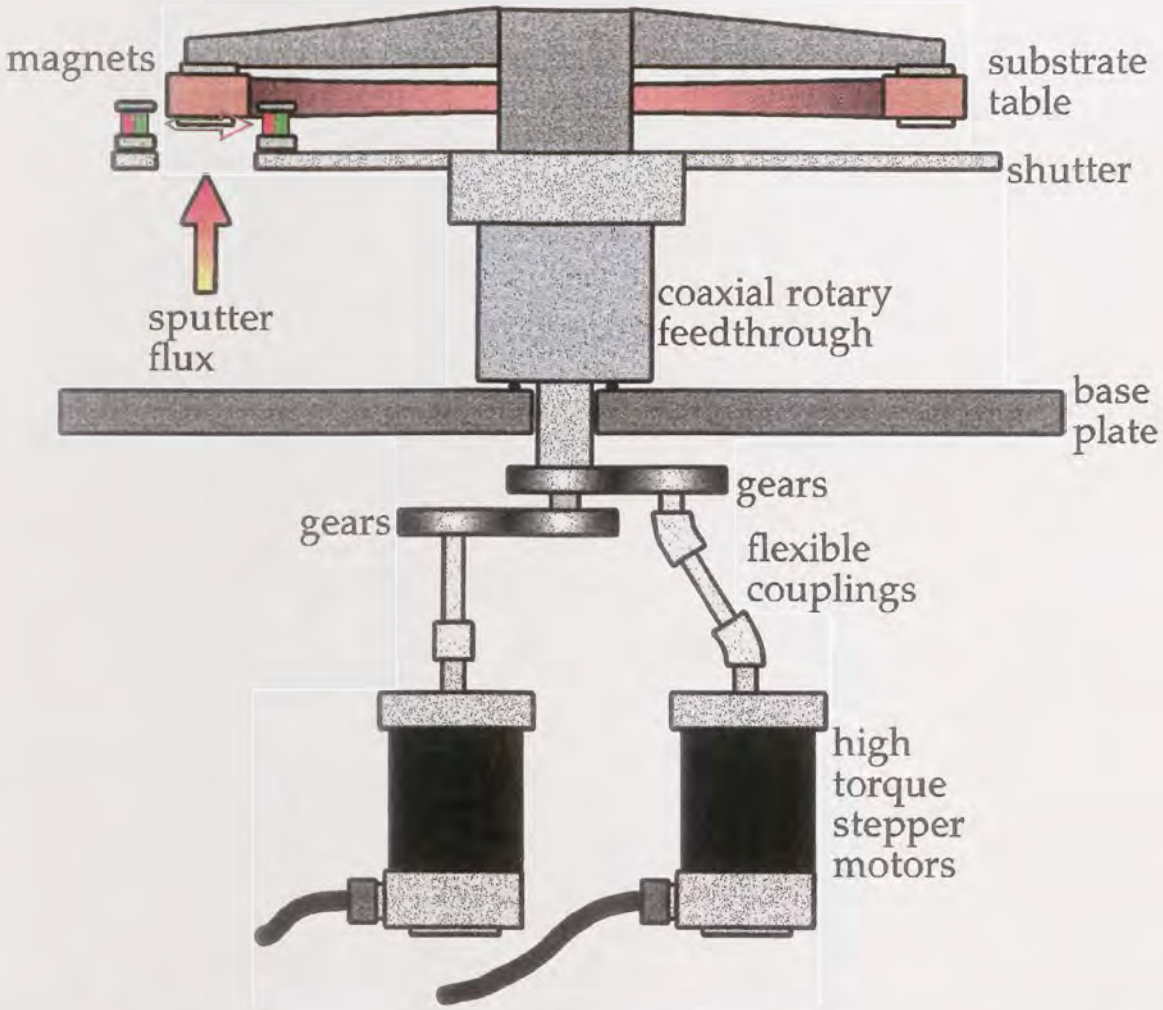

Figure 2.6 The substrate positioning and shuttering system. The wheel-shaped substrate table and shutter can be independently rotated by the stepper motors. The various sputter sources are arranged in a circle in the base plate below the rim of the wheel. Any sample may be moved over any source, and then exposed by the shutter, allowing any arbitrary structure to be grown.

The first task undertaken was to allow a larger number of samples to be grown in one pumpdown - this would mean that a single parameter could be varied over a larger number of comparable samples, as well as increasing the throughput of the machine. A replacement substrate table was designed, consisting essentially of a large wheel of pure copper to which the substrates could be attached. This wheel could be rotated around in order to bring any

one of sixteen substrate positions over any of the deposition sources. Copper was chosen due to its high thermal conductivity, in order to ensure that the temperature of the substrates could be well controlled. The copper wheel was supported by a stainless steel superstructure, as shown in Fig 2.6. This design benefits from being very light, but able to support the large mass of the copper wheel. The wheel contains holes into which can be fitted sixteen heaters and sixteen thermocouples. This allows the temperature at any one of the substrate positions to be measured and controlled. The wheel also contains a cooling channel through which water can be flowed - this is sealed with a long weld rather than O-rings in order to allow for high substrate table temperatures.

Directly below the substrate table a new shutter was installed. This was initially a single large disc cut from thin stainless steel sheet. One 50mm diameter hole was cut with it's centre 7" from the axis of rotation of the shutter. This has since been replaced with a thicker aluminium shutter disc which has the mechanical strength to support two arrays of SmCo rare-earth magnets which provide a uniform forming field of ~200 Oe for sample growth. The magnets are above the hole in the shutter plate so that which ever sample is currently being deposited is in the field. The calculated angular dispersion in the magnetic field over a 5cm square centred over the hole in the plate is less than 1°.

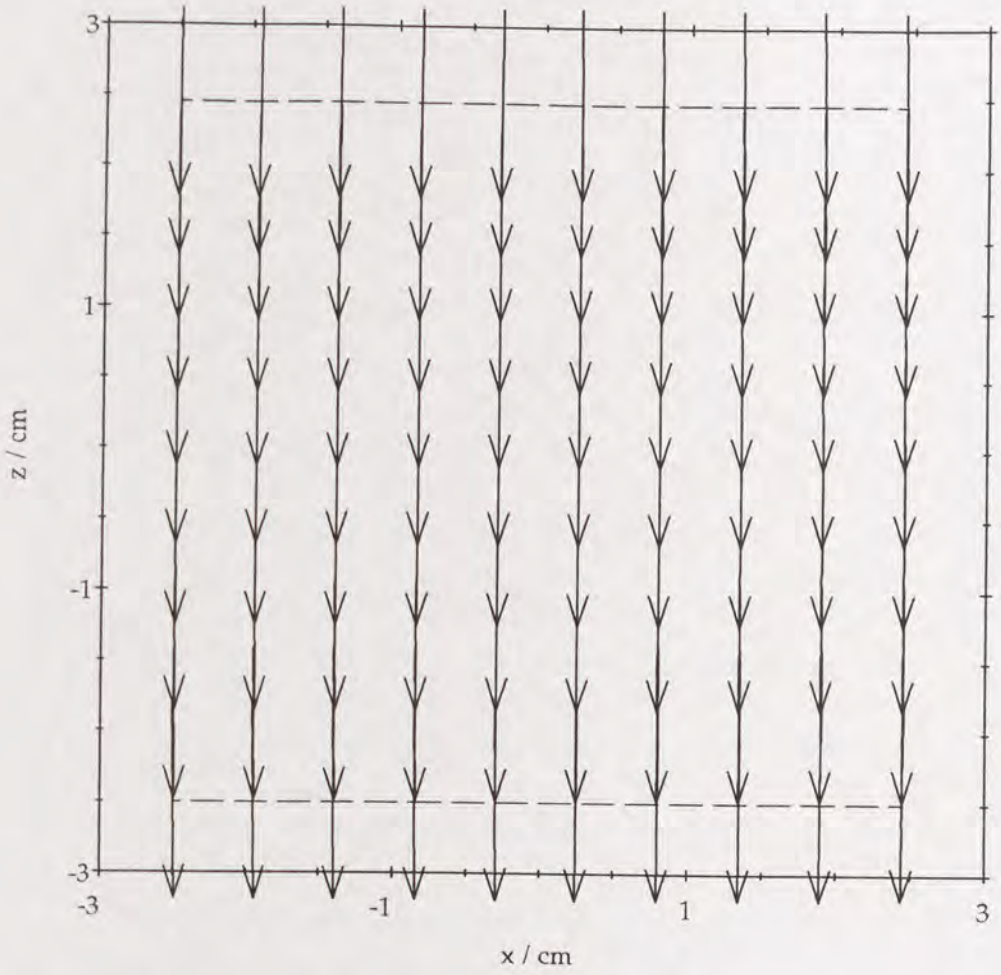

Figure 2.7 The calculated forming-field distribution in the region around the substrate. In the co-ordinate system used in the calculation the substrate surface lies in the x-z plane. The rms angular dispersion in the field is 0.32°.

Both the substrate table and shutter are attached to an original rotary motion feedthrough in the centre of the baseplate. The original shutter and 4 substrate stations were rotated by means of DC motors with a positioning accuracy of no better than around 10°. These were replaced with high torque hybrid stepper motors which operate under computer control. These motors have 400 steps per rotation, meaning that we have a positioning capability better than 1°, which is ~3 mm at a 7″ radius. The original feedthrough and gearing mechanism have so far been retained, although they were not designed to allow something with as high a moment of inertia as our new

substrate table to be rotated rapidly. There is noticeable mechanical backlash in the shutter due to the transmission drive shaft being set at an angle. It has been possible to compensate partly for this in the software, but it should still be possible to improve the mechanical accuracy of the system, allowing faster rotation of the substrate table and shutter between sources. Two methods suggest themselves: indexing the shutter and substrate table inside the chamber so that the computer is aware of the angular positions, or to replace the current legacy feedthrough. The substrate table could be suspended from the top of the chamber, so that both it and the shutter would be driven directly by single rigid shafts.

Custom software was written in order to make the deposition sequence programmable. The user is able to request any arbitrary series of layers to be deposited on any of the substrates, which the system will automatically perform. Individual layer thicknesses are controlled by requesting the system to pause for a specified period of time. It is therefore important that the sources be well calibrated.

There is a single quartz oscillator thin film monitor which can be fixed at any one point in the chamber. This can be used for real time monitoring of one magnetron gun. This method is rarely used, as it is difficult to get the monitor into a position where it will not obstruct the flux to the substrate. More commonly one of two X-ray techniques are used, as described in section 2 of this chapter. Both involve deposition for a fixed time, and the thickness being measured *ex situ*. The deposition rate is then known for the growth of further samples. Both X-ray and quartz oscillator rate measurements are found to be consistent to within about 5%.

The deposition of very thin layers (less than ~20Å) presents further problems when metal is being deposited at a rate of a few Å every second - timing resolution of ~0.1s required. This is the roughly the resolution of the time-of-day clock in a standard PC, which generates a hardware interrupt eighteen times a second. It is hence certainly possible to time to this level with the computer without requiring **sophisticated** assembly language

routines, but there is always a small overhead involved in computing what the next motion should be, and also in actually moving on and off the deposition source. The legacy mechanical transmission system will not allow the motors to be operated at more than around 50 steps per second, so it will take a few tenths of a second to move on and off the source position. The overall timing overhead is a little over a second, and so it must be remembered when programming the system for a particular deposition sequence involving very thin layers that this amount will be added to every deposition time requested. Having said this, the overhead is a constant for a particular configuration of the system hardware and software, and it is possible to control the thicknesses of layers accurately to less than ±0.5Å.

2.1.4.3 Further improvements

Initially the new substrate table was installed so that the target substrate distance was extremely long, ~25cm. Chimneys were installed on the three deposition sources, in order to prevent material sputtered from other guns from contaminating a growing film. In addition these chimneys help to ensure chemical purity of the layers, as the inside of the chimney walls are constantly coated with freshly deposited metal, which will getter many residual gases. This results in a locally very pure volume between the target and substrate. However once we were aware of the effects of large pressure-distance products on the film microstructure, and the associated magnetic and GMR properties, the table was lowered and the magnetrons raised to reduce the distance to ~6cm. In this way we dramatically reduced the level of thermalisation of both the sputtered metal atoms and reflected argon neutrals.

A new magnetron was added, which employed powerful NdFeB magnets to sputter thicker ferromagnetic targets, of up to 1.5mm thickness in the case of Co. The Tri-mag gun was removed to make room for two more IonTech 2" planar magnetrons in order to allow a wider variety of different materials to be deposited in a single structure - essential for the growth of

spin-valves.

2.1.4.4 The importance of residual gases

A final important addition was made - a Meissner trap was constructed from a coil of ¼" copper pipe, which was installed in the large empty space at the top of the chamber. Liquid nitrogen is forced through the tube from a large storage dewar by pressurising the dewar with a bottle of compressed nitrogen. A continuous flow of liquid nitrogen is maintained throughout deposition, as the heat leaks into the coil from the top plate are large, and it will warm and begin to release trapped gases only a few minutes after the nitrogen supply is removed.

The total surface area of the coil is many times that of the 8" diameter hole leading to the cryopump, leading to very high pumping speed for easily condensable gases, in particular for water vapour. The base pressure is improved by over an order of magnitude, principally by the removal of H_2O. The approximate partial pressures of various gases are:

H_2 1.0×10^{-9} Torr	He 0.5×10^{-9} Torr	H_2O 1.5×10^{-9} Torr
N_2 3.0×10^{-9} Torr	O_2 0.1×10^{-9} Torr	CO_2 0.5×10^{-9} Torr

The partial pressure of every gas has fallen, and significantly in certain cases. It can be seen that the level of H_2O has dropped to a little below that of N_2, and there has also been a large reduction in CO_2 levels.

This was found to dramatically improve the GMR properties of the samples. A full discussion of these effects will be found in Chapter 3, but this figure will illustrate the dramatic improvement this one change has made.

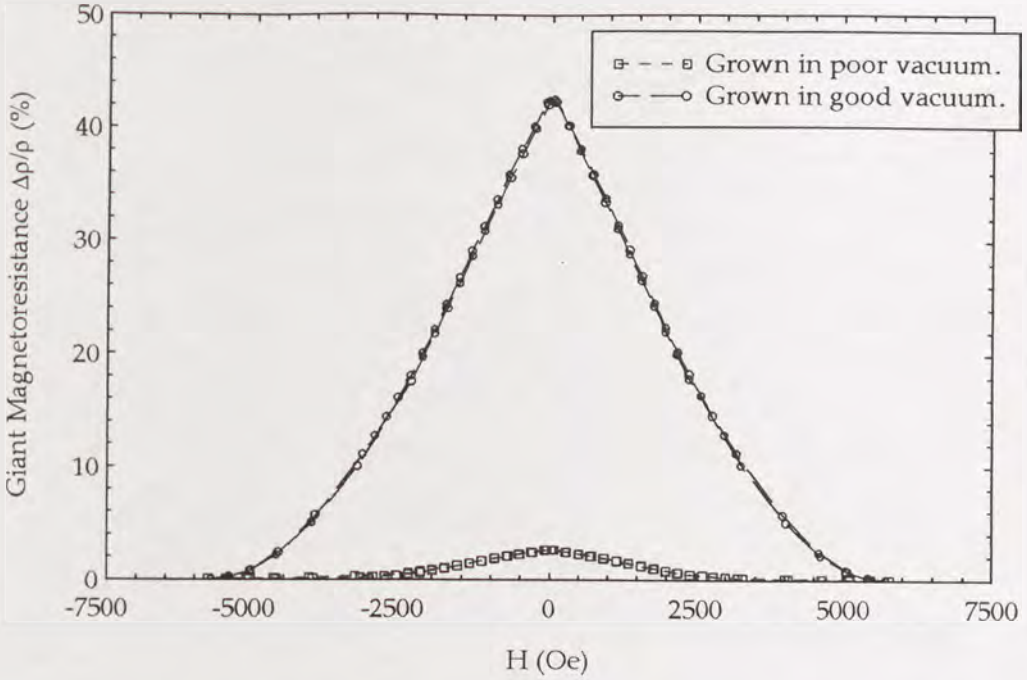

Figure 2.8 The effect of using the Meissner trap to improve the base pressure on the giant magnetoresistance of a Co/Cu multilayer.

New power supplies have also been added, which are capable of being controlled by the PC. They provide better regulation of the magnetron current to lower levels, and have arc-suppression circuitry to give cleaner plasma ignition. The digital control allows more complex deposition sequences to be easily programmed.

2.1.4.5 The current system

In summary, the sputter deposition system which was developed has the following features:

- base pressure of better than 2×10^{-8} Torr.
- 5 different targets, 1 may be ferromagnetic.
- relative layer thicknesses precisely controlled to ±0.5Å.
- capable of depositing 15 different samples per vacuum cycle.
- samples may be of arbitrary complexity.

2.2 X-RAY CHARACTERISATION

2.2.1 Theory and methodology

X-ray diffractometry is a non-destructive structural characterisation technique which is well suited to the analysis of thin-film and multilayers due to their shape and dimensions. Since its discovery at this university[49], X-ray diffraction is a subject which has been studied both widely and deeply, and a full discussion of the possible applications to thin films would require a long textbook. In this section those simple techniques which have been used at Leeds to characterise the sputtered samples will be discussed.

Of fundamental importance is the condition for Bragg reflection from a structure of period d:

$$n\lambda = 2d\sin\theta,$$

where θ is the angle of reflection, λ is the X-ray wavelength used, and n is the order of the reflection. In traditional crystallography d is defined as the distance between atomic planes, and for a particular set h,k,l of Miller indices may be defined as

$$d_{hkl} = \frac{a}{\sqrt{h^2 + k^2 + l^2}},$$

where a is the lattice constant. **This expression applies only to cubic crystals.**

The X-ray diffractometer used at Leeds is arranged in the Bragg-Brentano geometry and is used to perform θ-2θ scans. In this geometry the scattering vector is perpendicular to the film surface, and so only information about the structure in this direction is obtained. The X-ray tube contains a copper target, and Cu-Kα radiation is used, which has a wavelength of 1.54Å. There is a Ni filter before the detector to filter out Cu-Kβ. The sample and detector arm are rotated at constant angular velocities by motors, with $\omega_{sample} = \frac{1}{2}\omega_{detector}$. The detection electronics converts the count-rate to an output voltage, which is logged on a PC. The PC does not measure the angle 2θ, but infers it from the time elapsed since the start of the experiment, which was at a known angle.

2.2.2 *Low angle scans and calibration techniques*

2.2.2.1 Bragg reflections

Low angle scans are those where 2θ is varied between roughly 1° and 10°. The length scales which will produce Bragg reflections at such small angles are roughly 5-50Å - on the scale of individual layer thicknesses. The bilayer period of a multilayer sample generally falls within this range. The sample is aligned at 2θ=1°, close to the critical angle where the X-ray beam is strongly reflected from the film's upper surface, and the count rate is very high.

Superlattice type samples which have a periodic structure will give Bragg reflections according to the Bragg law given above, where d is now the superlattice period. This will be affected by the refractive index of the film at very low angles, $2\theta < \sim 3°$. The refractive index of the film is not unity, and this will have an effect on the optical path length. In addition the uncertainty associated with high angle Bragg peaks is smaller, as

$$\frac{\Delta d}{d} \sim \cot\theta \frac{\Delta\theta}{\theta}.$$

Measurement of the the bilayer Bragg peaks allows a highly accurate means of calibrating a pair of deposition sources - a series of multilayers of the general form {A(a)/B(b)}×N is grown, where A and B are two different metals, deposited for a or b seconds. The time a is held constant, whilst b is varied for each different sample. A plot of the measured bilayer period against b will yield a straight line, where the slope gives the deposition rate of B, and the y-intercept gives the thickness of A. This is particularly convenient in those experiments where the thickness dependence of one or the other layer in a superlattice is being investigated, as it allows direct layer thickness determinations on the particular samples of interest.

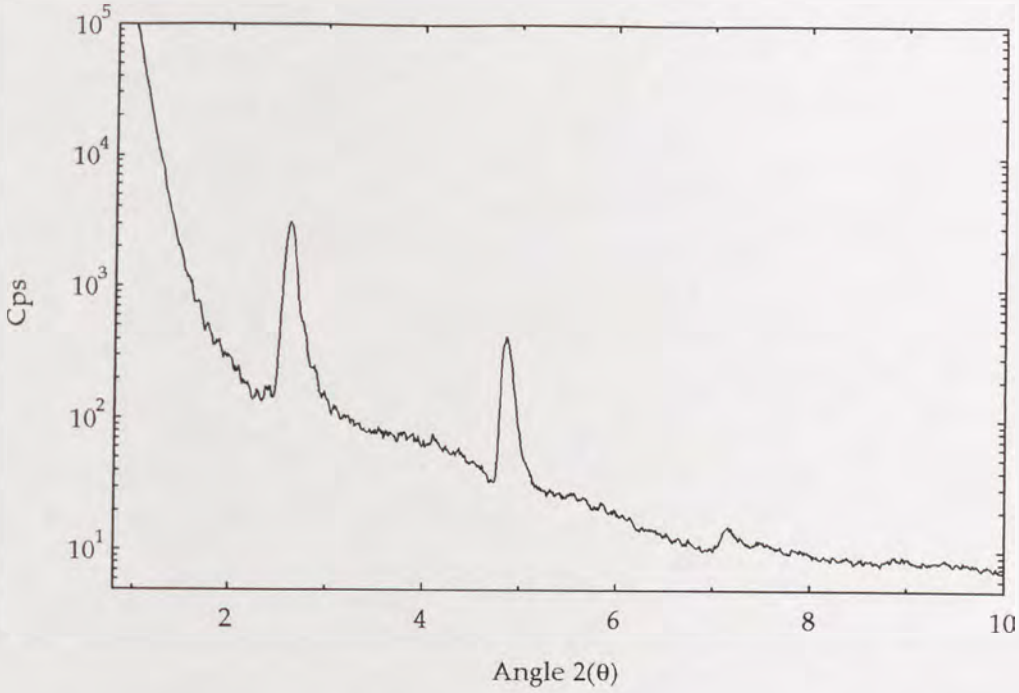

Figure 2.9 Low angle Bragg peaks due to the periodicity of a Co/Cu sputtered multilayer. The first and second peaks are distinct, the third is just visible.

2.2.2.2 Kiessig fringes

Total reflection of X-rays from thin films is observed for glancing angles of the incident beam less than the critical angle. Just above the critical angle X-rays are still specularly reflected with a large intensity. As first observed by Kiessig[50], specular reflections from buried interfaces may interfere with this reflected beam. In the simplest case of a single thick film of several hundred Å the substrate/film interface is likely to be very strongly reflecting. Interference fringes are observed along the specular ridge as a function of reflection angle above the critical angle.

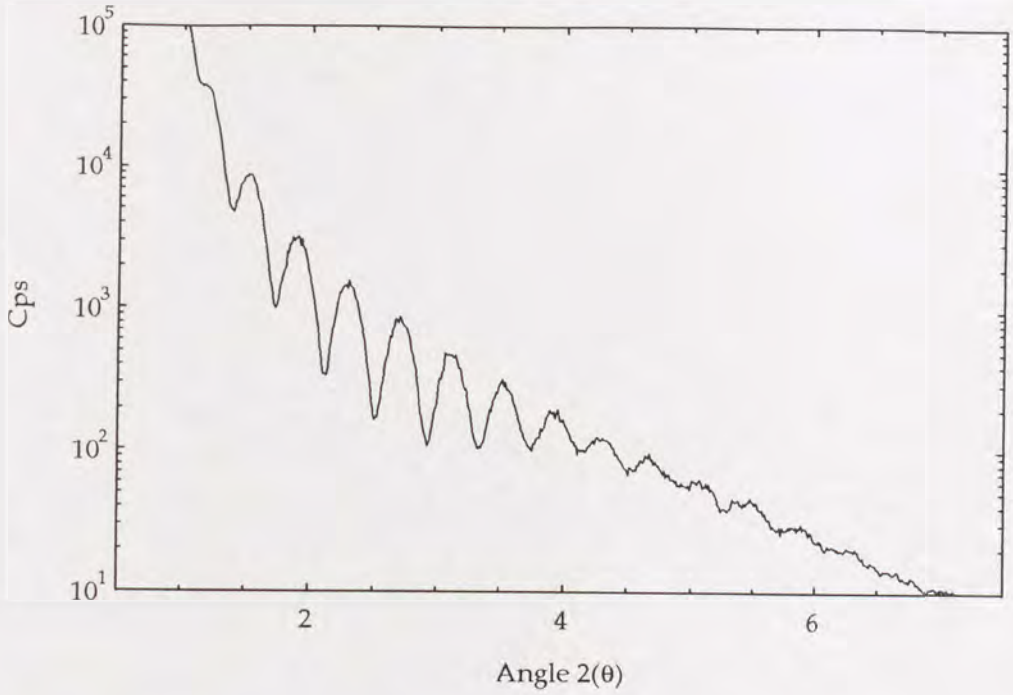

Figure 2.10 Kiessig thin film interference fringes. The sample was a thin film of Co.

This phenomenon allows a method of measuring the thickness t of the film, as the position of the mth extremum is given by

$$\theta_m^2 = 2\delta + (m+k)^2\left(\frac{\lambda^2}{4t^2}\right),$$

where δ=Re(1-n), n is the refractive index of the film, k is 0 or ½, for minima or maxima respectively, and λ is the X-ray wavelength. The quantity δ is proportional to the number density N_e of electrons, as given by

$$\delta = \frac{r_e N_e \lambda^2}{2\pi},$$

where r_e is the classical electron radius, 2.818×10^{-15}m. The definition of k is valid when for $\delta_{substrate} < \delta_{film}$, true generally for metal films on semiconductor substrates. If $\delta_{substrate} > \delta_{film}$, k is 0 or ½ for maxima and minima respectively[51].

It is possible to perform an analysis which eliminates the dependence of δ and k by measuring the angles of successive maxima or minima and calculating the squares of the differences. When these values are plotted

against successive integers a straight line of slope $\lambda^2/4t^2$ will be obtained. We then need only the wavelength to determine the thickness, as any series of consecutive integers will allow us to measure the slope. This was performed by a least squares fit to the data, and the uncertainty in the slope allows the uncertainty in the film thickness to be measured. More sophisticated measurements and analyses can be performed to allow the value of δ to also be measured[52].

The technique makes no reference to film crystallinity, and can be applied to any film that has sufficiently smooth interfaces, be it epitaxial or amorphous. Surface roughnesses will smear out the fringes more rapidly as the detector angle increases. It is possible to introduce a Debye-Waller factor for the surface roughness

$$D = \exp\left(\frac{-16\pi^2 \sin^2\theta\langle z^2\rangle}{\lambda^2}\right),$$

where $\langle z^2\rangle$ is the mean square deviation of the real surface from an ideal plane[53]. Further refinement in terms of the Rayleigh grating theory allows accurate predictions of the fringe contrast and intensity falloff with angle[54].

It can be seen that a longer fringe period is associated with a thinner film. Samples consisting of more than one film will exhibit reflections at each interface and this can lead to a complex superposition of fringes. For systems such as Co/Cu or NiFe/Cu multilayers, where the different metals have similar values for δ this effect is not significant. However oxide forming on the surface of the sample can form a different layer of very different free electron density, and these thin layers can modulate the fringes, as shown below.

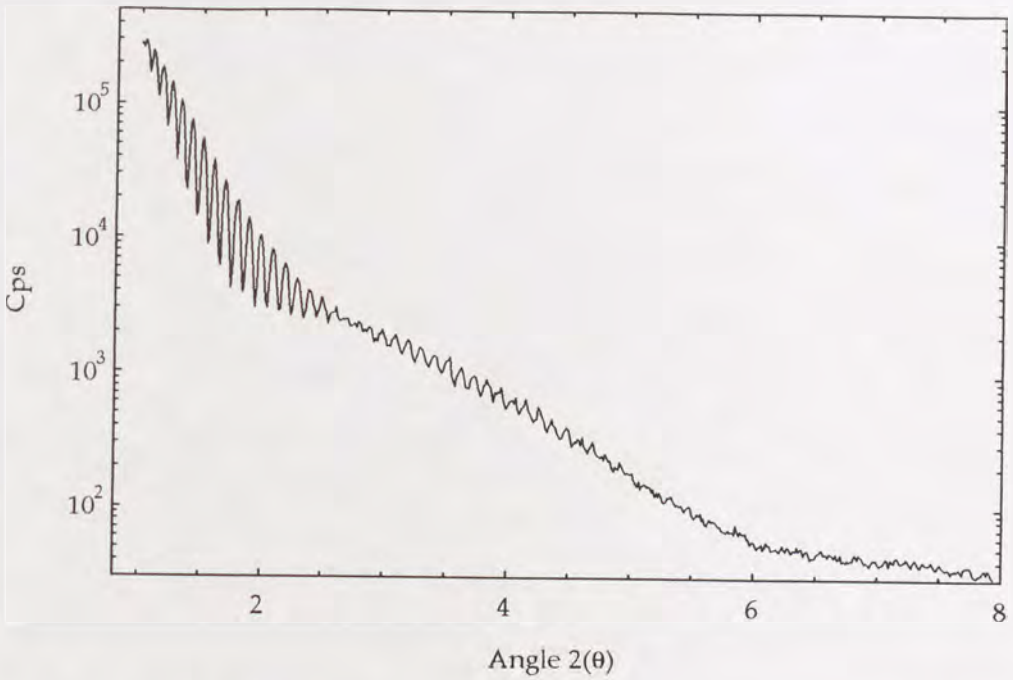

Figure 2.11 Modulated Kiessig fringes - the low angle scan is of a single film of copper with a thin oxide layer on it s surface.

It is immediately apparent that this technique allows the calibration of individual deposition sources, if single films are deposited for a fixed length of time. Usable series of fringes are produced from films between 100 and 750Å thick. For thicker films the close spacing of the fringes makes measurement of the angular differences inaccurate.

2.2.3 High angle scans and film texture

High angle scans are those performed in the region of 2θ ~25° and upwards. Bragg peaks seen at these angles give information about periodicities in the sample at length scales of less than ~2Å. These scans can only be performed with ease when the sample is on a crystalline substrate, such as Si, as the substrate Bragg peak will be very strong and sharp. This allows the sample to be easily aligned in the diffractometer - we set the sample and detector arm to a known Bragg peak of the substrate (e.g. 28.43° for (111) Si), and rock the sample in order to maximise counts. It is worth noting that this aligns the sample with respect to planes of atoms in the substrate, and not in the multilayer.

It is also important to use a monochromator for the X-rays in this regime - this is performed by a single reflection from an X-ray mirror placed between the sample and the detector. This removes spurious lines caused by both Cu-Kβ radiation and several lines from W which has sublimed from the filament in the X-ray tube onto the Cu target. The monochromator also causes the level of background counts to drop by over an order of magnitude, meaning that low intensity X-ray peaks can be more easily seen.

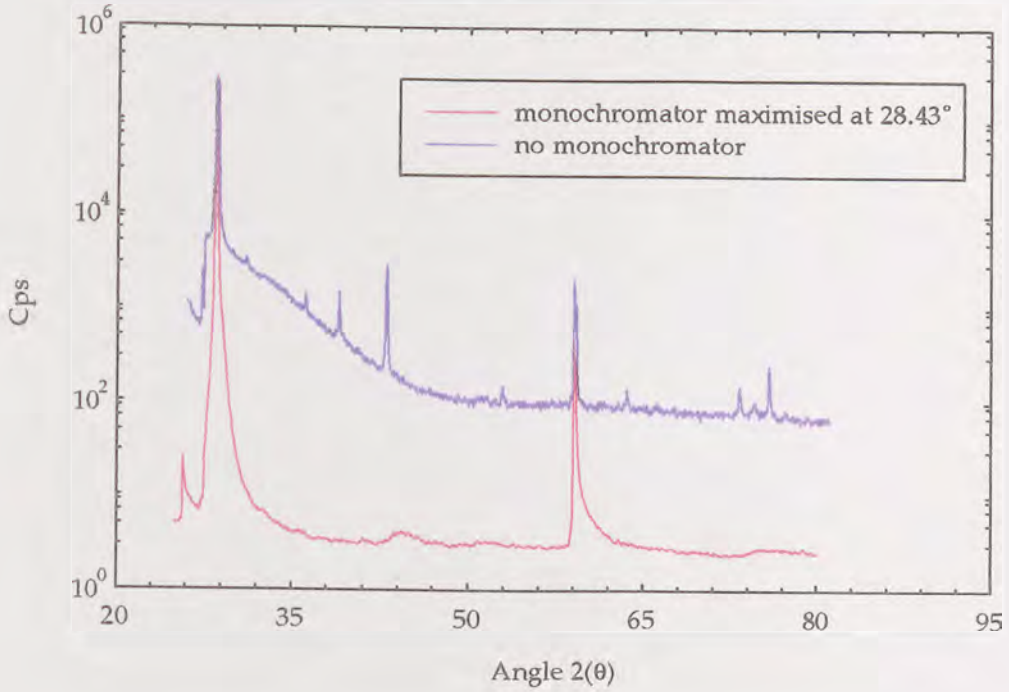

Figure 2.12 The importance of using the monochromator. Not only are many spurious lines removed from the spectrum, leaving only strong Si (111) and (222) peaks due to Cu-Kα, but also the noise floor is drastically reduced. This allows the very weak (111) texture of the multilayer to be seen around 43° in the monochromated scan.

It is useful to define a few terms at this point for the purposes of this thesis, which are somewhat loosely used in the literature. Films which in which the grains show a preferred orientation in the direction normal to the layers are said to possess *texture*. Films which are *epitaxial* are those in which the grains all share a close common orientation both normal to and in the

planes of the layers. Epitaxial films generally have a large grain size, although this a less rigorous use of the term epitaxy than that used in the semiconductor MBE community. *Polycrystalline* films have an isotropic distribution of grain orientations.

The preferred texture is often determined by the crystal structure - fcc films generally exhibit (111) texture, hcp films (0001) and bcc (001). These mean that atomic planes in the layers are close packed. This is of course not necessarily always the case, and different growth conditions can affect the texture which is adopted by a growing film. Different underlayers, not surprisingly, can have a strong effect on the final texture of a film.

The determination of film texture can be measured from high-angle diffraction spectra. The positions of individual Bragg peaks determine which set of lattice planes are in the plane of the film. The exact plane spacing can be affected by a number of other factors.

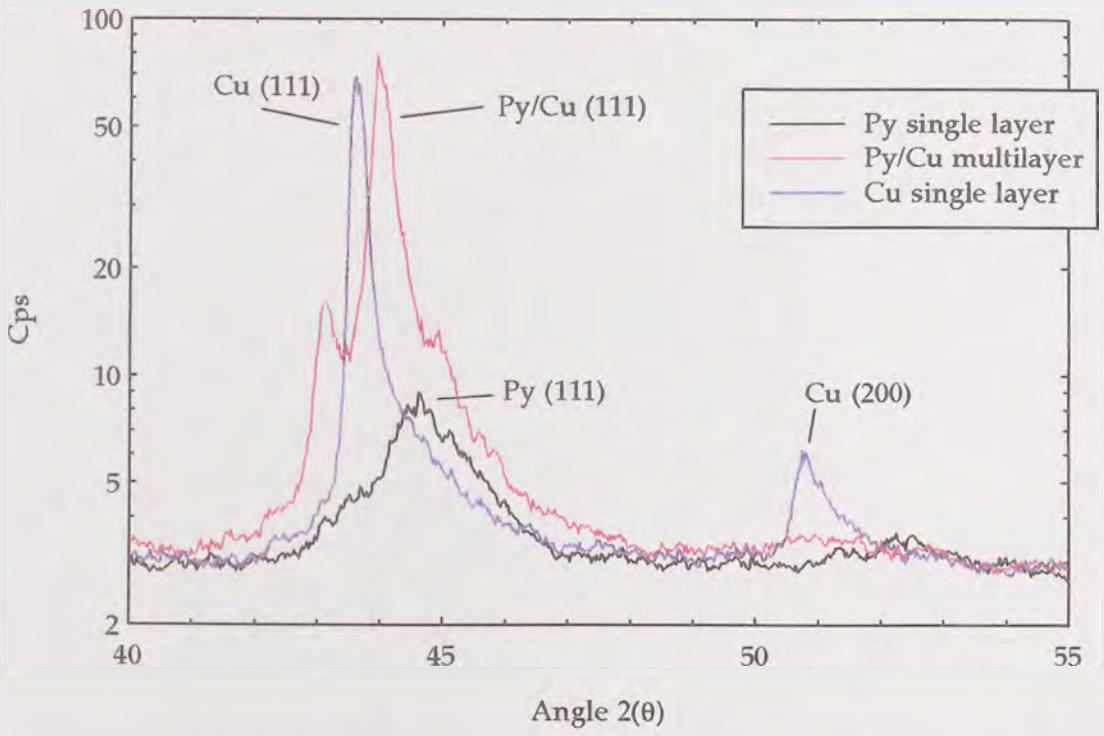

Figure 2.13 High angle X-ray data for permalloy (Py) and Cu.

This figure shows the high angle diffraction spectra of single films of Cu

and permalloy ($Ni_{80}Fe_{20}$). The (111) Bragg reflections are close together, as both materials have an fcc structure of similar lattice constant. The Cu film is more highly textured, showing a sharper, more intense Bragg peak. There is also some (200) texture visible. If the layers are strained then the position of the Bragg peaks can be slightly affected, as lateral strain is reflected in the inter-plane distance in the normal direction.

The graph also shows the high angle scan results for a multilayer of permalloy and Cu. The (111) peak is in a position that takes the weighted average of the two constituents of the sample. This is similar to the common metallurgical method of determining the composition of an alloy by measuring the Bragg peak position.

There are also two smaller peaks on the shoulders of the main (111) peak of the multilayer sample. These are called *satellites*, and their origin can be understood by considering the appearance of the superlattice in *k*-space. a superlattice has an enlarged unit cell in the growth direction, and this will be represented in *k*-space by additional points between those representing the atomic planes. These peaks also allow the bilayer thickness to be measured, as their positions will be determined by the modified Bragg equation

$$d = \frac{\lambda}{2(\sin\theta_{n+1} - \sin\theta_n)},$$

where the integer n is used to label the satellite peaks. We associate the main Bragg peak with the value n=0. There can be a large number of these superlattice Bragg peaks, for example in highly epitaxial semiconductor heterostructures such GaAs/AlAs superlattices[55]. However in sputtered samples where the grain size is typically only ~100Å, seeing the n=1 satellites is unusual.

2.3 TRANSPORT MEASUREMENTS AND MAGNETOMETRY

2.3.1 Resistivity and Magnetoresistance

2.3.1.1 Measurement methods

One of the most striking properties of magnetic multilayers is the Giant Magnetoresistance. In the Co/Cu system the GMR response is usually large, and hence easy to measure. A computerised four point probe method using dc current was employed to measure the magnetoresistance. The sense current was supplied by a stable current source, and the signal voltage was measured with a voltmeter with nanovolt sensitivity. The sample holder was in the form of a stick, made in order to allow low temperature measurements in a small gas-flow cryostat. The probes were spring loaded contact pads which make good contact with the metal film when pressed down. The four probes were spaced at intervals of 2.5mm. A test for good contact is to look for Ohmic behaviour; i.e. current reversal gives a near equal but opposite voltage, and the *I-V* characteristic is linear.

The computer controls the magnetic field by ramping an analogue voltage which is input to a unipolar power supply. This drives a large electromagnet which is capable of supplying a field of up to 1.5T. The current direction may be switched by large relays to give a bipolar output. The field is applied in the plane of the layers, and is measured for every data point using a small Hall sensor. The resistance is measured for both current directions and averaged, to avoid the effects of thermally induced emfs. The form of the sample holder allows longitudinal ($I//H$) and transverse ($I \perp H$) measurements to be made. This allows the AMR to be measured and subtracted off for samples that have a GMR of only a few percent. The resistance is calculated from the known current and logged to a data file.

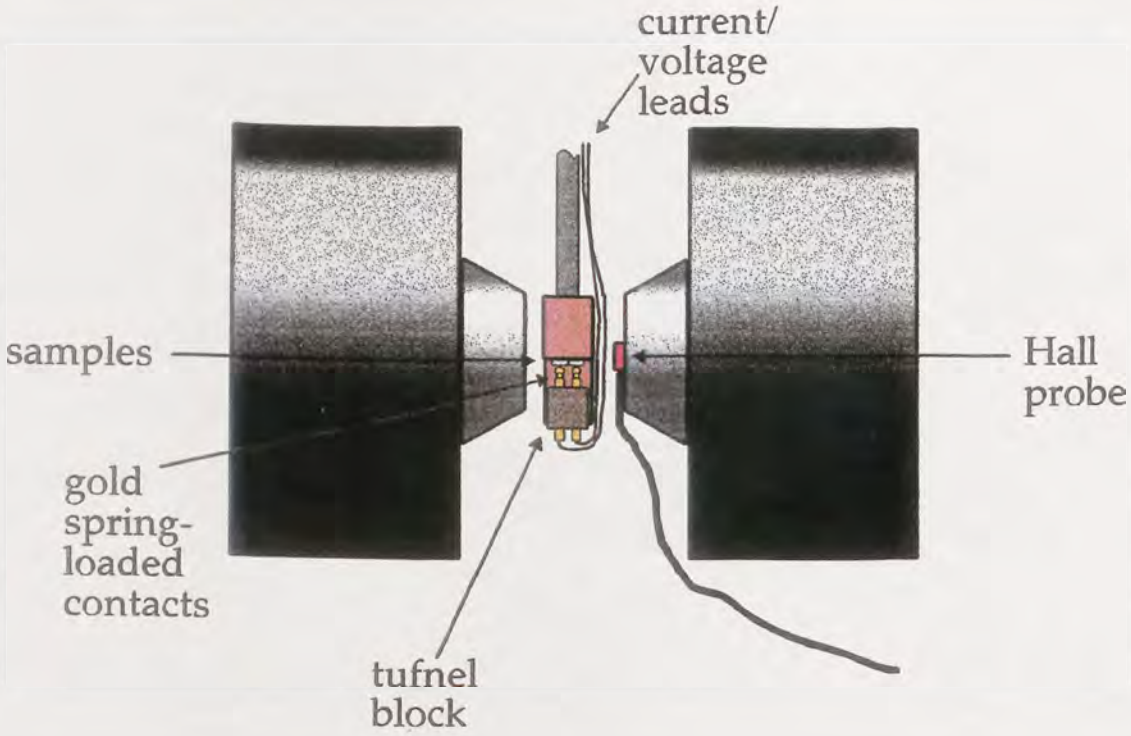

Figure 2.14 The room temperature magnetoresistance apparatus. The samples are inserted between the poles of a large electromagnet on the end of a stick. The samples are here drawn end-on, the current flows into the page. The stick may be rotated to allow the current to flow parallel to the field.

2.3.1.2 Sheet resistance and correction factors

It is common in thin film work to quote a quantity called the sheet resistance, $R_{\square}$. It is easily measured using a four point probe technique. It is defined by a modified version of Ohm's law, $R_{\square} = \kappa \times (V/I)$, and measured in $\Omega/\square$. Here κ is a correction factor determined by the geometry of the measurement, and accounts for a non-uniform current distribution in the sample. The resistivity of the sample is then defined as $\rho = R_{\square} t$, where t is the total film thickness.

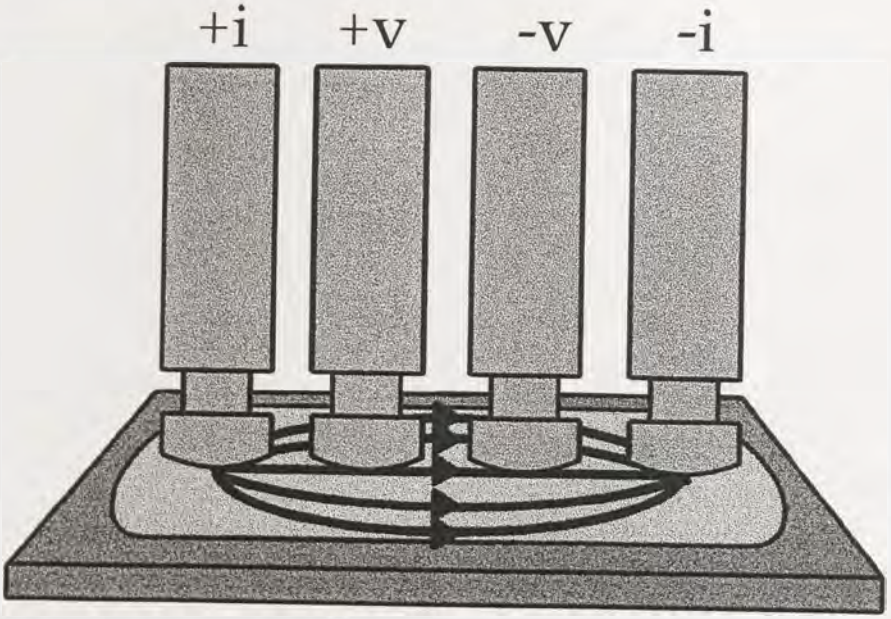

Figure 2.15 The four-probe probe geometry used for measuring the GMR and resistivity of the samples. The resistivity of the region between the two voltage probes is measured. The correction factor is due to the non-uniform current distribution between these probes

The correction factors for rectangular samples are given in the table below[56], where the sample is of length *a* and width *d*. The probes are *s* apart, and are on a line parallel to the length of the sample. For large *d/s* the κ tends towards a value for an infinite 2D sheet, κ=4.53. The value of κ approaches unity for large *a/d* and small *d/s*; that is, for a long thin sample. In this case the current flow in the region between the voltage probes is almost uniform.

The samples were in the form of long thin strips, in order to keep κ as close to 1 as possible. The samples were typically of dimension 12mm×3mm, those deposited through contact masks had a strictly defined width of 2mm. For such samples the correction factor κ is clearly almost unity.

d/s	Square a/d=1	a/d=2	Rectangle a/d=3	a/d≥4
1.0			0.9988	0.9994
1.25			1.2457	1.2248
1.5		1.4788	1.4893	1.4893
1.75		1.7196	1.7238	1.7238
2.0		1.9475	1.9475	1.9475
2.5		2.3532	2.3541	2.3541
3.0	2.4575	2.7000	2.7005	2.7005
4.0	3.1137	3.2246	3.2248	3.2248
5.0	3.5098	3.5749	3.5750	3.5750
7.5	4.0095	4.0361	4.0362	4.0362
10.0	4.2209	4.2357	4.2357	4.2357
15.0	4.3882	4.3947	4.3947	4.3947
20.0	4.4516	4.4553	4.4553	4.4553
40.0	4.5120	4.5129	4.5129	4.5129
∞	4.5324	4.5325	4.5325	4.5324

2.3.1.3 Thin film size effects

The extreme thinness of these films imposes boundaries on the motion of the transport electrons, as a significant fraction will now impinge on the film surfaces. This limits the mean free path of those electrons travelling in directions close to the film normal. As the film becomes much thinner than the bulk mean free path, ℓ, a smaller and smaller fraction will be able to experience this full length of travel. The fraction will be given roughly by $\sin(t/\ell)$ where t is the film thickness.

Fuchs solved the Boltzmann equation using boundary conditions appropriate to thin films with diffusive surfaces[57]. His work was later extended by others, in particular Sondheimer, Lucas and Chambers, who generalised the basic model. Fuchs' basic theory captures the important points of the topic, and the main results will be summarised here.

We will define ρ_F as the resistivity of the thin film, and ρ_B as the bulk value for the material in question. The symbol γ will be used for the ratio t/ℓ. The solution of the Boltzmann equation leads to

$$\frac{\rho_F}{\rho_B}=\frac{\phi(\gamma)}{\gamma} \text{ where } \frac{1}{\phi(\gamma)}=\frac{1}{\gamma}-\frac{3}{8\gamma^2}+\frac{3}{2\gamma^2}\int_1^\infty\left(\frac{1}{a^3}-\frac{1}{a^5}\right)e^{-\gamma a}da\,.$$

The limiting form for large γ is given by

$$\frac{\rho_F}{\rho_B} = 1 + \frac{3}{8\gamma}.$$

This approximation is actually remarkably good for values of γ as low as 0.1, although it does improve for γ>1. This provides a method for the measurement of ℓ. If we measure the resistivity of a series of samples of different known thicknesses, and plot $\rho_F t$ against t we should obtain a straight line. This line will have slope ρ_B and y-intercept $\frac{3}{8}\rho_B \ell$. A fuller discussion of this topic, including the effects of specular reflection at the surfaces is given by Chopra[58].

2.3.2 *Magneto-Optic measurements*

A convenient means of measuring the hysteresis loop of a thin magnetic film is the use of the Magneto-Optic Kerr Effect (MOKE). By sampling only a very small volume (the product of the area of the laser spot and the skin depth of the material), the technique measures only the sample itself. The substrate is never measured as in methods such as Vibrating Sample Magnetometry (VSM) and SQUID magnetometry, which measure the entire sample. A large diamagnetic contribution from the substrate is superimposed on the measured magnetisation with these techniques.

The apparatus used in this measurement is shown in the figure below. A large electromagnet is used, as in the GMR apparatus described above. The computer controls and measures the applied field in a similar manner. The HeNe laser is linearly polarised, and then reflected from the surface of the sample. The reflected beam then passes through the analyser, and falls onto a photodiode, which is connected to a digital voltmeter via a broadband amplifier. The temperature of the sample cannot be changed from ambient.

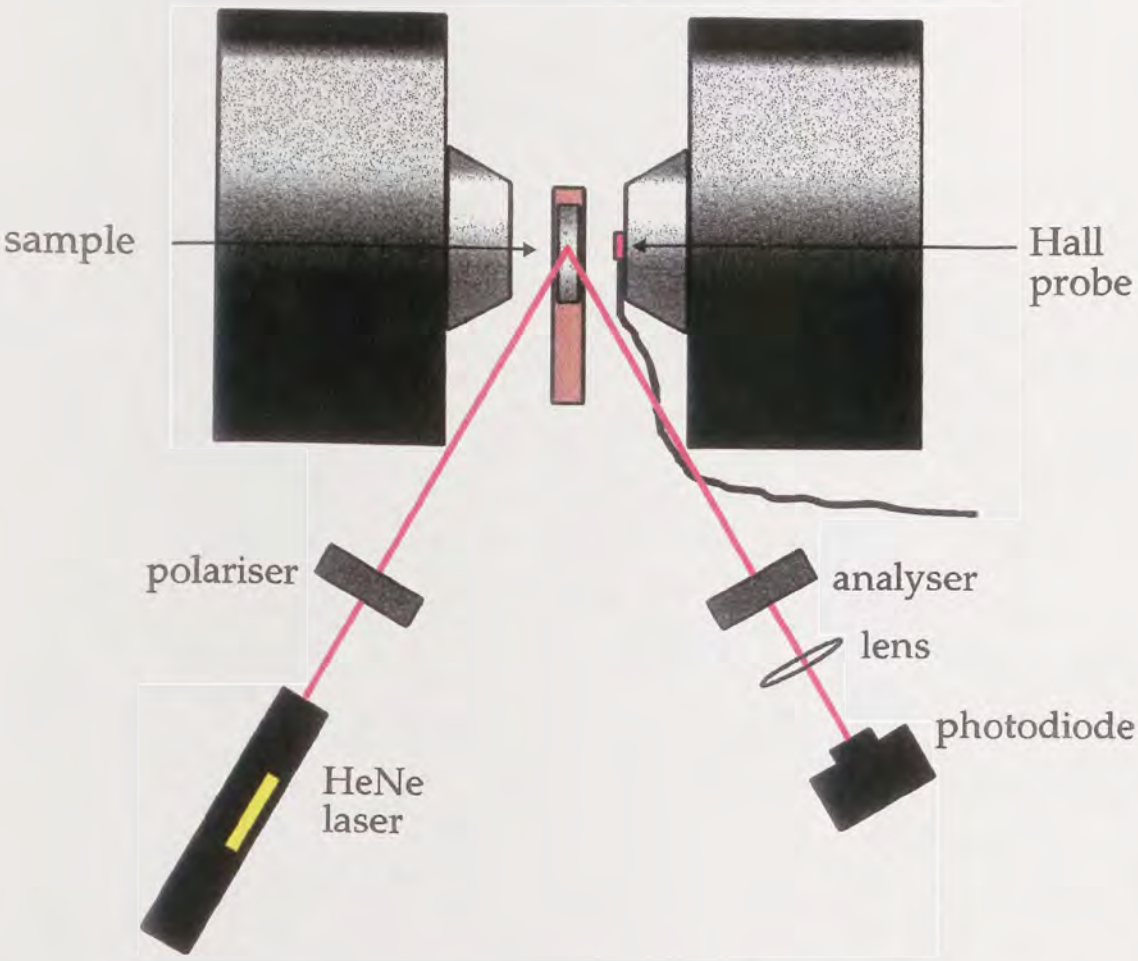

Figure 2.16 The MOKE apparatus. The laser is plane polarised, and then reflected from the sample surface. The beam is then analysed, and focused by a lens to a spot on the photodiode detector.

The analyser setting is important. It should be set close to extinction in order to ensure a large fractional change in measured laser intensity. However this is the least linear part of the $\cos^2\theta$ response curve, and for settings too close to extinction the response is no longer monotonic. A balance between these two extremes gives the optimum setting.

2.4 SUMMARY

In this chapter the main experimental methods employed in the multilayer studies were described. These fall into two main areas - the deposition of the films, and the subsequent characterisation. The development of the sputtering system was a major undertaking, and a large

number of new parts have been installed. Once the system was in a working condition a large amount of development was required to produce samples which exhibited a significant GMR.

X-ray analysis was the primary tool used for structural characterisation of the samples, and is particularly useful for determining the thicknesses of the individual layers. MOKE is a convenient and fast method of doing magnetic characterisation, although the absolute moment cannot be determined. Measuring the magnetoresistance is of course essential in the study of these type of samples.

3. INDIRECT EXCHANGE COUPLING

3.1 INTRODUCTION

The study of the coupling of thin magnetic films through metallic spacers has a long history. At the beginning of this century Maurain electroplated copper and then iron onto an iron wire[59]. He observed that the electroplated iron shell became magnetised in the same direction as the iron wire, provided that the copper spacer was sufficiently thin, and was unable to explain this phenomenon. The magnetostatic interaction between two magnetised bodies will tend to align their magnetisations anti-parallel when they are side by side, as shown below. This will be true as they are moved closer and closer together, indeed they may become arbitrarily close.

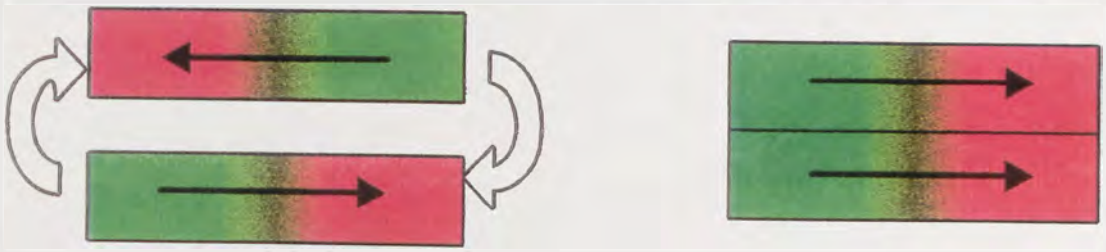

Figure 3.1 Two ferromagnetic bodies will align antiparallel when they are fairly widely separated, in order to minimise the magnetostatic energy contained in the stray field. If they are brought into intimate contact so that we may consider them as one piece of material then the direct exchange interactions will cause the magnetisations to lie parallel.

If the two bodies are brought into contact and considered as a single piece of material then they can share conduction electrons, and the magnetisation across the 'boundary' will align due to the usual ferromagnetic exchange interactions. In the 1960s there were observations similar to Maurain's, of long-range ferromagnetic coupling of ferromagnetic films

separated by spacers of between ~50 to a few hundred Å[60]. This was observed with spacers consisting of Ag, Au, Cr, Pd, Cu and In. These results were partly interpreted in terms of contemporary theoretical results showing that a long range exchange interaction could indeed be mediated by the conduction electrons of a nonmagnetic spacer layer[61]. However it was shown that, at least in some cases, the positive coupling was caused by ferromagnetic bridges or *pinholes* in the spacer[62].

In 1986 Grünberg *et al* observed the first hint of something new. They observed that for the proper thickness of a Cr interlayer, the magnetisations of two Fe films were coupled antiferromagnetically[63]. It was then found by Parkin *et al.* that there was not only one region of antiferromagnetic coupling, the sign of the coupling oscillated as the thickness of the spacer was increased, and this occurred in Co/Cr and Co/Ru as well as Fe/Cr[64]. This was also then observed in Co/Cu[65] and Fe/Al and Fe/Au[66]. The oscillatory nature of the coupling was found to be quite general for transition metal spacers in a thorough study by Parkin[67]. Further experimental results showed that for certain particular systems the coupling oscillation could even be multi-periodic[68].

3.2 Theoretical Models

There have been some attempts to calculate the exchange coupling directly as the energy difference between the ferromagnetic and antiferromagnetic states, either *ab initio*[69,70], or within a tight binding scheme[71,72]. Such calculations are extremely difficult, as the energy difference is many orders of magnitude smaller than the total energy of the system. This leads to numerical inaccuracy, and also a lack of transparency in the physical picture of the coupling. There have been a number of attempts to describe the coupling mechanism in terms of simpler physical concepts, and these will be described below.

3.2.1 RKKY interactions

An obvious way to interpret an oscillatory indirect coupling is by reference to the Ruderman-Kittel-Kasuya-Yosida (RKKY) interaction. This was originally developed by Rudermann and Kittel to describe the interactions of nuclear spins of impurities in metals[73], and was extended by Kasuya[74] and Yosida[75]. Indeed this oscillatory form for the spin density distribution in non-magnetic overlayers was predicted theoretically long before it was observed[76]. The RKKY model deals strictly with the interaction between a point magnetic impurity embedded in a nonmagnetic matrix.

The Fermi gas of a host metal naturally tries to screen the charge of an impurity ion core. However the fact that the values of $\boldsymbol{k}$ available to the conduction electrons are cut off at $\boldsymbol{k}_F$, the Fermi wavevector, means that screening at very small length scales is not effective. There is an electron density oscillation around the impurity atom[77]. Analogously, spin density decays away in an oscillatory fashion around an magnetic impurity[78], changing sign with a characteristic period Λ given by $\Lambda=\pi/k_F$. If the metal does not have an isotropic free electron-like Fermi surface then this spin density oscillation will naturally also be anisotropic.

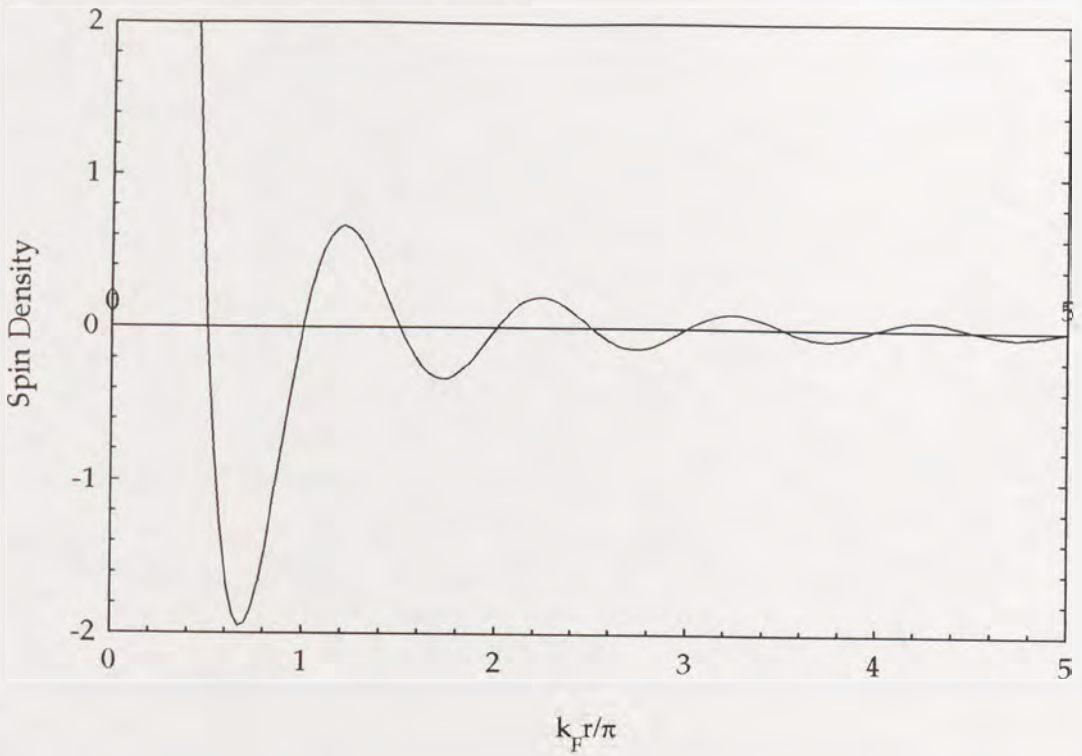

Figure 3.2 Spin density of the free electron gas in the neighbourhood of a point magnetic impurity at r=0, where k_F is the wave vector at the Fermi sphere.

We may extend this to cover interlayer coupling by summing the interactions over all the magnetic atoms in the two layers. It is generally necessary to do this only for the interfacial layer of spins in each layer to achieve a result of acceptable accuracy. These ideas were used initially to describe the interactions in rare-earth/Y superlattices[79], in particular by Yafet[80]. Here the spins are localised on the atoms in the core 4*f* states, and the RKKY model is clearly valid.

The application of these ideas to the problem of describing the varied results observed in transition metal multilayer coupling experiments followed soon after. Here the spins have a largely itinerant character. A particular problem is that the RKKY period given above is too short (~2Å) to describe the experimental results which typically find a period ~10Å. It was suggested that the discrete nature of the spacer thickness caused an *aliasing* effect,

where the rapidly oscillating spin-density distribution could only be sampled at a step size of the lattice spacing in the growth direction[81]. This discrete sampling yields a period given by $\Lambda = \left[\frac{k_F}{\pi} - \frac{n}{d}\right]^{-1}$, where d is the lattice spacing and n is an integer. For d close to π/k_F this can give a long period close to the observed value. This is equivalent to k_F approaching the Brillouin zone boundary.

A long paper by Bruno and Chappert sets out the application of the RKKY model to transition metal superlattices[82]. They correctly predicted the multiperiodic behaviour of certain systems, and achieved reasonable accuracy in predicting the various periods. However they were not able to predict the phase of the coupling oscillation or its amplitude, due to the model not taking correctly into account the non-local character of the spins in ferromagnetic 3*d* transition metals.

3.2.2 Quantum wells

Another conceptual paradigm for interpreting this phenomenon was given by Edwards and Mathon[83], and has been developed over the years. This describes the coupling in terms of quantum well states in the spacer, and is analogous to the de Haas-van Alphen effect. In the dH-vA effect the application of a magnetic field quantises the energy levels in 2D of the conduction electrons. As the field is increased, each of these discrete energy levels passes through the Fermi level and becomes unoccupied. This causes an oscillation in the susceptibility of the metal. In the quantum well picture, magnetic carriers are confined in a potential well in the spacer layer, and their energy levels are quantised in 1D. As the well width is reduced, the energy levels are raised, and as each passes through the Fermi level, the sense of the coupling oscillates.

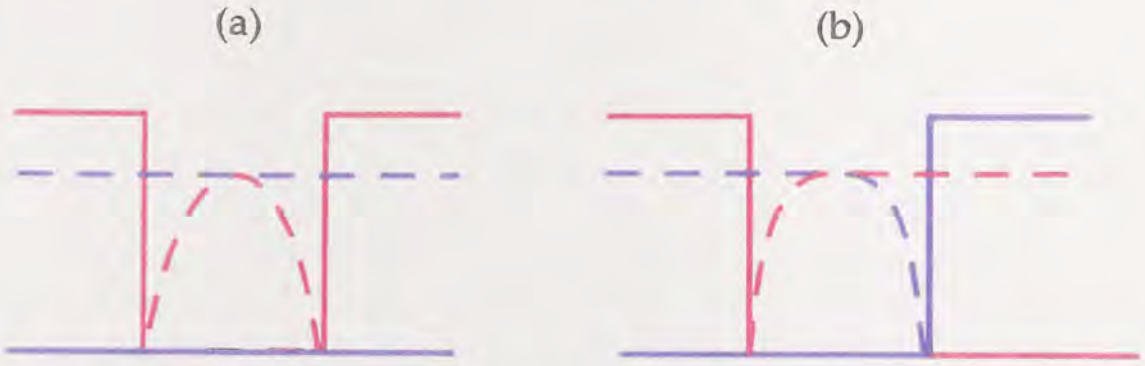

Figure 3.3 Spin dependent potentials and carrier densities (broken lines) for a magnetic trilayer sandwich, drawn for (a)ferromagnetic and (b) antiferromagnetic alignment. Red lines refer to the potentials experienced by (solid) and densities (broken) of spin-up electrons or spin-down holes, blue refers to spin-down electrons or spin-up holes.

In the above figure the potentials in which the conduction electrons move is shown for a two thick magnetic layers separated by a non-magnetic metal spacer. It is assumed, for the sake of simplicity only, that the ferromagnet is strong, and that the minority band is of the same form as the spacer *d*-band. This is reasonable for a system such as Co/Ru. The potential is spin-dependent inside the ferromagnetic layers, as the d-bands are exchange split. The potentials are drawn in both the parallel and antiparallel alignments. Since the majority band is full in the ferromagnet it is convenient to discuss the motion of holes rather than electrons.

When the magnetic alignment of layers is parallel, holes in the spin-down band (which are of course themselves spin-up particles) are able to travel through the whole structure, as there are empty states in every sub-band. Spin-down holes however are confined to the spacer, as the spin-up band is filled in the magnetic layers.

When the layers are anti-parallel then holes of either spin are able to move between the spacer and one of the two ferromagnetic layers. Spin-down holes are confined to the half-space to the right of the first interface, and spin-up holes are confined to the left of the second interface. The spin-up and down carrier densities are also drawn on the diagram to illustrate this

point.

One of the consequences of the Heisenberg uncertainty principle is that the confinement of quantum particles costs energy. It is necessary now to determine which of the two forms of confinement has the smaller energy cost for a given spacer thickness. We must determine the sign of the quantity $\Delta E = E_{\uparrow\uparrow} - E_{\uparrow\downarrow}$, where $E_{\uparrow\uparrow}$ is the energy in the parallel state, and $E_{\uparrow\downarrow}$ the energy of the antiparallel state.

It can be shown that this is equivalent to $\Delta E(N) = E(N) - E(\infty)$, where $E(N)$ is the kinetic energy of spin down holes confined to the N atomic planes of the spacer, and $E(\infty)$ is the energy of free carriers[84]. In fact as the width of the well is varied the shape of the density curve may well change, and in order to preserve the electrical neutrality of the spacer, the number of particles will also change. We must therefore actually deal with thermodynamic potentials, and treat the expression $\Delta\Omega(N) = \Omega(N) - \Omega(\infty)$.

If we assume that the spin down holes are confined between two infinitely high potential walls a distance $L=Nd$ apart, but that they are free to move in the layer plane, then a simple particle-in-a-box calculation leads to the energy of a particle being given by

$$E(n,k_{\parallel}) = \frac{\hbar^2}{2m}\left[\left(\frac{n\pi}{L}\right)^2 + k_{\parallel}^2\right],$$

where m is the particle mass, $k_{\parallel}$ is the in-plane wave vector and n is an integer labelling the 1D quantised energy level. The thermodynamic potential $\Omega(N)$ is obtained by adding up all the one-particle energies and counting all the occupied states up to the Fermi level,

$$\Omega(L) = \int_0^{E_F} (E - E_F)[D^{conf}(E,L) - D^{bulk}(E,L)]dE$$

where $D^{conf}(E,L)$ is the density of states of the confined particles, and $D^{bulk}(E,L) = (L/2\pi^2)(2m/\hbar^2)^{3/2}E^{1/2}$ is the density of states of free particles in a slab of unit surface area and thickness L[85].

This $\Omega(L)$ is now the coupling energy between the two magnetic layers, and is given by the difference in the density of states of the confined

particles, and the bulk. The bulk density of states takes its normal parabolic form for free particles. Let us now turn to the form of $D^{conf}(E,L)$.

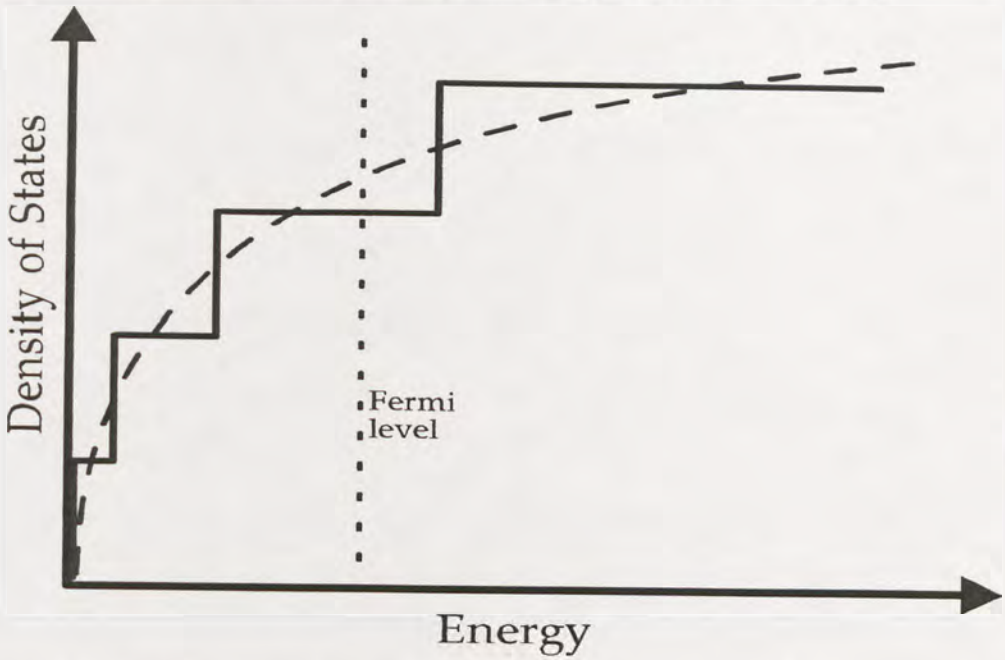

Figure 3.4 Density of states of confined spin-down holes, and of free electrons in the bulk (broken line).

The confined particles are forbidden to have energies below the first 1D quantised level, the zero point energy $(\hbar^2/2m)(\pi/L)^2$. So up to this energy the density of states is zero. For energies between the first and second discrete levels the system is equivalent to free particles moving in a plane, for which the density of states is a constant $(1/2\pi)(m/\hbar^2)$. Hence there is a step of this height at the first 1D quantised level. It follows that there is another sharp increase of $(1/2\pi)(m/\hbar^2)$ as each new 1D level becomes occupied. As the step positions go like n^2, this staircase-like density of states follows the parabolic free particle form, but *oscillates* about that smooth curve. As we increase the value of L we will linearly increase the bulk density of states and allow the confined density of states to keep up by reducing the step width. Hence for a fixed Fermi level, as the spacer thickness increases the coupling will oscillate in sign. Of course the small changes in the number density of carriers will mean that the Fermi level is not exactly fixed, but the changes are small enough that the basic model is correct. Once the discrete nature of

the spacer is again taken into account, the theory predicts the observed long periods.

This fairly transparent physical picture has allowed quite accurate predictions of a number of properties of coupled multilayers - the period and magnitude of the coupling observed in Co/Ru by Parkin, the trend in coupling energy with number of *d*-electrons (also observed by Parkin)[86], the correct form for the coupling in (111)[87] and (001) Co/Cu[88], and the strong temperature dependence of the coupling observed in transition metal systems[89]. Experimental evidence for these quantum well states has also been found by inverse photoemission[90].

3.2.3 A unified picture

These models and other related calculations share a number of common features. All the models have at their heart a *superexchange* mechanism, the polarisation of the spacer conduction electrons by one magnetic layer, which then interacts with the second magnetic layer on the far side of the spacer. The period of the oscillations is always derived by reference to the extremal spanning vectors of the spacer material Fermi surface. The envelope of the oscillations is of the form $1/L^2$.

This commonality was made explicit by Bruno in his unified picture described in a paper in 1993[91]. He considers a conduction electron crossing the spacer represented by a Bloch wave of momentum $\boldsymbol{k}_i$. As it passes from spacer to magnetic layer it experiences a change in potential, and hence the wave function is partially reflected back into the paramagnet. This reflected Bloch wave of momentum $\boldsymbol{k}_r$ will interfere with the incident wave, and a standing wave will be set up in the spacer. The associated electronic density will oscillate with a period given by the scattering vector $\boldsymbol{q}=\boldsymbol{k}_r - \boldsymbol{k}_i$. For a perfect multilayer structure, $\boldsymbol{q}$ will be exactly normal to the layers, and will also be independent of electron spin. However the reflecting potential step does depend on spin, and so the standing wave will be spin polarised. The net polarisation will be due to the sum of all the electrons of different $\boldsymbol{q}$, and

so will decay away from the interface.

The reflected Bloch wave will reflect again once it has crossed the spacer, and multiple reflections from the interfaces will take place. The energy of the interferences will oscillate with a period of $2\pi/q$, and for electrons at the Fermi level this period will be $\pi/2k_F$. These oscillations are the only ones that do not largely cancel out, and so we find the same period as for the RKKY, quantum well and other models.

The key parameter in determining the strength of the coupling is the spin-asymmetry of the reflection coefficients. It is possible to determine these reflectivities in a number of ways. If these quantities are calculated *ab initio*, then this provides an essentially first principles total energy calculation. If the interfaces are described as 2D arrays of localised spins then the RKKY model is recovered, for a tight-binding model with the spin-up and down reflection coefficients of zero and unity then the basic quantum well picture is obtained. For free electrons between spin-dependent energy barriers then the model becomes free electron model of Hathaway and Cullen[92].

It is of course possible for reflections to occur within the ferromagnetic layers, and so we should also expect to observe oscillations with respect to the magnetic layer thickness[93,94]. Indeed even varying the thickness of a capping layer outside the superlattice can cause coupling oscillations[95]. As Slonczewski had also noted, these oscillations are not purely sinusoidal, and this anharmonicity will lead to non-Heisenberg-like terms in the coupling energy.

3.2.4 Non-Heisenberg exchange coupling

3.2.4.1 Intrinsic contributions

The bilinear Heisenberg Hamiltonian may be regarded as the first term in a power series in $\mathbf{S}\cdot\mathbf{S}$. The terms of higher order than linear are usually ignored in calculations of bulk properties. However a number of experimental results on the indirect exchange coupling through thin spacers show that at least the first of these higher order terms $(\mathbf{S}\cdot\mathbf{S})^2$ is of

importance. There have been a number of attempts to derive this *biquadratic* term directly from the same model as the bilinear coupling[96,97]. The coupling terms are then written as $J_1\mathbf{S}\cdot\mathbf{S} + J_2(\mathbf{S}\cdot\mathbf{S})^2$. All of these intrinsic mechanisms predict $J_2 << J_1$, contrary to the results of experiment. It is possible that J_2 is non-zero at the some of the nodes in the oscillation of J_1, but on the whole in order to explain the experimental observations extrinsic mechanisms must be sought.

3.2.4.2 Loose spins

Slonczewski predicted in 1993 that lone magnetic impurities in the spacer could cause orthogonal coupling of the moments with a rapid temperature dependence[98]. The spins are coupled to the magnetic layers by the usual Heisenberg indirect exchange field. At high temperatures the Curie susceptibility of the spins is independent of this exchange field, and they contribute only a correction to J_1. At low temperatures, the spins may be brought close to saturation by the exchange fields, and their polarisation response is no longer linear. This non-linearity means that our power series in $\mathbf{S}\cdot\mathbf{S}$ does not converge so rapidly, and we must include higher order terms.

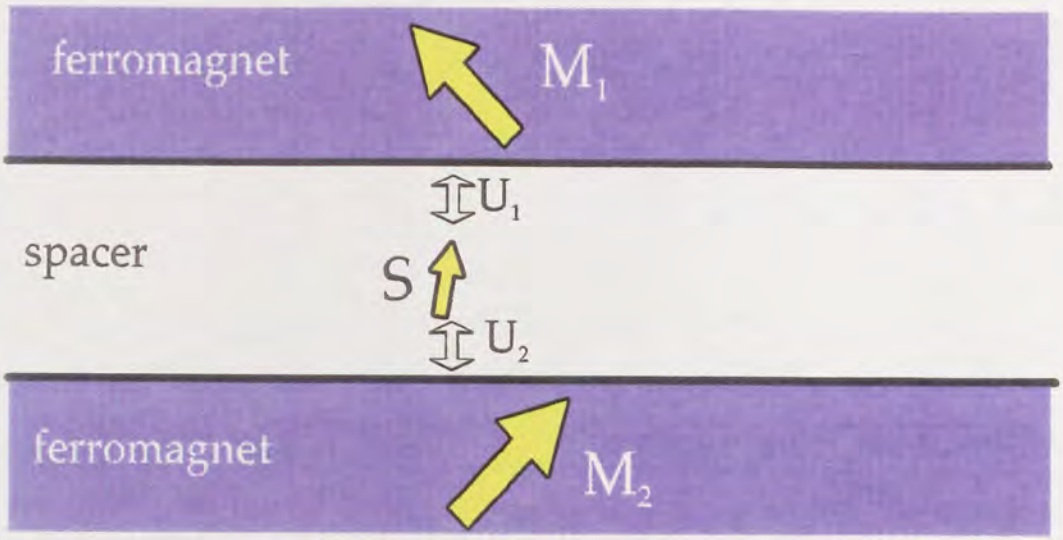

Figure 3.5 A loose spin in the spacer layer will interact with the magnetisations M_1 and M_2 through exchange coupling fields U_1 and U_2. The low temperature non-linear susceptibility of the spins can allow for 90° coupling with a rapid temperature dependence.

Let us place in the spacer a single atomic electron state, with spin quantum number S and momentum operator $\hbar\mathbf{S}$. It is subject to exchange coupling fields $\mathbf{U}_1$ and $\mathbf{U}_2$ from the conduction electron polarisation due to magnetic layers 1 and 2. The vector sum of these fields gives us the effective local spin Hamiltonian $H=(\mathbf{U}_1+\mathbf{U}_2)\cdot\mathbf{S}/S$.

The energy levels of the defect are now $E_m=-Um/S$, where the integer m=$-S,-S+1,\ldots S$. We may write

$$U(\theta)=|\mathbf{U}_1+\mathbf{U}_2|=\sqrt{U_1^2+U_2^2+2U_1U_2\cos\theta}$$

where θ is the angle between the layer magnetisations. The free energy of the spin $f(T,\theta)$ may be derived from conventional statistics, and the bilinear correction and biquadratic coefficient for N such loose spins are given by

$$J1=N\left[f(\pi)-f(0)\right]/2,\quad J_2=N\left[\tfrac{1}{2}f(0)+\tfrac{1}{2}f(\pi)-f(\pi/2)\right].$$

It is the term $f(\pi/2)$ which leads to orthogonal ordering. There is now experimental evidence to support this model as describing the mechanism of biquadratic coupling in the Fe/Al system[99].

3.2.4.3 Thickness fluctuations

Another mechanism which is of importance in real multilayered structures was also first treated theoretically by Slonczewski[100]. If there are thickness fluctuations in the spacer layer then the value of J_1 is not a constant across the area of our prototypical magnetic trilayer sandwich. If these coupling fluctuations are so great that there are regions which are positively coupled and others which are negatively coupled then we must perform a detailed micromagnetic calculation in order to determine the lowest energy state.

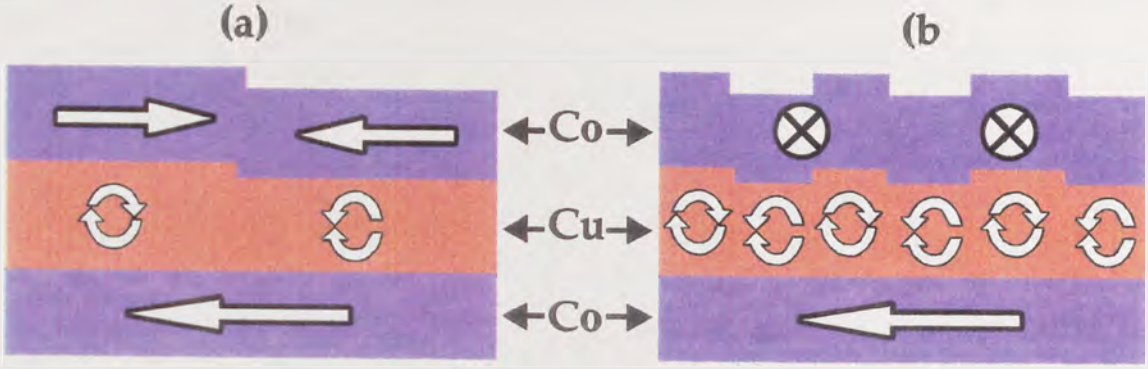

Figure 3.6 The effects of mixed-sign coupling caused by thickness fluctuations. The curved arrows represent the sense of the coupling. In (a) the lateral length scale of the fluctuations is long, and the exchange stiffness within a Co layer cannot prevent the coupling being satisfied everywhere. In (b) the exchange stiffness is effective over the shorter distances and the moments are frustrated.

In general there are two possible cases. Let us suppose that the multilayer roughness is in the form of terraces as shown in the diagram above, which are of length L. The thickness fluctuations cause changes in the bilinear coupling constant from terrace to terrace of magnitude $2\Delta J_1$. If L is very large then the intralayer exchange stiffness A is unable to maintain a constant direction for the magnetisation within a layer, and it is possible for domains to form. In this case the coupling is satisfied everywhere and a low energy state is attained.

If however the length scale L is short, then the exchange stiffness within a layer will not allow such a rapid variation in the direction of **M**. In this case the moments in the layers are frustrated, and an energy minimum can be found when the moments are orthogonal. We may write the effective value of the biquadratic coupling constant as

$$J_2 = \frac{2L(\Delta J_1)^2}{\pi^3} \sum_{i=1,2} \frac{\coth(\pi D_i / L)}{A_i},$$

for magnetic layers 1 and 2, of thickness D. This assumes L is much greater than the spacer thickness. In fact there will be small amplitude static spin waves in both magnetic layers, as the local bilinear coupling will relax the moments slightly away from their average directions. It is also possible for more complex arrangements of spins to arise[101].

One peculiar feature of this model is that J_2 increases for wider terraces, which correspond to increasing structural perfection. This has been observed by experiment[102].

3.3 Minimum Energy Calculations

Faced with such an array of complex theoretical schemes, it is often convenient to discuss experimental results in terms of a simple phenomenological model. Such a model can be used to extract from the raw data numerical results for the quantities of interest such as the saturation magnetisation, coupling energies and anisotropy constants. This allows comparison between experiments without reference to theory, as well as testing the theories themselves.

We proceed by writing down the total energy of the system as a sum of the various contributions of the all the effects present in the multilayer. For thin films it is sensible to discuss the energy per unit area of film, denoted ε. This energy is then minimised to determine the exact magnetic configuration in a given field. As the field is varied, the system will follow the path of minimum energy, and we will be able to trace out magnetisation and magnetoresistance loops. This is the approach used in the well known

Stoner-Wohlfarth model for small particles[103].

3.3.1 *The Zeeman term*

Any magnetic dipole **m** has an energy of interaction with an applied field H given by $-\mu_0\mathbf{m}\cdot\mathbf{H}$, called the Zeeman energy. A ferromagnetic body has a dipole moment per unit volume **M**, the normal definition of the magnetisation. If we wish to calculate the energy per unit area of a thin ferromagnetic film in an applied field then we must take into account the film thickness t, and the Zeeman areal energy density is given by

$$\varepsilon_{Zeeman} = -\mu_0 t\mathbf{M}\cdot\mathbf{H}\,.$$

We have made here the implicit assumption that **M** is not a function of position within the film. For a chemically homogeneous film the magnitude of **M** will indeed be a constant, but we have neglected the possibility that the film has broken into domains. Historically it has been believed that it is impossible to support a domain wall in a sufficiently thin film[104]. A typical Bloch domain wall, where the local magnetisation vector rotates in the plane of the wall, will generate a large number of free poles on the surfaces of a thin film. This is energetically unfavourable. However this may be avoided by the use of Néel walls, where the local direction of **M** rotates perpendicular to the wall plane, but in the plane of the film. However for extremely thin films (t<100Å) the wall width increases to very large values[105]. Single domain states have been inferred from hysteresis loops for various systems[106,107,108], and directly observed Co/Cu(100) films magnetised in plane[109].

For the purposes of this calculation we will assume that each magnetic layer forms a single domain. This is valid for reasonably large areas of multilayer, and is anyway necessary in order to make the problem tractable.

3.3.2 *Demagnetising effects*

A uniformly magnetised ferromagnetic body will have magnetic charges at its surfaces. These free poles will generate a *demagnetising field* $\mathbf{H}_d$, which

for an ellipsoidal body will be exactly anti-parallel to the magnetisation. The *demagnetising factor* is defined as $N=-\mathbf{H}_d/\mathbf{M}$. The magnetostatic energy of a body is given by $-\frac{1}{2}\mu_0\int\mathbf{H}_d\cdot\mathbf{M}dV$, where the integration is performed over the volume of the ellipsoid.

We may consider a thin film as an extreme case of an oblate ellipsoid. In this case the demagnetising factors are zero for a field applied in the film plane, and unity for a field applied exactly perpendicularly. We may then generalise the areal demagnetising energy density as

$$\varepsilon_{demag}=\tfrac{1}{2}\mu_0 t(\mathbf{M}\cdot\hat{\mathbf{n}})^2,$$

where $\hat{\mathbf{n}}$ is a unit vector normal to the film plane.

This means that there is a *shape anisotropy*, with a hard axis normal to the film, and an easy plane in the film plane. We may write the volume anisotropy constant $K=\frac{1}{2}\mu_0 M^2$. Again there are implicit assumptions: we have assumed that the film is uniform in representing it as an ellipsoid where the minor axis diameter has gone to infinity. Non-uniform films will have more complex behaviour as free poles may be generated on the surfaces. A full discussion is given by Dove[110].

3.3.3 Anisotropy

It is possible to induce an anisotropy in a ferromagnetic film by a number of means. Firstly oblique deposition can cause there to be an easy axis along the projection of the deposition direction in the film plane. This topic was never fully resolved, but may be due to the canted microstructural voids discussed in chapter 2 [111], or an internal strain[112], and oxygen may play some role[113]. This effect is not usually as apparent in sputtered films as in evaporated ones due to the spread in deposition angles caused by the sputter gas. It has however been observed, in films where the gas pressure is high and there is likely to be a zone 1 microstructure which contains voids[114].

Also growth of the film in an applied forming field can cause there to be an induced easy axis in this direction[115]. It is not necessary that this

field be magnetic[116], although this is usual, for practical reasons. Again the exact reasons are unclear. It is possible to induce an anisotropy in a ferromagnet by annealing in a field[117], and the condensation of adatoms onto a substrate has many of the characteristics of a fast quench.

This type of anisotropy can be described by a term like

$$\varepsilon_{uniaxial} = -K_u t(\hat{\mathbf{m}} \cdot \hat{\mathbf{a}})^2,$$

where $\hat{\mathbf{a}}$ is a unit vector along the easy axis and $\hat{\mathbf{m}}$ is a dimensionless unit vector parallel to the magnetisation direction. Values of K_u>0 are assumed, as this will lead to the required easy axis, rather than plane.

A second type of anisotropy takes effect at the ferromagnet-spacer interfaces. This is termed surface or interface anisotropy, and is largely due to the reduced symmetry at the surface[118], although the altered electronic structure caused by the overlayer plays a role[119]. This takes the functional form

$$\varepsilon_{surface} = -K_s(\hat{\mathbf{m}} \cdot \hat{\mathbf{n}})^2,$$

where K_s is the surface anisotropy constant. This anisotropy has an easy axis perpendicular to the film plane for K_s>0. It can dominate over the demagnetising term for sufficiently small film thicknesses, as it has no t dependence, resulting in perpendicular alignment even in zero field. For a Co/Cu interface the anisotropy is usually not strong enough to support an easy perpendicular direction, as it can be for systems such as Co/Au and Co/Pd[120].

The subject of magnetic anisotropy is both broad and deep and many important effects have been neglected here as being largely irrelevant to the special case in hand. There has been no mention of *magnetocrystalline anisotropy* as it is zero in permalloy and fcc-Co (though not hcp), which [188] generally takes higher symmetry orders than uniaxial, nor of *magnetostriction* induced anisotropy. A near book-length review of anisotropies in ultrathin magnetic films is given by Heinrich and Cochrane[121].

3.3.4 Interlayer coupling

3.3.4.1 Heisenberg bilinear coupling

We may represent the coupling of the normal Heisenberg form between two layers in the usual way,

$$\varepsilon_{bilinear} = -J_1 \hat{\mathbf{m}}_1 \cdot \hat{\mathbf{m}}_2$$

where $\hat{\mathbf{m}}_i$ represents a dimensionless unit vector in the direction of **M** in layer *i*. The coupling constant J_1 has dimensions of energy per unit area, and is a purely phenomenological parameter. The sign convention used is that positive values of J_1 correspond to ferromagnetic coupling, and negative values to antiferromagnetic coupling. It should be noted that this exchange energy is shared between a pair of layers.

3.3.4.2 Biquadratic coupling

Biquadratic coupling has an areal energy density of the form

$$\varepsilon_{biquadratic} = -J_2 (\hat{\mathbf{m}}_1 \cdot \hat{\mathbf{m}}_2)^2$$

where the symbols have similar meanings to those in the bilinear expression given above. Again J_2 is a phenomenological parameter, without reference to its possible cause, either intrinsic or extrinsic. The sign convention is that positive values lead to collinear coupling, and negative values to orthogonal coupling. The energy is again shared between a pair of ferromagnetic layers.

3.3.5 Emergent behaviour

All of these terms interact in complex ways. The Zeeman term alone will align the magnetisation into the field direction for arbitrarily small fields, and this will result in the magnetisation switching sharply and discontinuously from $+M_s$ to $-M_s$ as the field passes through zero. It is however rare to find a magnetic system which puts up so little resistance to the applied fields energy requirements.

3.3.5.1 Anisotropy & hysteresis

The effect of anisotropy is not only to align the magnetisation in zero

field, but also affects the shape of the **M-H** loop. This is true of shape anisotropy, as well as the various intrinsic and induced effects. When a field is applied in a hard direction it has to do work against the anisotropy term to rotate the magnetisation vector, and this means that a finite field value is required to saturate the magnetisation. This field value H_s is given by

$$H_s = \frac{2K_u}{\mu_0 Mt}.$$

However the system never leaves the global minimum in the energy landscape. This means that the system follows the same path as the field is both increased and reduced. However if the field is applied along an easy axis then the system can remain in a local minimum as the system is brought back from saturation. This results in *hysteresis*, the state of the system is not only determined by the current set of parameters, but also by previous sets. Only a discrete set of easy directions (e.g. uniaxial) will cause hysteretic behaviour, rather than, say, an easy plane. Of course another cause of hysteresis in real systems is the presence and pinning of domain walls, which we have neglected here.

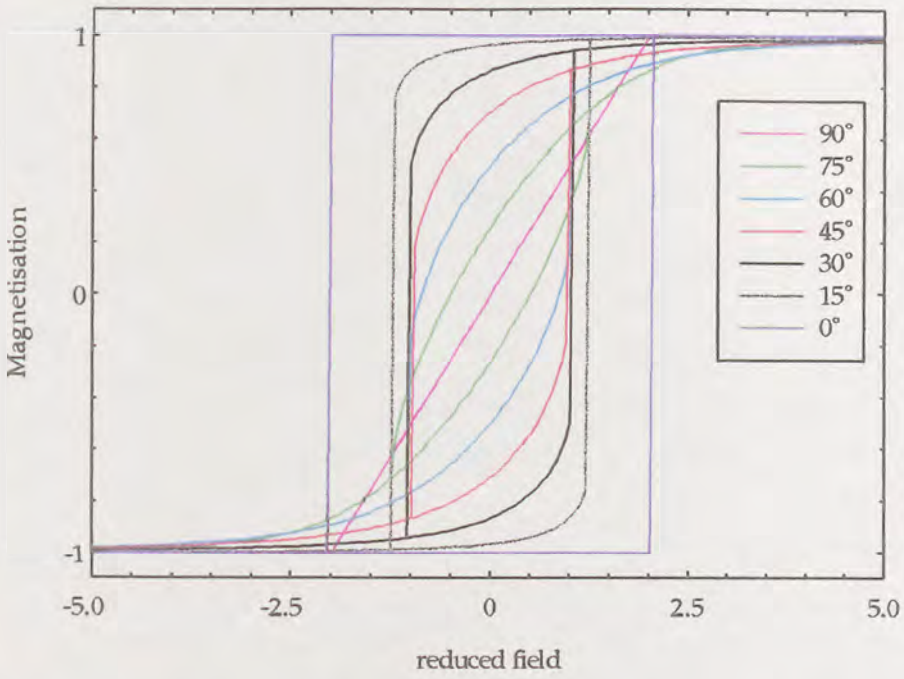

Figure 3.7 The predictions of the Stoner-Wohlfarth model for a single thin film with an in-plane easy axis, with the field applied at various angles in the plane. The reduced field is expressed as H/K_u.

3.3.5.2 Interlayer coupling

If we have a number of uncoupled magnetic films then we may minimise their energies individually before summing the resulting individual magnetisation vectors to find the total moment of the sample. For an ensemble of identical films then we need only calculate the properties as a function of field for one of them, and then multiply the results by N. If our experiment is one such as MOKE where we are unable to measure the total moment, but only ratios such as $M(H)/M_s$, then even this is unnecessary, and we need only calculate the properties of one film.

If we allow interactions between adjacent films then we introduce cross-terms into the energy. Let us first of all suppose that we ferromagnetically couple every pair of magnetic layers. If the layers are all identical, as we previously supposed, then there will be no difference in the calculated magnetisation loop, as the layer magnetisations were always parallel

anyway, without the coupling requiring them to be so. It is impossible to tell from magnetisation loops if identical layers are uncoupled, or positively coupled. On the other hand, if films with different individual magnetisation loops are coupled ferromagnetically, then there will be some averaging of the two hysteresis loops.

On the other hand, if we couple the films antiferromagnetically and first of all assume that there is no anisotropy, then at zero field the films magnetisation vectors will lie antiparallel and the total magnetisation of the sample will be zero (for an even number of magnetic layers). In order to saturate the sample the applied field must do work against the coupling energy, and a finite field is required to saturate the sample, given by

$$H_s = -\frac{2J_1}{\mu_0 Mt},$$

for a pair of ferromagnetic layers where J_1 is negative. In a superlattice where each layer is coupled to two others, J_1 is twice as effective, and the numerator is $4J_1$.

The form of the magnetisation loop is a straight line, as for a uniaxial system magnetised in a hard direction. This is not coincidental - suppose $\mathbf{M}_1$ makes an angle θ_1 with $\mathbf{H}$, similarly for $\mathbf{M}_2$. By applying the energy minimisation condition that $\frac{\partial \varepsilon}{\partial \theta_1} = 0, \frac{\partial \varepsilon}{\partial \theta_2} = 0$ it is possible to show that in this case the moments close symmetrically about the field direction, i.e. θ_1=-θ_2. For a particular magnetic layer the field is working against a term like $\cos^2\theta$, producing identical behaviour.

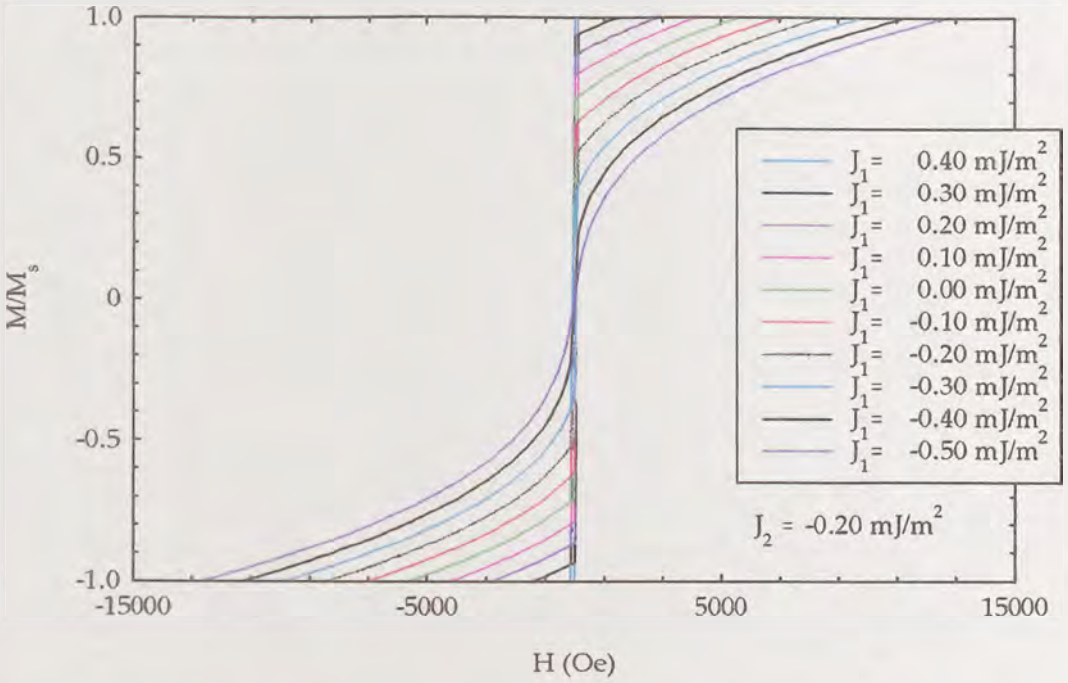

Figure 3.8 The results of numerically simulating the effect of varying the bilinear coupling constant for a pair of 1nm thick Co layers also displaying orthogonal coupling. For large positive or negative bilinear coupling the remanence returns to unity or zero respectively.

If we have also an anisotropy then the above symmetry considerations apply only in the case that the field is applied along a symmetry axis of the anisotropy. For a hard axis the loop is again a straight line, but if we apply the field along an easy axis then the system may again find itself in a local minimum, and hysteresis will result. This is generally not important in the sputtered samples which will be discussed in this thesis, and is covered in more detail by Bloemen *et al*[122].

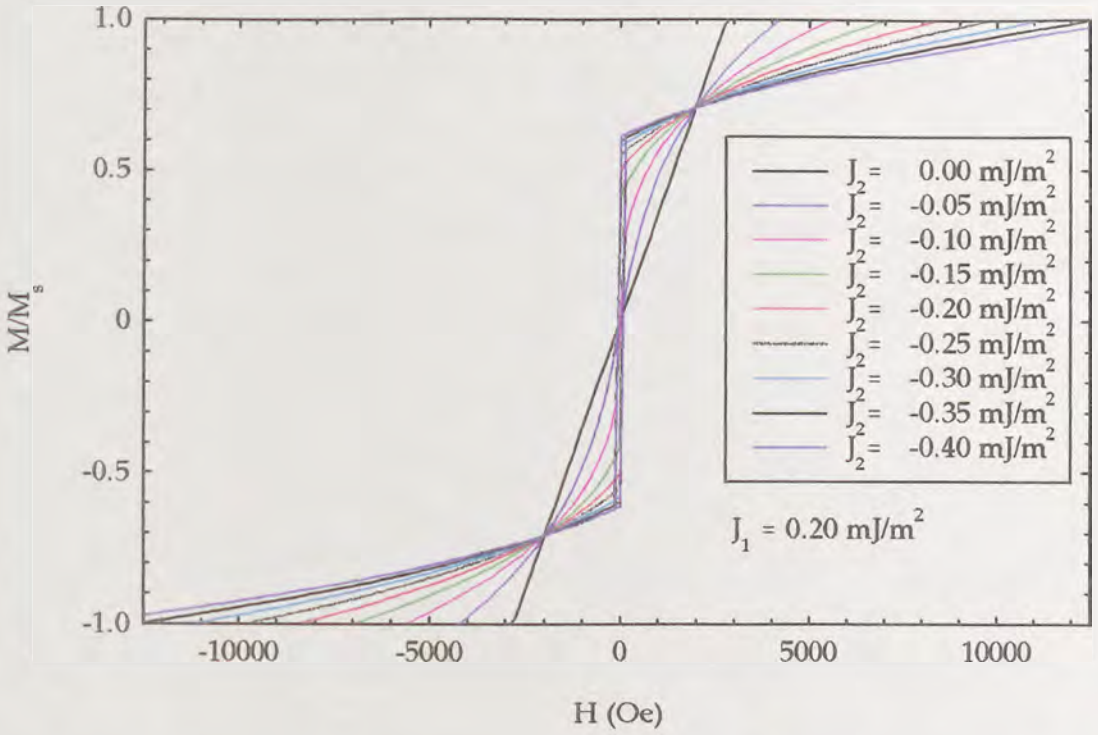

Figure 3.9 The results of numerically simulating the effect of varying the biquadratic coupling constant for a pair of 1nm thick Co layers also displaying bilinear coupling.

The behaviour of the biquadratic term is more complex, as it has two equivalent energy minima. Let us suppose that J_1=0 and consider a pair of coupled magnetic layers with J_2<0. In zero field the moments will lie at 90° to one another, and the net magnetisation will be $\sqrt{2}/2$ of the saturated value. In the absence of anisotropy the above symmetry considerations apply, and as the field is increased the moments will close towards the field direction until saturation is reached. We may modify the zero-field interlayer angle by now making J_1 slightly positive or negative, which in turn will affect the saturation field, now given by the above expression for pure bilinear coupling but replacing J_1 with the total effective coupling constant (J_1+2J_2). If $|J_1|>|J_2|$, then the bilinear term again dominates, and the remanent fraction is again zero (J_1<0) or unity (J_1>0). This behaviour is more easily understood by reference to the phase diagram given below, where these two states are represented by the regions AFM1 and FM respectively. The non-collinear

ordering for large negative J_2 is represented by region NC.

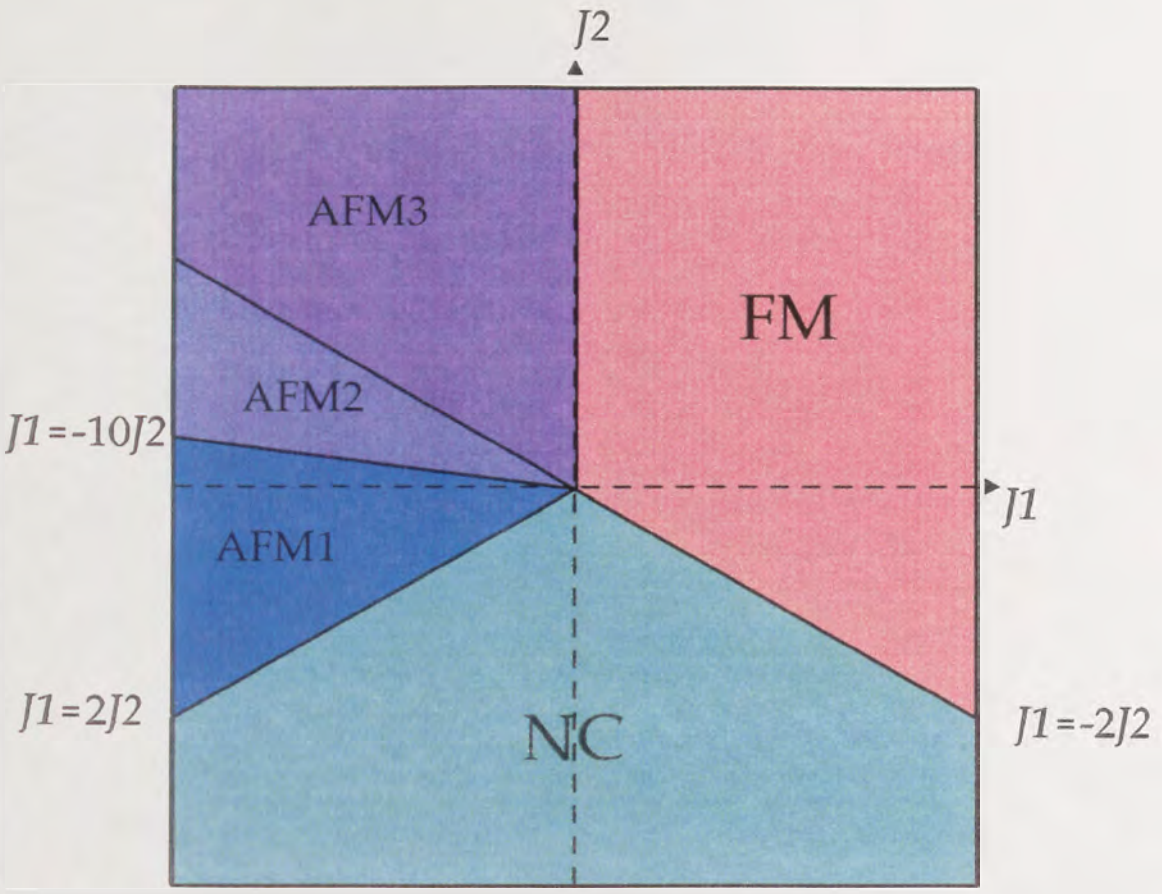

Figure 3.10 Phase diagram of magnetic multilayers in zero field exhibiting bilinear (*J1*) and biquadratic (*J2*) coupling. After Ustinov *et al* (ref 123).

For $J_2>0$, the ordering is collinear, but neither parallel or antiparallel orientations are favoured, except by the bilinear term. This means that there are two minima, and it is possible for hysteresis to result, as the system cannot reach the global minimum. The distinction between regions AFM2 and AFM3 in the phase diagram is whether the system gets back to the global minimum before or at zero field. However values of $J_2>0$ have never been observed experimentally.

A thorough and instructive explanation of the effects of these two forms of coupling was published recently by Ustinov *et al*[123], to whom the above phase diagram is due.

3.4 SUMMARY

The topic of indirect exchange coupling has been extensively studied in recent years, since the advent of UHV deposition techniques which allow careful and controlled preparation of high-quality samples. It now seems clear that the topology of the Fermi surface of the spacer is of importance in determining the period of the oscillations in coupling. However there are still a number of unexplained aspects of the problem.

The role of disorder is unclear - the RKKY formalism, the quantum well scheme, and calculations based on reflection coefficients all rely on crystalline order to derive the observed long oscillation periods. The effect of grain size in multilayers was first pointed out by Bobo *et al*[124]. They found the grain size estimated by X-ray analysis in their Fe-buffered samples was approaching 20Å yet still displayed reasonable GMR and oscillations. There are also a number of experimental results on coupling across alloy spacers[125,126,127,128], but theoretically disorder is difficult to treat. There have been some attempts to calculate the effects of substitutional disorder[129], but there is an overwhelming body of work on sputtered multilayers grown for their GMR properties, which suggests that the coupling phenomenon is universal, and not predicated on high quality epitaxy.

There have also been observations of oscillatory coupling across semiconducting[130] and amorphous-Si spacers[131], which pose severe theoretical problems. Bruno has attempted a treatment of *ordered* insulating spacers[132], and finds the correct temperature dependence, but does not find oscillations. This calculation relies on the properties of a complex Fermi surface, and a full description of this, as well as the unified theory described above was recently published in a long paper[133].

The mathematics of minimising the energy are typically not trivial. Stoner and Wohlfarth gave an analytic solution of the problem of a single domain with uniaxial anisotropy, and their approach was extended by Fujiwara and Parker to cover the case of $2N$ layers with identical uniaxial

anisotropy, with bilinear and biquadratic coupling[134].

In general it is easier to solve the problem numerically, which allows for more generality in the conditions which are to be solved for, with arbitrary anisotropies and couplings in a set of layers which need not be all like. This may be completed in not too long a period of time on even an i486-based PC, and in a matter of seconds on a fast RISC workstation. This allows the parameter space of the problem to be searched rapidly, and a large number of curves to be generated to be fit to the experimental data.

4. Giant Magnetoresistance and Oscillatory Exchange Coupling in Co/Cu Multilayers

4.1 Introduction.

In this chapter the initial results obtained on the Co/Cu samples first grown will be described. A few very early results will be presented showing how the Meissner trap was an essential aspect of producing good quality GMR samples. In order to characterise the system well, measurements of the coupling and GMR as a function of Co layer thickness, Cu layer thickness and number of bilayer repeats were carried out. Large giant magnetoresistances were obtained at the first and second coupling peaks, which were well defined.

4.2 Improving the vacuum

A large number of samples were grown once the sputtering system was brought back to a usable state, with a wide variety of sputtering rates, working gas pressures, substrates and thicknesses of layers. Very few exhibited any GMR, and for those few which did the magnitude was of only a few percent.

The later modification of adding the Meissner trap was crucial in achieving a large GMR. Samples grown at base pressures of more than ~5×10^{-7} Torr showed consistently poor GMR ratios. There is then a rapid rise until below ~1×10^{-7} Torr good results are achieved for the proper layer thicknesses. The Meissner trap lowers the pressure through just this range, once the additional gas load of the localised heating of the running magnetrons is taken into account.

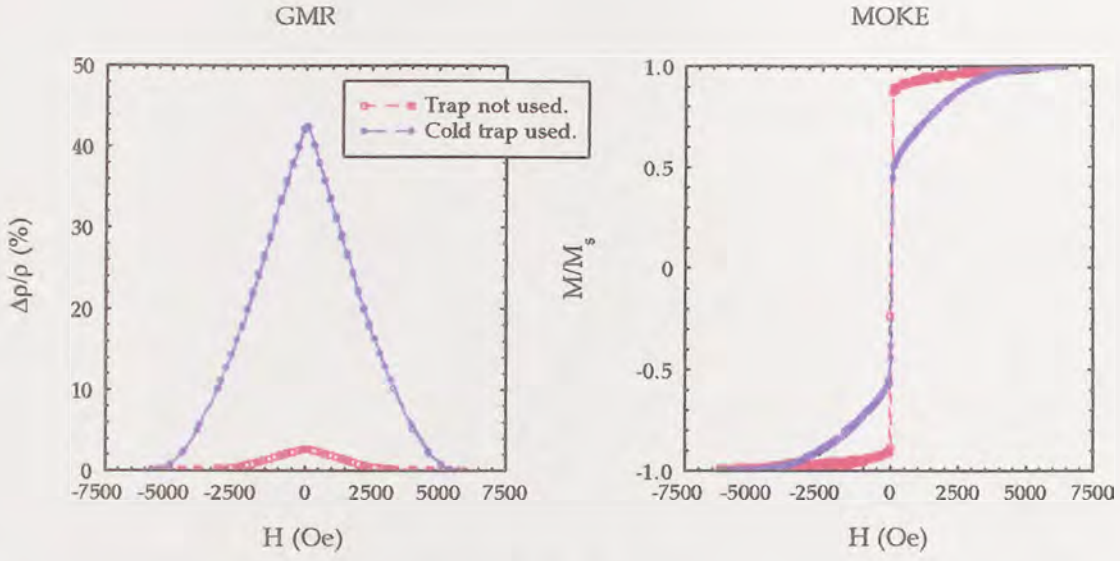

Figure 4.1 The effects of the use of the Meissner trap on the GMR and MOKE loops of two {Co(9Å)/Cu(9Å)}×25 multilayers grown under otherwise identical conditions.

In Fig 4.1 the difference the cold trap makes is illustrated by comparing the GMR and MOKE loops of a pair of typical Co/Cu multilayers grown under otherwise identical conditions. The GMR for a sample grown under poor vacuum conditions without the trap being used has a GMR ratio of only 4%, and the MOKE loop shows it to have a ferromagnetic character. A sample grown whilst the trap is filled with flowing liquid nitrogen has a GMR ratio of over 40%, has a much smaller remanence. It is apparent this sample exhibits marked antiferromagnetic interlayer coupling. It is interesting to note that it was not necessary to use any buffer layer to achieve this large GMR. The sample was grown directly onto the native oxide layer of the Si wafer. The relative magnitudes of the magnetoresistance are what would be expected from the relative remanent fractions measured by MOKE. The saturated resistivities of the two samples are too similar to explain the difference in $\Delta R/R$. The importance of a clean vacuum to large GMR is immediately evident. Experience over the growth of large numbers of multilayer samples shows that H_2O is particularly damaging, in accord with others [135].

Basic x-ray analysis of such a pair of samples at Leeds by the low and high angle techniques described in Chapter 2 revealed no obvious structural differences. The low angle Bragg peaks were distinct, and good quality Kiessig fringes were observed. At high angles no texture could be discerned. Further structural analyses were undertaken at other sites to attempt to determine the microstructural effect of the residual gases which were contaminating the poor sample.

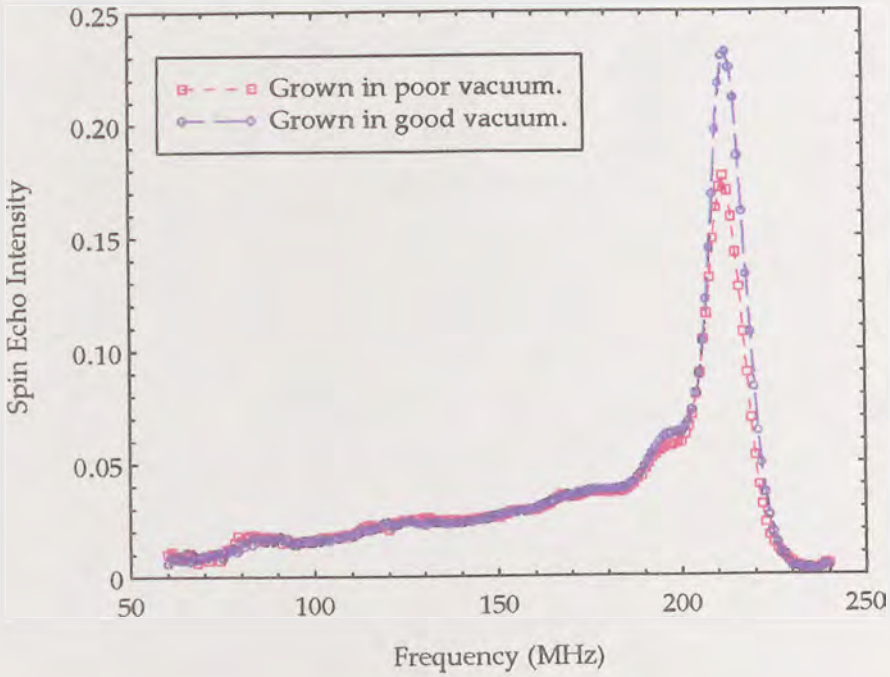

Figure 4.2 Nuclear magnetic resonance spectra of a pair of Co/Cu multilayers grown with and without the use of the Meissner trap.

Nuclear magnetic resonance experiments were performed at ICPMS-GEMME in Strasbourg by C Mény and M Malinowska. Zero field NMR was performed at 1.5K with a broadband automated spectrometer in order to get information on the bulk and interface short range structure. The NMR spectra for the two samples are shown in Fig 4.2. There are no differences in the spectra indicating that the interfaces have the same short range morphology in both samples. The main peaks indicate that the bulk Co is fcc-like, whilst the extended low frequency part of the spectra indicates that both samples have intermixed interfaces. First analyses shows that the

amount of intermixing at the interfaces is about 1.5 full Co atomic planes suggesting that the interfaces are of quite good quality. (A perfectly flat interface would contain 1 atomic plane.) However it was not possible to reproduce the shape of the NMR spectra with a step interface model, nor with a simple diffuse interface model[136]. To simulate the NMR spectra it was assumed that the Co layers are composed of clustered Co atoms separated by a random CoCu alloy containing about 60% of Co. The height of the clusters is about 6 atomic planes and the surface area occupied by clustered Co atoms follows this sequence: 12%, 83%, 92%, 92%, 83%, 12%. Such a model has been previously used[137]. This particular structure of the Co layers (in particular the reduced magnetisation in the alloyed part) may play an important role in the magnetotransport behaviour of those samples.

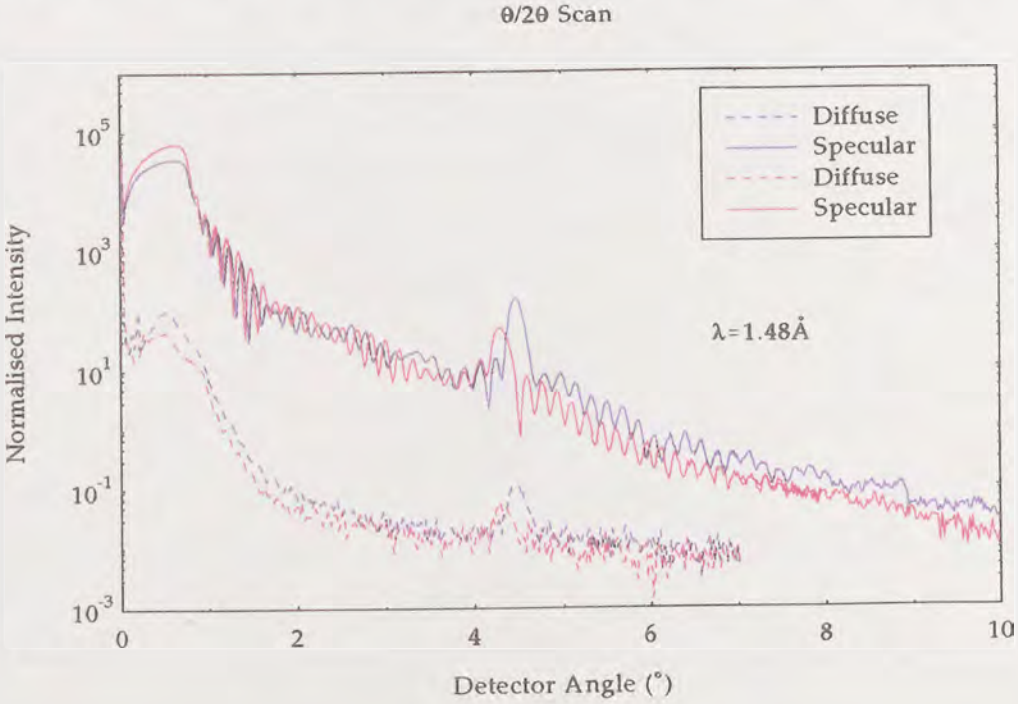

Figure 4.3 Low angle X-ray scans performed at the Daresbury synchrotron source. The blue curves are those from a high-GMR good vacuum sample, the red curves those of a poor vacuum low-GMR sample.

Further detailed analysis of such a pair of samples was undertaken using synchrotron X-ray diffraction. No measurable differences were detected. The small difference in Bragg peak positions represents a small

difference in bilayer period, but is not significant enough to explain the drastic drop in GMR. The second Bragg peak is missing as the Co and Cu layers are of almost equal thickness. Both low angle and transverse scans showed that the rms conformal roughness in both cases was ~1.0Å, with a total rms roughness of ~1.4Å. This represents an unusually high degree of correlation for sputtered samples. This is reflected in the very low amounts of diffuse scatter observed.

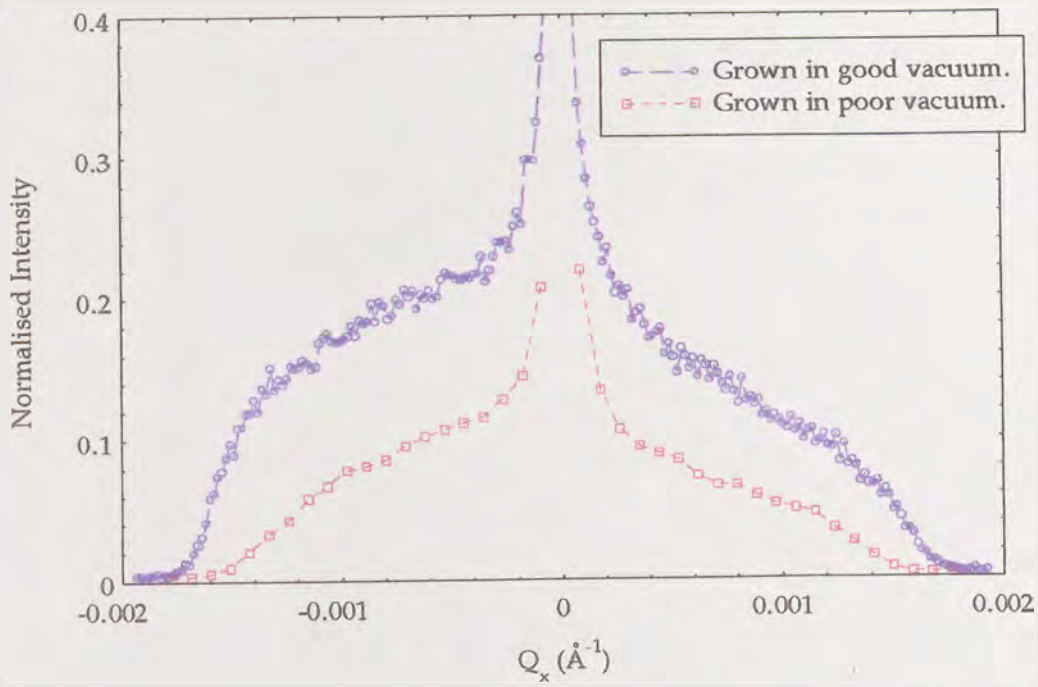

Figure 4.4 X-ray rocking curves (transverse scans) through the first superlattice Bragg peak shown in the θ/2θ scans.

In short it was found that the layers were very smooth, and what little roughness was present is remarkably conformal. No texture was detected. The Co layers are in the form of large Co clusters, separated by a Co rich alloy. However despite there being no obvious structural differences the magnetic and magnetotransport properties were markedly affected by the presence or absence of residual gases during growth.

4.3 COUPLING OSCILLATIONS

4.3.1 Characterising the system

Once the system was producing samples that exhibited a respectable GMR, the work moved on to a fuller characterisation of the Co/Cu multilayers being grown. This is a system that has been investigated by a large number of groups around the world, and so represented a good benchmark by which to judge the deposition machine. Two series of samples were grown in which the thickness of both the copper spacer and cobalt layers were varied, also the effect of varying the number of bilayer repeats was investigated.

4.3.2 Texture and microstructure

There have been a wide variety of studies on sputtered Co/Cu since the discovery of the coupling oscillations and very large giant magnetoresistance effect in this system[138,139]. A number of workers have sought to identify those conditions under which the GMR is large, and in particular there has been much work attempting to associate a particular texture or crystal orientation with large GMR ratios. Although the earliest discoveries of high GMR in this system by Parkin were in (111) textured samples, a number of workers then suggested that the absence of (111) texture was a pre-requisite to a large GMR effect. Pollard, Grundy and co-workers found in common with a number of others that an Fe buffer layer of between ~50 and 100Å was necessary to achieve a large GMR, and that samples grown on such a buffer exhibited reduced (111) texture[140]. They later grew Co/Cu on Si(111) wafers which had been progressively etched to expose bare the Si beneath the surface oxide layer. They found that the GMR ratio dropped from it's high initial value as the etching energy was increased, and this correlated with the a rise in (111) texture in the metal film[141]. Suzuki et al found that the use of an Fe buffer layer reduced (111) texture, and found that the GMR ratio rose in line with the quantity of (220) texture[142]. However Honda *et al*

made a positive correlation between high GMR and the presence of (200) texture[143].

A full structural characterisation of a number of samples was carried out at Daresbury by T Hase, B Tanner and C Lehmann from the University of Durham, building on the initial X-ray work performed here at Leeds. The results of this extended structural characterisation will be reported here, since the microstructure determined from these X-ray scans has an important bearing on the discussion of the magnetic properties of the samples.

Low-angle X-ray reflectivity and diffuse scattering experiments were performed on station 2.3 at the Daresbury Synchrotron Radiation Source[144] with a slit-limited instrumental resolution of 40 arc seconds. High angle diffraction scans were also performed at the SRS using a Soller slit detector collimator and on a conventional Bragg-Brentano powder diffractometer using CuKα radiation and a curved crystal graphite monochromator.

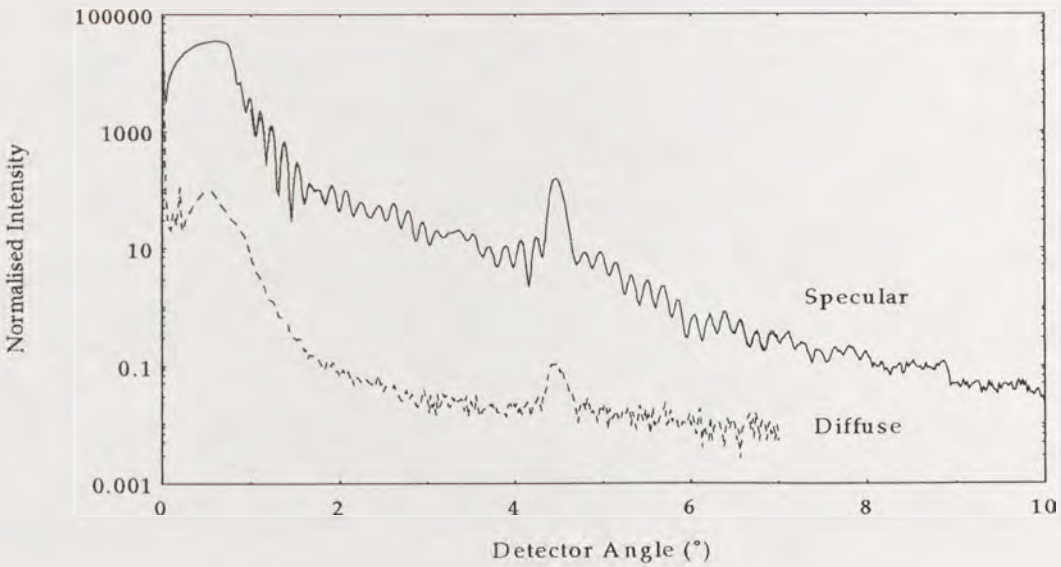

Figure 4.5 Low angle reflectivity data from the SRS for the Co/Cu multilayer taken with an X-ray wavelength of 1.48Å. The modulation is caused by CuO as the layers are uncapped. There is a single multilayer Bragg peak visible at 4.5°.

Fig 4.5 shows the low-angle X-ray results for both the specular and diffuse components of the scatter for a sample of the form

$\{Co(10Å)/Cu(10Å)\}_{20}$. The specular results show very good Kiessig fringes extending up to about 8 degrees and a single multilayer Bragg peak. This low rate of fall of intensity with scattering vector indicates a very low surface and interface roughness. Longitudinal (offset θ-2θ) diffuse scans were measured using an offset of -0.1°. These results show very low diffuse scatter consistent with a very small roughness. The presence of a clear Bragg peak in the diffuse scatter indicates that much of the roughness is correlated throughout the multilayer stack. Born wave analysis of transverse scans (rocking curves) give a correlated roughness of 1.0 ± 0.5Å. The second order multilayer Bragg peak is again absent as the Co and Cu thicknesses are very close. These results are very similar to those presented above on early samples.

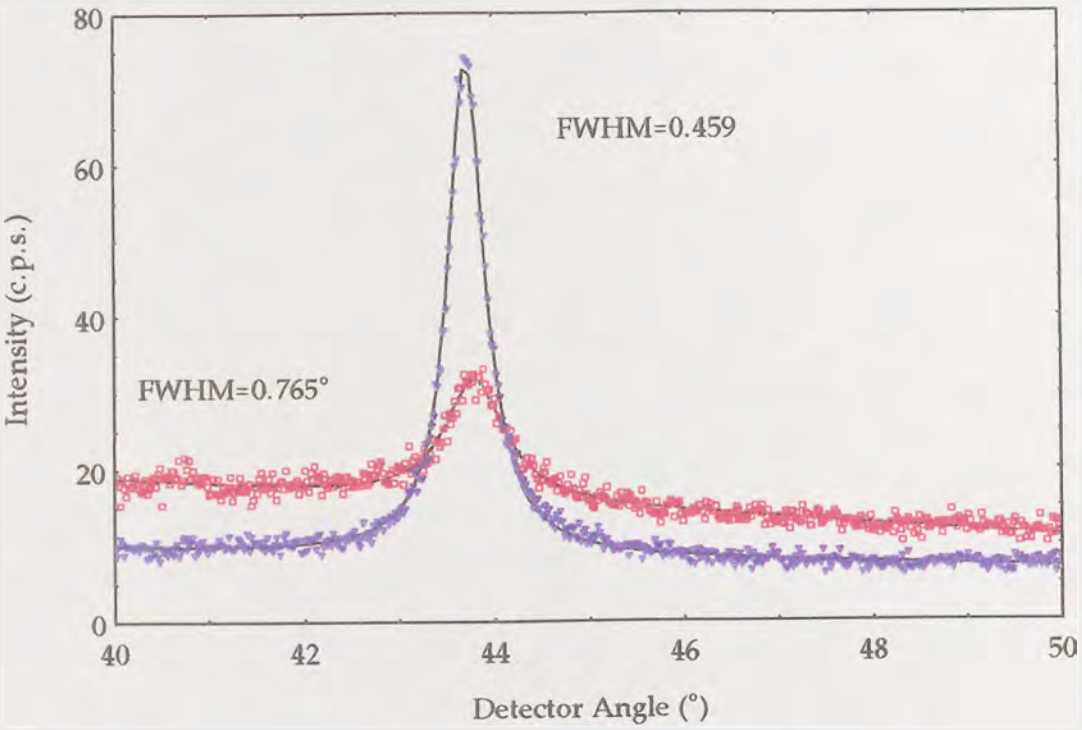

Figure 4.6 High angle x-ray diffraction data for Co/Cu multilayers performed with Cu K_α radiation at the Dept of Chemistry, University of Durham. Blue triangles: A sample grown on Si(001) with 50 bilayer repeats. The FWHM of the (111) Cu/Co peak is 0.459°, which gives a minimum grain size of 210Å. (High resolution data obtained at the SRS raises this limit to 250Å). Red squares: A sample grown on Si (111) with 25 bilayer repeats.

Fig 4.6 shows the high angle (θ-2θ) diffraction data for the same sample. The (111) Cu/Co Bragg peak is small but well defined. The compromise peak was fitted to a Lorentzian giving a FWHM of 0.765° and a lattice parameter of 3.5804Å which is close to the expected value (3.579Å) for a 50:50 Cu/Co multilayer. The inverse of the FWHM in reciprocal space reveals the grain size to be approximately 140Å. The laboratory θ-2θ scan of another sample is also shown. This sample was grown on an (001) oriented Si substrate and has a smaller FWHM, giving a minimum grain size of 210Å.

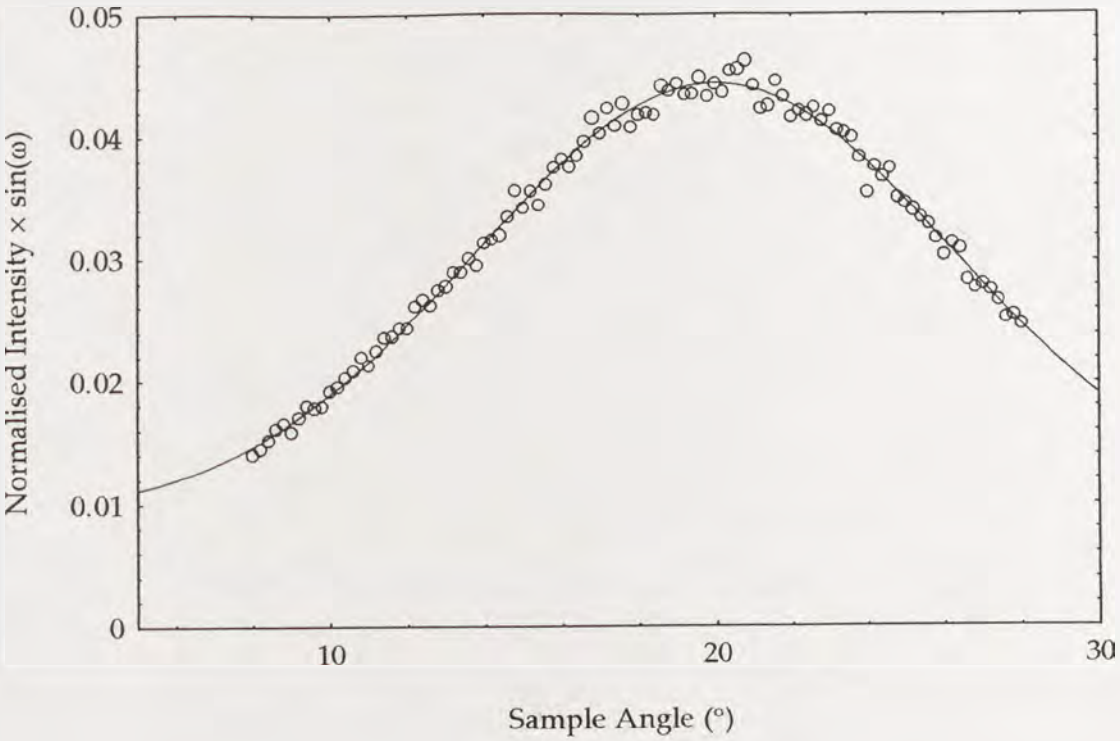

Figure 4.7 Rocking curve of a Co/Cu multilayer through the high angle Bragg peak. The position of the detector is held constant at the 2θ value for the Bragg peak, whilst the sample is rotated through the specular reflection position. The FWHM of this curve is ~16°.

Rocking curves of similar samples taken at the SRS show that the spread of (111) oriented grains around the surface normal is of the order of 16° FWHM (Fig 4.7). This explains the low intensity in the laboratory data, as at any one time only a very small fraction of the grains are diffracting the X-ray beam. This rocking curve width is extraordinarily large. This is the reason for initially detecting no texture, as only a few grains are diffracting the beam at any one time, due to the wide spread of orientations.

These results suggest an unusual microstructure. The width of the rocking curve shows that the distribution of ⟨111⟩ directions extends to about 8° in every direction around the film normal. The grains are quite large, ~200Å, as measured by the width of the high angle Bragg peaks. One might speculate that the Co/Cu interfaces might follow the rapidly tilting atomic planes as they pass from grain to grain, but this does not appear to be the

case from the excellent low angle data, which suggests exceptional layering quality. The rms roughness of the interfaces is too low for them to be so far removed from ideal planes, and it seems that the interfaces must pass through the grains at small angles to the planes of atoms. This means that the interfaces take on the character of vicinal surfaces with a miscut equal to the grain tilting angle, with a distribution half-width of 8°. This structure is drawn schematically in Fig 4.8.

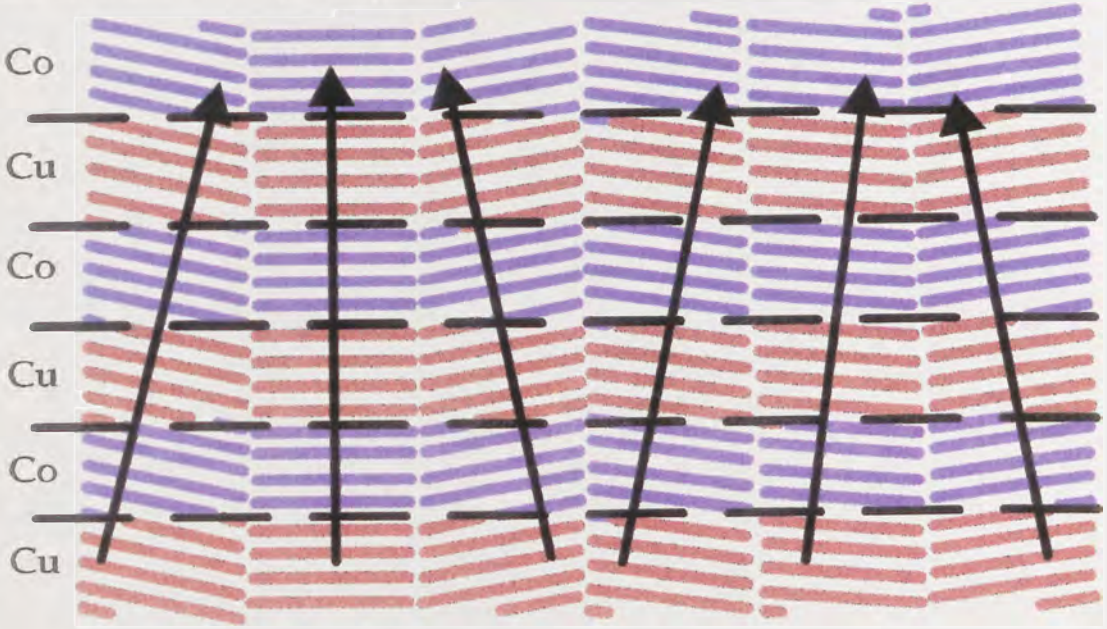

Figure 4.8 Schematic representation of the multilayer microstructure. The individual grains are of the order of 200Å in diameter, and the angular distribution of (111) directions is ~16° wide. The layer interfaces are close to ideal planes, passing through the grains at small angles the atomic planes.

One might suppose that the interfaces tilt a little toward the {111} planes inside each grain, as this would correspond to correlated roughness, but the rms amplitude of this roughness would still have to be of the order of only 1Å.

4.3.3 Spacer oscillations

One property of Co/Cu multilayer systems is the strong oscillations of the coupling with respect to the Cu spacer thickness due to the good band

matching between the Cu and minority-Co d-bands. This coupling oscillation results in a series of peaks in the GMR as the Cu spacer layer is made thicker. Parkin's original results showed four antiferromagnetic maxima in the GMR curve, although the fourth peak was very weak.

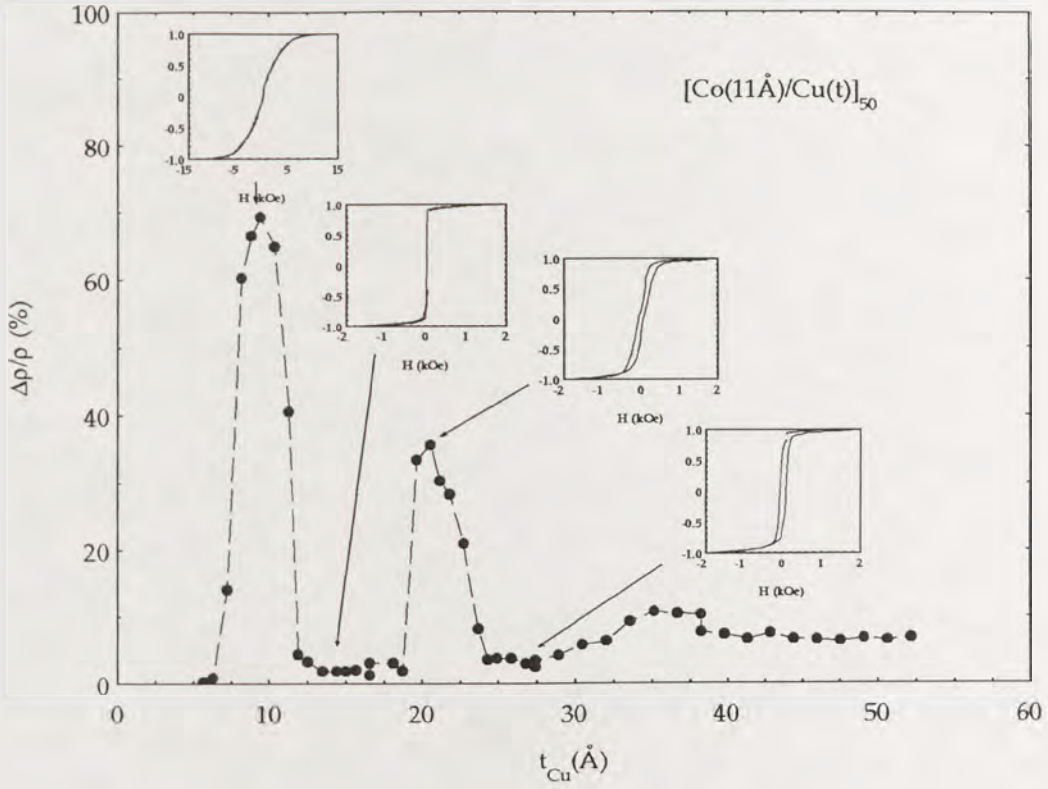

Figure 4.9 The GMR as a function of the thickness of the Cu spacer. Each inset shows a MOKE image corresponding to the indicated sample. Note that the field scale in the first inset is different to the remaining three. There are clear oscillations with a period of about 10Å and clear regions of AF and F coupling.

Figure 4.9 shows the room temperature magnetoresistance for multilayers with a constant thickness of Co(11Å) plotted as a function of the Cu spacer thickness. The insets show longitudinal MOKE curves for various samples measured at the same temperature. The GMR data show that there are clearly two peaks and a marked rise towards a third, corresponding to regions of antiferromagnetic (AF) coupling with regions of ferromagnetic (F) coupling in between. The period of this oscillation closely matches that

reported for other sputtered samples of Co/Cu. The magnitude of the GMR is high as any in the literature, rising to 130% at 4.2K for the first maximum and such a sample has almost zero remanence.

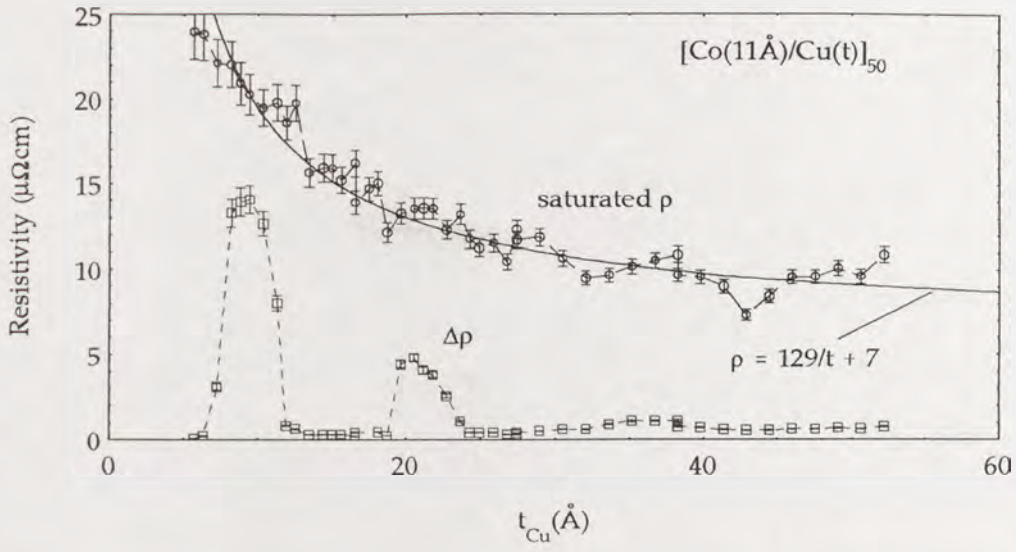

Figure 4.10 The magnetically saturated resistivity and change in the resistivity as a function of the Cu spacer layer thickness. The solid line is a fit given by $\rho = 129/t_{Cu} + 7$. (Units as on the graph).

The resistivity of the layers as a function of the Cu thickness is shown in Fig 4.10. The magnetically saturated data follows a Fuchs-Sondheimer-type behaviour with an extrapolated value of the Cu resistivity of about 7μΩcm. The oscillatory component is seen to be entirely in $\Delta\rho$.

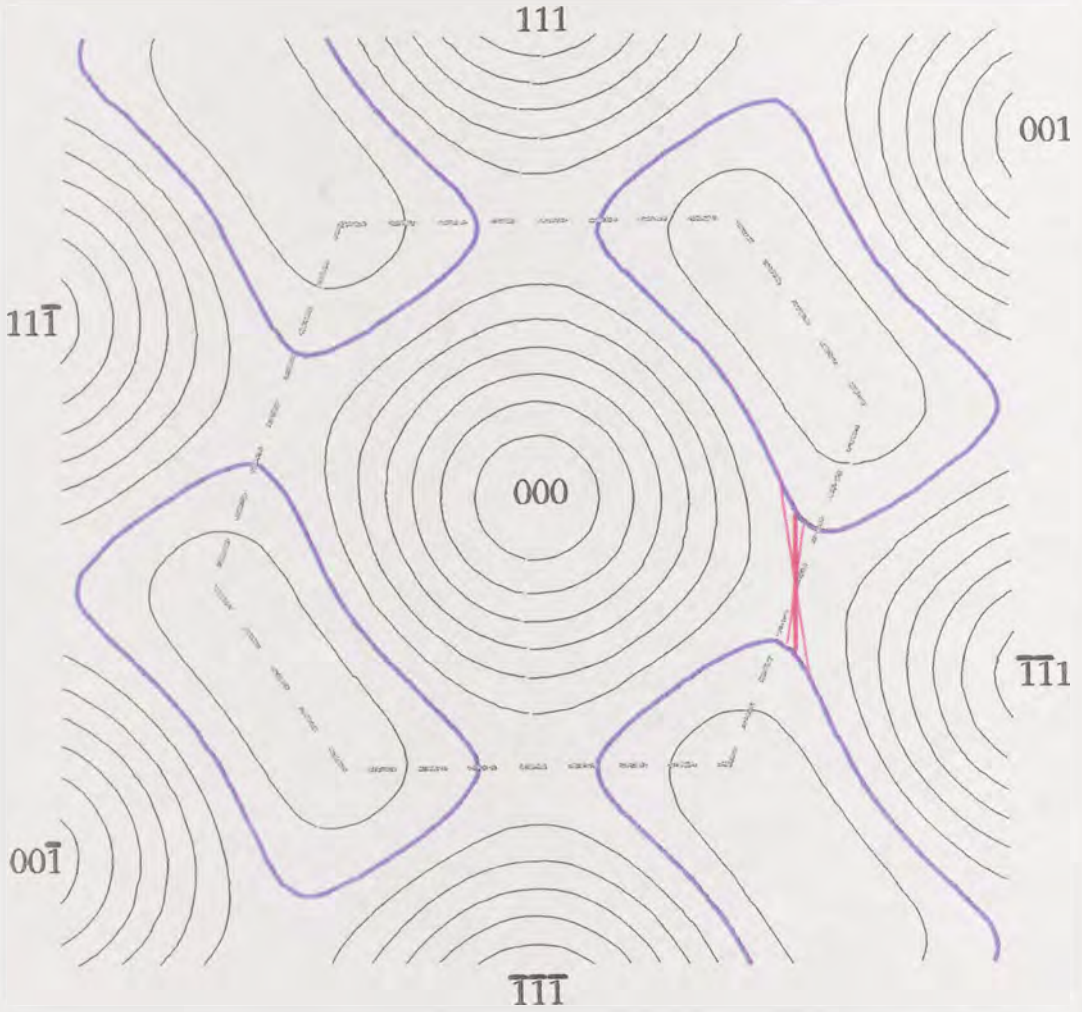

Figure 4.11 Constant energy contours in the ($1\bar{1}0$) plane, including the Fermi surface, marked in blue. The dashed line marks the first Brillouin zone boundary. The [111] direction spanning vector is marked by the vertical red line, and the paler vectors represent rocking the Fermi surface by 8° in either direction. The change in length of the spanning vector is immediately apparent. Energy contours taken from Edwards *et al.*[145].

Some discussion of these oscillations is now in order - the period of the coupling is measured to be a little over 10Å, which lies comfortably within the region spanned by various other published results. We must of course pay attention to the orientation of the sample, and compare our samples to those most alike - in this case (111) oriented multilayers. However only a small fraction of the grains in this case are truly (111), with the remainder taking up some close orientation. We recall from Chapter 3 that the period is

determined by a spacer Fermi surface spanning vector which lies parallel to the layer normal. For (111) Cu this presents an additional complication, as the Fermi surface necks lie in the ⟨111⟩ directions. This means we cannot simply draw our vector across the Fermi surface in the usual fashion, but must draw it at an angle across an adjacent neck.

We must rotate the Fermi surface by up to 8° in order to assess the effects of the misaligned grains. If the layers were (001) oriented (for example), then this would have little effect, as in this region the Fermi surface is near spherical, and the extremal vector length would hardly vary at all. When this operation is performed in the ⟨111⟩ direction though then large changes in the spanning vector length can occur, as the Fermi surface is highly distorted from a free-electron-like spherical form in these neck regions. This is illustrated in Fig 4.11. The (111) plane has threefold symmetry, and the spanning vector will lengthen or shorten, depending on whether the tilt is towards either ⟨110⟩ or ⟨100⟩ respectively.

How should this be interpreted? Each individual grain now contains Co layers coupled with a different period, depending on that particular grain's orientation. As the Co layers are expected to be continuous across a number of grains due to the low roughness we may expect that some averaging of the distribution of periods may take place in order to determine the oscillation which is displayed macroscopically in Fig 4.9. It is found that due to the particular shape of the Fermi surface, that the long period tail of the distribution is somewhat dominant, and will tend to shift the average to a slightly longer period than that expected for a purely (111) sample. This is in accordance with the data.

4.3.4 Magnetic layer oscillations

As discussed in Chapter 3 there have been a number of predictions that the magnitude of the interlayer exchange coupling should oscillate as a function of the thickness of the ferromagnetic layers. Experimental investigations have focused on the two most widely studied magnetic

multilayer systems: Co/Cu and Fe/Cr but the results are inconsistent. For each system, some observe the predicted oscillations, whilst others do not. For the Co/Cu system, Qiu et al.[146] did not find any such oscillations, whereas by contrast, Bloemen et al.[147] reported oscillations with a period of 6-7 Å of Co. A similar situation exists for the Fe/Cr system. Okuno and Inomata[148] reported "oscillatory exchange coupling as a function of the Fe layer thickness". However, in the subsequent studies of Schad *et al.*[149] for the Fe/Cr system it was found that that "None of the transport properties shows any indication of oscillatory behaviour."

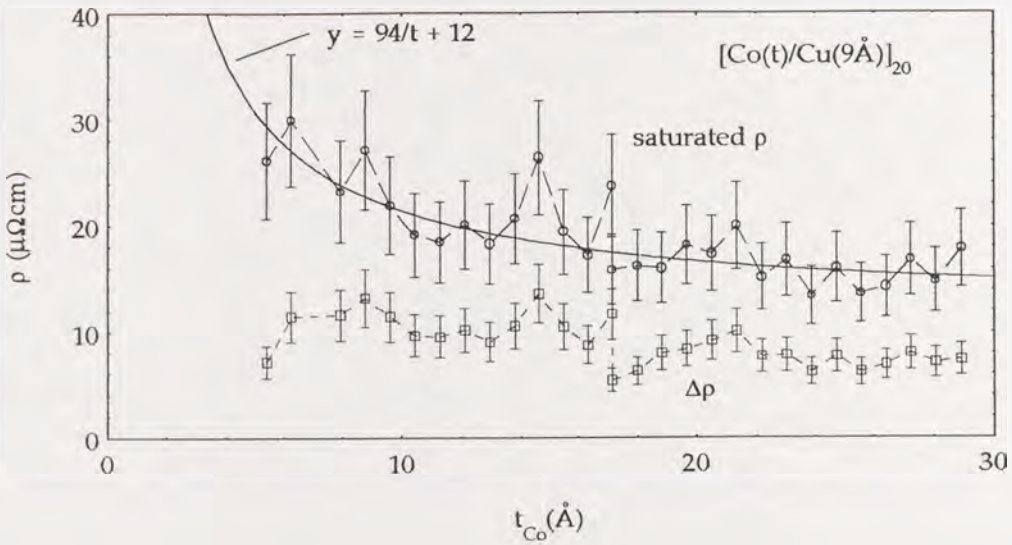

Figure 4.12 The magnetically saturated resistivity and change in the resistivity as a function of the Co thickness. The solid line is a fit given by $\rho = 94/t_{Co} + 12$. (Units as on the graph).

First of all examining these transport properties, Figure 4.12 shows the thickness dependence of the saturated resistivity as a function of the Co thickness in a series of sputtered Co/Cu samples. Extrapolating this data gives a thick-film resistivity value for Co of 12μΩcm. Also plotted in this figure is the variation of $\Delta\rho = \rho(0) - \rho(B_s)$ where the main source of uncertainty is the width of each sample, as these samples were not prepared through contact masks. Within the limits of our experiment there are no oscillations as a function of the Co thickness.

Of course the magnitude of the GMR does not depend on the magnitude of the coupling, but the strength of the interlayer exchange coupling can be determined by measuring the magnetic field that saturates the magnetoresistance. We recall from Chapter 3 that in the absence of anisotropy, that the expression for the saturation field of a multilayer is,

$$H_s = \frac{4J_1}{\mu_0 M t_{Co}}.$$

We are justified in neglecting the anisotropy, as magnetometry measurements of the samples showed no sign of anisotropy for any thickness of the magnetic layer. Moreover, the near (111) texture revealed by the high-angle x-ray scans indicates that there is little to support the existence of in-plane anisotropy[150], despite the presence of the forming field during growth. Hence, the saturation field Hs directly gives the strength of the exchange coupling energy J_1. For a constant value of J_1 (independent of t_{Co}), a plot of $1/H_s$ vs t_{Co} will yield a straight line whose slope equals $\mu_0 M/4J_1$. However, if the magnitude of J_1 oscillates with t_{Co}, such a plot will exhibit oscillations in $1/H_s$ around the straight line.

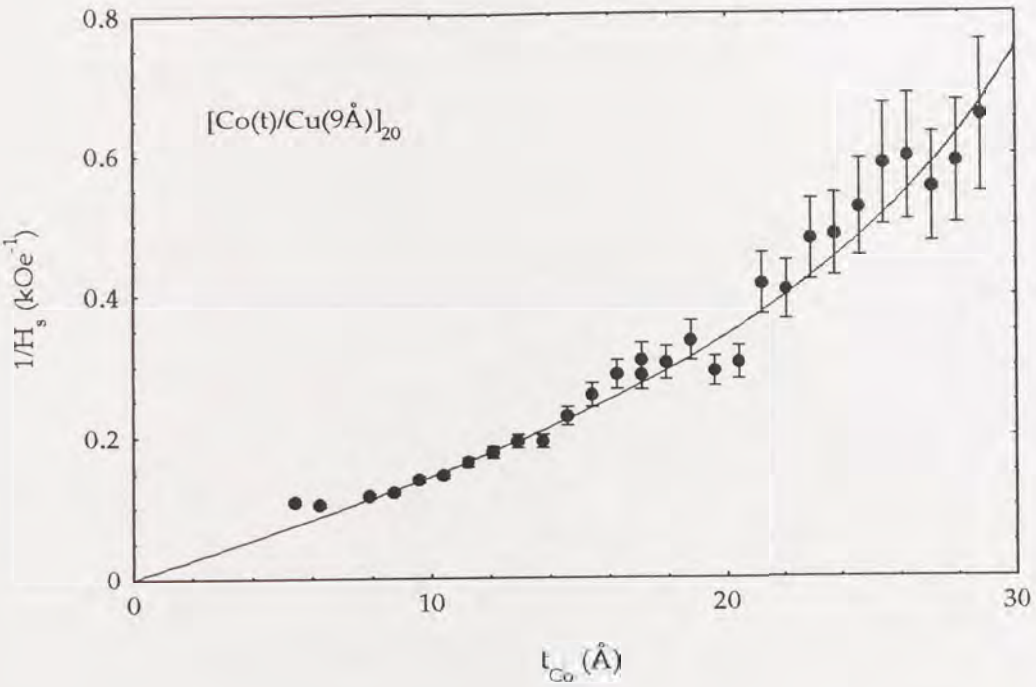

Figure 4.13 Inverse saturation field H_s as a function of the thickness of the Co layers for Co/Cu multilayers. The red curve is the best fit to the orange-peel coupling model, as described in the text.

The experimental data is shown in Fig 4.13. For values of t_{Co} between 8 and 20Å the data fits well to a straight line. For high and very small Co thicknesses the data points lie above the position of such a line, indicating weaker than expected coupling. At low thicknesses this is due to the layers becoming so thin that they are discontinuous, indicated by the magnitude of the GMR dropping rapidly towards zero at these thicknesses. The reason for the weaker coupling at large thicknesses is more complex.

Many years ago, Néel[151] discussed what has become known as orange-peel coupling relating to the free poles on the surfaces of magnetic films which are not perfectly flat. This topological coupling has since been studied by a number of workers[152,153]. The model orange-peel structure is a two-dimensional sinusoidal wave, characterised by roughness amplitude σ and wavelength ξ. Atomic force microscopy measurements confirm the presence of wavy surface roughness for the thicker magnetic layers and the X-ray analysis of the samples has shown us that much of this roughness is

correlated throughout the multilayer stack.

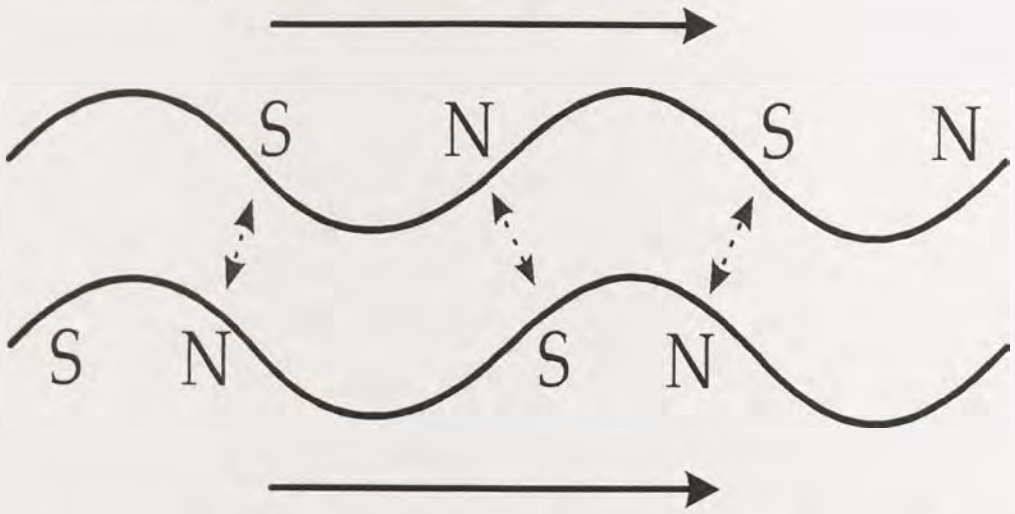

Figure 4.14 Magnetostatic interactions between the free poles formed on the surfaces of wavy magnetic layers interact across the spacer layer, causing ferromagnetic coupling. This is referred to as orange-peel or topological coupling.

The effect of this wavy structure is to generate magnetic poles on neighbouring magnetic layers. When the waviness is in-phase, i.e. the roughness is conformal, these poles then couple the layers ferromagnetically, thus reducing the effective strength of the antiferromagnetic exchange coupling.

This coupling energy is proportional to the square of the roughness amplitude, which for the present analysis, we assume to increase linearly with thickness. Thus we write the effective coupling

$$J_{eff} = J_1 - J_{op}t^2$$

where J_1 is the true antiferromagnetic exchange coupling energy and J_{op} is the correction term due to the orange-peel effect. Inserting this into the expression for Hs gives the final expression to be compared with the data,

$$\frac{1}{H_s} = \frac{\mu_0 Mt}{4(J_1 - J_{op}t^2)}.$$

The values of t and H_s are measured, M is given by its handbook value (1.4 MA/m for Co at room temperature), and the values of J_1 and J_{op} are

determined by fitting to the data. The particular question of interest here is whether one gets a good fit using a constant value of J_1. The results of the fit are also given in Fig. 4.13, and the agreement is good. In particular, there is no sign of any oscillations. The error bars increase for samples having thicker magnetic layers because the correspondingly smaller values of H_s imply a larger experimental uncertainty. But for samples with the thinner magnetic layers, the error bars are very small, and the results are therefore quite reliable. The accuracy with which we can define relative layer thicknesses in a series of samples is determined by X-rays to be 0.5Å. Therefore if there were oscillations in our samples as a function of Co thickness, we should have seen them.

One can obtain the value of J_1 from the fit to the data shown in Fig. 4.13 initial slope, $J_1 \approx 0.25$ mJ/m^2 which is in agreement with the values previously reported for Co/Cu multilayers by Mosca et al. [154](≈ 0.3 mJ/m^2) and by Parkin et al. [155](≈ 0.15 mJ/m^2). The derived value of J_{op} implies the following values for the wavelength ξ and the roughness amplitude σ of the orange-peel wave: $\xi \approx 140$ Å, $\sigma \approx 12\%$ of bilayer thickness. These values are consistent with the grain size deduced from both the X-ray scans and the atomic force microscope imaging of the top surfaces of our samples.

4.3.5 Total film thickness

There are also insights to be gained from varying the thickness of the entire sample by depositing different numbers of bilayers[156]. The minimum here is two, in order that there be a pair of magnetic layers to interact. The GMR was found to rise steeply up to around 15 bilayers where there is a knee in the curve, above which the slope is much more shallow. A sample with only 2 bilayers has a room temp transverse MR of only 0.1%, increasing to 71% for a sample with 100 bilayer repeats.

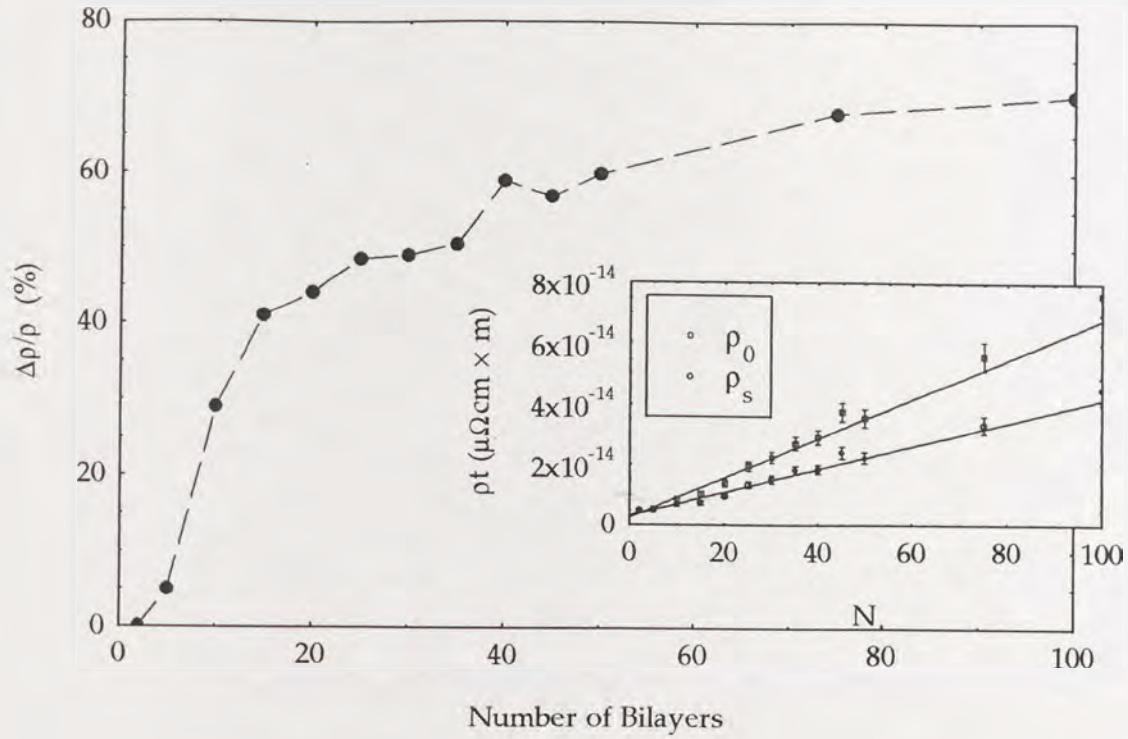

Figure 4.15 Giant magnetoresistance as a function of the number of bilayer repeats for {Co(10Å)/Cu(10Å)}×N at room temperature. Inset is the Fuchs-Sondheimer straight line fit to the size-dependent resistivity data also at 300K.

The Fuchs-Sondheimer fits to the data indicate that the resistivity of a multilayer with an infinite number of repeats would be 21.1μΩcm in the saturated state, and 37.3μΩcm at zero field - a GMR ratio of 77%. The associated mean free paths determined from the fit are ℓ_{sat}=311Å and ℓ_0=52Å. Like Plaskett and McGuire[157], we found that the GMR increases rapidly for total thicknesses below, ℓ_0 and then has a more gentle upward drift. From the simple resistor network model of GMR these values imply $\ell_\uparrow$=594 Å whilst $\ell_\downarrow$=27 Å. Despite $\ell_\uparrow$ being more than a factor of 20 greater than $\ell_\downarrow$ the GMR ratio is still less than 100%.

$\ell_\uparrow(\ell_\downarrow)$ is the mean free path for spin ↑ (↓) electrons.

4.4 CONCLUSIONS

The quality of the samples is remarkably good - the best GMR observed at room temperature in a sample grown in this sputtering system was 75%,

with values of 65-70% being achieved routinely. Three complete periods of the Cu spacer coupling oscillation were observed, with the remanence of a sample grown at the first antiferromagnetic peak being very close to zero. These results compare favourably with the best published results on CoCu multilayers.

The microstructure of the samples as determined by X-ray analysis is unusual - there is a weak (111) texture, but the rocking curve width is very large, a FWHM of 16°. From this we may determine that the grains are ~200Å in diameter, and have their {111} directions distributed within ~8° of the film normal. However the layering structure is of very high quality, with a total rms roughness of ~1.5Å, with an rms correlated roughness of ~1.0Å. This represents ultra-smooth layers, and an unusually high degree of correlation from on layer to the next. We deduce from these two pieces of information that the likely form for the interfaces within a grain is similar to that of a vicinal surface, with the interfaces making a small angle with the atomic planes.

Thus it has been shown that it is not necessary to have a well defined crystallographic texture to achieve long-period oscillations in the coupling, as many theoretical models require. Instead it is important that the layer thicknesses are well defined, and that the layers are smooth.

However despite the strong oscillations as a function of Cu thickness, no oscillation is observed for varying the Co layer thickness. The question arises as to whether or not there should be oscillations in these samples. Consulting Fig 4 in the paper by Barnas[158], we see that for a band splitting of 2eV the expected period is about 3Å, but in fact these oscillations are severely damped so that only 2 large peaks are visible below 10Å and virtually none above. We conclude that we should not expect to see oscillations as a function of the Co thickness in these samples.

5. Biquadratic Coupling & Residual Gases

5.1 Introduction

5.1.1 Background gases

In the previous chapter we briefly discussed the dire consequences of not using the liquid nitrogen trap on the magnetic and transport properties of multilayer Co/Cu samples. To recap, it was found that using the trap improved the base pressure by about an order of magnitude, principally by condensing out water vapour. Under these superior growth conditions, the GMR ratio of a typical Co/Cu multilayer increased from <5% to >50% at the first AF-coupling peak. Examining the magnetic properties by means of MOKE, it was found that the remanent fraction had dropped sharply from >90% for the poor low GMR samples to as low as <5% in the best cases with the use of the trap.

In an attempt to determine what the underlying morphological causes of these large changes might be, the samples were subjected to a detailed structural analysis by NMR and X-ray diffraction. The results were presented in the previous chapter, but for the moment it is necessary to recall only that no microstructural differences were found in the samples by either technique. The exact causes of the reduction of GMR by residual gases remain unknown.

Beyond the obvious assertion that a cleaner vacuum produces better samples the literature on the effects of background gases on GMR structures is not abundant. Yoshizaki and Kingetsu measured the GMR and crystallographic texture of Co/Cu multilayers grown in a baked and unbaked chamber[159]. They observed that the GMR of samples grown under UHV (baked) conditions had a larger GMR due to both a reduced saturated

resistivity due to less oxidisation of the samples, and also better antiferromagnetic coupling.

Kagawa et al also made a study of oxygen incorporation in sputtered Co/Cu multilayers[160]. They found that there was a sharp drop in GMR above a base pressure of about 10^{-6} Torr, not too much higher than in the present work. This was due to O_2 absorption. They also found that an Fe buffer layer absorbed O_2 and supposed that the GMR was improved by this mechanism. In the Leeds sputtering system we have not found that Fe buffers improve the GMR at any base pressure; in fact the converse is true. One might suppose that if this were to be the only purpose served by a buffer that a Ti layer would serve best. In general however studies attempting the use of other buffers have not met with success.

Both of these studies found that the largest amount of oxygen was incorporated into the earliest parts of the structure close to the substrate - the offered explanation being that a fresh coating of metal on the chamber walls would getter residual gases during later stages of the deposition. This is contrary to findings in the present study, as one might suppose that in growing a long series of samples that the later samples would incorporate less gas - however samples seem to remain consistent throughout the length of a run.

5.1.2 A selective probe

As structural analysis techniques had failed to yield any information on the origin of the large changes in GMR caused by the residual gases, a selective probing technique was adopted to attempt to discover which parts of the sample were most susceptible to damage by these gases. Whilst growing in a good vacuum with the cold trap operating the residual gases are at low partial pressures, and good quality clean samples can be prepared. If the growth is paused at a specific point in the multilayer stack, and the substrate moved away from the deposition source for a period of time then gas can be allowed to condense onto the surface of the growing film. When

growth is resumed the film will incorporate this gas much as if this specific region of film had been grown in a much poorer vacuum.

This technique allows a specific part of the sample to be *'gas-damaged'*, and we may investigate the effects of the background gas atoms wherever we choose in the stack. We may also choose to perform this action in every period of a multilayer structure, to determine the effects of gas atoms on e.g. the spacer layers, or the interfaces.

5.2 PROBING THE MULTILAYER STRUCTURE

We chose to absorb residual gases at various different parts of the multilayer structure - into the centre of every Cu layer, every Co layer, in every interface, and every other interface. A sample without any pauses in growth was also grown as a control sample. Every break was of 10s away from the source. This corresponds to ~0.1 Langmuir exposure to the damaging gases such as H_2O and O_2. The sticking coefficients of the various gases on Co and Cu surfaces could not be found in the literature. However we may be certain that these gas exposures are not sufficient to achieve monolayer coverage. The coverage is likely to be only ~0.1 monolayers of gas atoms at each point where growth was halted.

A series of samples of the form {Co(10Å/Cu(10Å)}×20 were grown on (001) Si wafers. As previously the native oxide layer was preserved on the wafer, and no buffer layer was used. The samples are on the first AF peak of the coupling oscillation. The four different types of gas-damaged sample are illustrated below in Fig 5.1. The sample grown without breaks in growth as a control will be referred to as the *clean sample*.

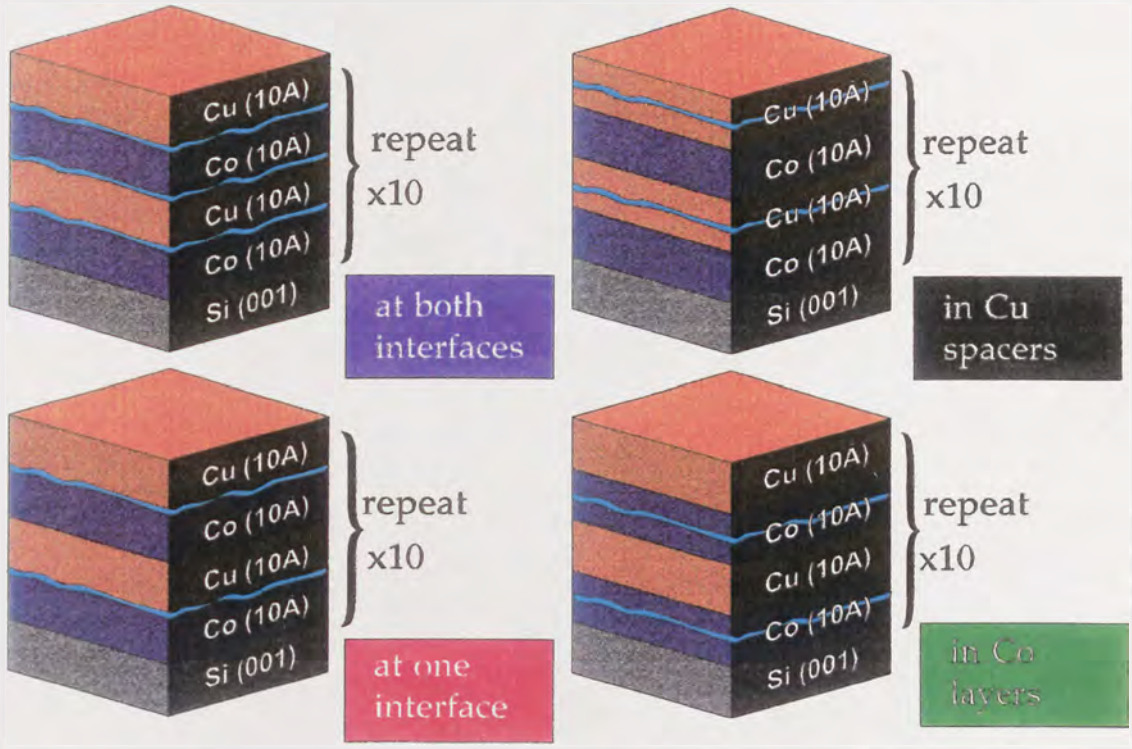

Figure 5.1 The residual gas damage was inserted into a number of multilayers of the form {Co(10Å/Cu(10Å)}×20 grown on (001) Si wafers. The pale blue lines marked on the samples indicate the points in the stack at which the gas-damage was caused.

The room-temperature GMR and MOKE results for these samples are shown in Figs 5.2 and 5.3. The colours of the curves correspond to the colours in the label panels of Fig 5.1. We have been able to use our model described in Chapter 3 to fit to the data and extract the values of the coupling constants. As is common, we have assumed that $\Delta\rho$ is proportional to $(1 - \cos\Theta)$, where Θ is the angle between the magnetisation vectors of adjacent magnetic layers.

The observed GMR ratio correlates with the remanence as measured by MOKE, with the exception of the sample with the impurities in the middle of the Co layer. We will discuss the other samples and then touch on this point briefly below. All the samples had similar values of saturated resistivity, 20±2μΩcm.

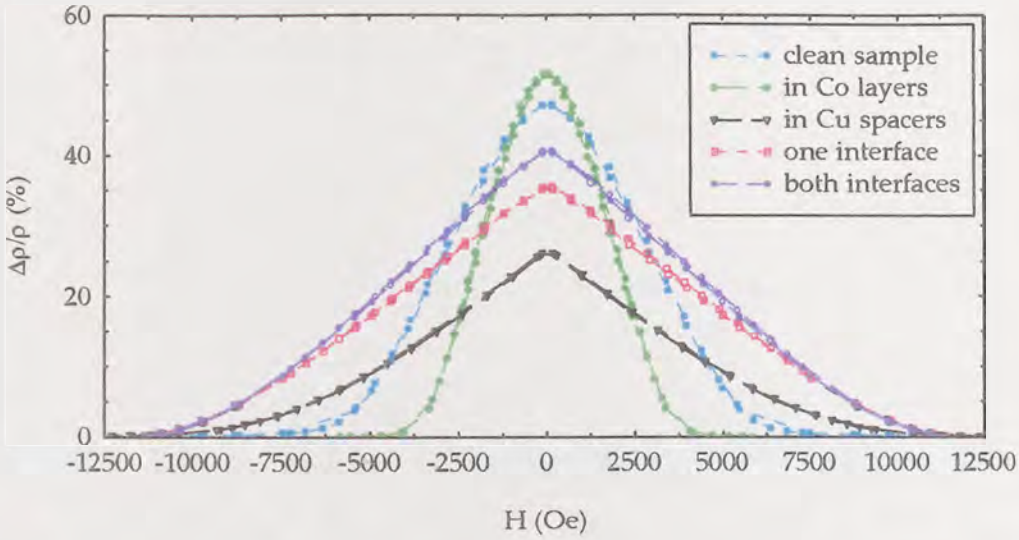

Figure 5.2 The GMR of the various samples at room temperature. The clean sample is seen to possess the largest GMR ratio of all but for the sample with damaged Co layers.

The pure sample can be seen to have a **remanence** of almost zero from the MOKE data - hence this sample should posses the largest possible GMR for a given set of transport parameters. In the **fits to the data all** magnetoresistances are expressed as fractions of this value ($\Delta R/R$ = 47%).

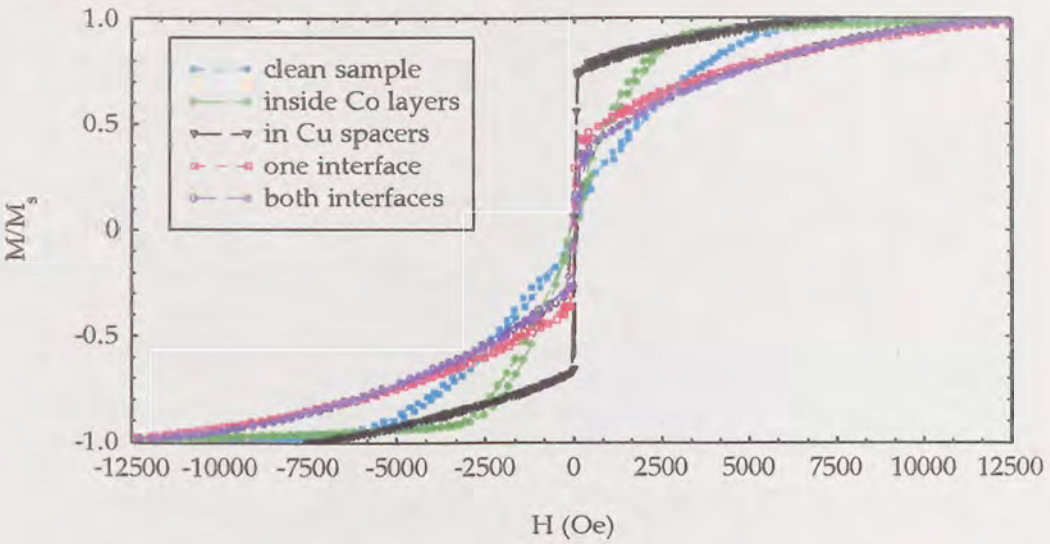

Figure 5.3 MOKE loops of the various samples at room temperature. The clean and Co damaged samples are seen to have a remanent fraction of very close to zero.

Since the curves have symmetry and exhibit no hysteresis we show only one half of the MR loop, and one quadrant of the magnetometry data, although in all panels of Fig 5.4 both forward and backward sweeps are shown. The model does not predict the high field tail of the magnetoresistance well as it does not take into account small effects such as the ordinary magnetoresistance. The values of the coupling constants used in modelling the pure sample were J_1 = -0.14 mJm^{-2}, and J_2 = -0.02 mJm^{-2}, and the fits are shown in Fig 5.4(a). In this sample the bilinear coupling is dominant, as shown by the almost straight MOKE loop, and the parabolic convex form of the GMR response. We have assumed that the magnetisations within each layer are uniform, and that non-collinear coupling may occur, these assumptions will be justified later in this chapter.

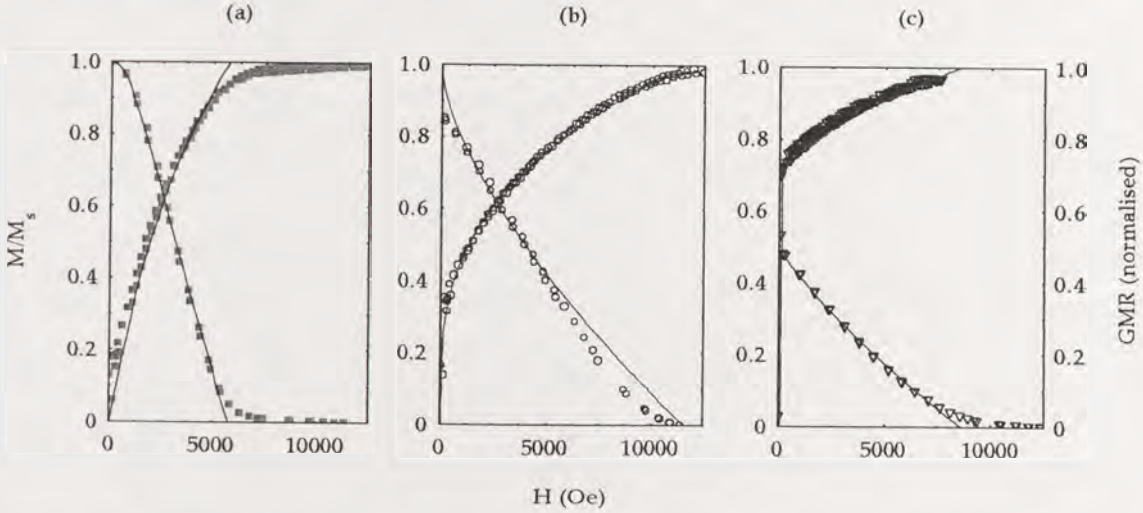

Figure 5.4 Fits to the data using the numerical model described in Chapter 3. The panels are (a) the clean sample, (b) the interface damaged sample, and (c) the spacer damaged sample. In each of the three cases both the GMR and MOKE data were fitted simultaneously using a single set of parameters. The bulk value of M_s for Co was used.

Interface results (shown in Fig. 5.4(b)) are modelled with J_1 = -0.18mJm^{-2} and J_2 = -0.09mJm^{-2}. Here we have a larger biquadratic term - there is an appreciable remanence, indicating that the antiferromagnetic coupling is no longer perfect. Fig. 4(c) presents the results for the sample where the

impurities are in the middle of the spacers. Here there is considerable **remanence** , indicating poor antiferromagnetic alignment in zero field. A purely biquadratically coupled sample would have a **remanent** fraction of $\sqrt{2}/2$, and would display a GMR of half that of a perfectly antiferromagnetic sample. These values are very nearly what we measure, and we are able to calculate the solid line shown using J_1 = +0.01 mJm^{-2}, and J_2 = -0.15 mJm^{-2}. This is a very surprising result. In most multilayer studies there is much emphasis on the interface quality as being a very important aspect of a good GMR sample. We have found here that it is the purity of the spacer, rather than damage at the interfaces which determines the quality of the AF coupling.

When the impurities were placed in the middle of each Co layer, a reduction in saturation field and a small rise in GMR ratio were observed. One might speculate that the impurities had caused the formation of magnetically dead regions inside the Co, reducing the average value of M_s, in turn reducing H_s. One might also speculate that the small but repeatable rise in GMR ratio is due to impurity atoms causing additional spin-dependent scattering, as they are embedded in a ferromagnetic matrix. Another possible explanation suggests itself. In the early 1970's Varma and Hoffman grew Fe films by UHV evaporation, and found that ultrathin Fe films grown sequentially, rather than continuously had a superparamagnetic behaviour above ~80K, as determined by Mössbauer spectroscopy[161]. This indicates that the individual Fe layers are "at least partially magnetically isolated." If we were to have regions in a gas-damaged Co layer which were not coupled by direct exchange interactions we might expect to see small fluctuations in magnetisation direction around zero field which would cause a small GMR enhancement.

The same experiment has also been undertaken using spin-valve structures of the form Co/Cu/Co/FeMn. The FeMn layer exchange-biases the adjacent Co layer so that it is fully saturated in zero field[162]. The antiparallel alignment of magnetic layers required for GMR is now

independent of interlayer coupling. The GMR ratio $\Delta R/R$ of all these samples was found to be in the range 5.8±0.2%, whether or not the sample contained impurity gas atoms, or their whereabouts in the structure. This demonstrates further that the large changes in GMR ratio seen in the multilayer samples are due entirely to changes in the nature of the interlayer coupling.

5.3 BIQUADRATIC COUPLING

5.3.1 Non-collinear ordering

In the previous section we assumed that the magnetisation vector is a constant within each magnetic layer in order to apply the numerical model outlined in Chapter 3. In order to achieve a non-zero remanence, the magnetisation vectors must be allowed to take up a non-collinear state at zero field; i.e. biquadratic coupling must be present.

Few published results in the literature on Co/Cu multilayers prepared by sputtering exhibit the linear, zero-remanence magnetometry behaviour predicted by a straightforward Heisenberg bilinear coupling term. There is typically a measurable remanent fraction, although it can be very small, and also significant curvature in the *M-H* plot. The form of these *M-H* loops has been interpreted in terms of pin-holes [163], or extended linear defects in the Cu spacer layers[164]. In these models there are small regions around the spacer defects where the coupling is ferromagnetic, causing a localised rotation of the moments over these regions. The moments are no longer antiparallel in zero applied field in the neighbourhood of these defects. This has much in common with the Slonczewski model described in Chapter 3. The exchange stiffness within a Co layer is too strong to allow the magnetisation to fracture into domains, but will allow some dispersion of the moments. There have now been observations of 90° configurations of spins in zero applied field (e.g. in Fe/Cr[165], NiFe/Ag[166], and Co/Cu[167]), and the theoretical basis for biquadratic coupling is sound. In particular the results below will be interpreted in terms of the Slonczewski thickness

fluctuation model described in Chapter 3.

In order to determine if the assumptions about biquadratic coupling made above are justified, further samples were grown under the conditions where the biquadratic coupling is strongest - when the gas damage is in the middle of the spacer layer.

5.3.2 Results and Discussion

Two series of multilayers were prepared with variable Cu spacer thickness in the range 7-12Å, that is ranging over the first antiferromagnetic-coupling (AF) peak. All multilayer samples were of the form $\{Co(10Å)/Cu(t_{Cu})\}\times 50$. Each series was grown in a single batch. There was a break in growth in the middle of each of the spacer layers. In the first series (referred to as A) the substrate was moved away from the magnetron, and then returned immediately to allow the completion of the Cu layer. In the second series (B) there was a longer 10s pause to allow the freshly deposited metal surface to be contaminated by residual gas atoms. Exposure was of the order of 0.1 Langmuir, hence coverage is clearly still in the sub-monolayer regime.

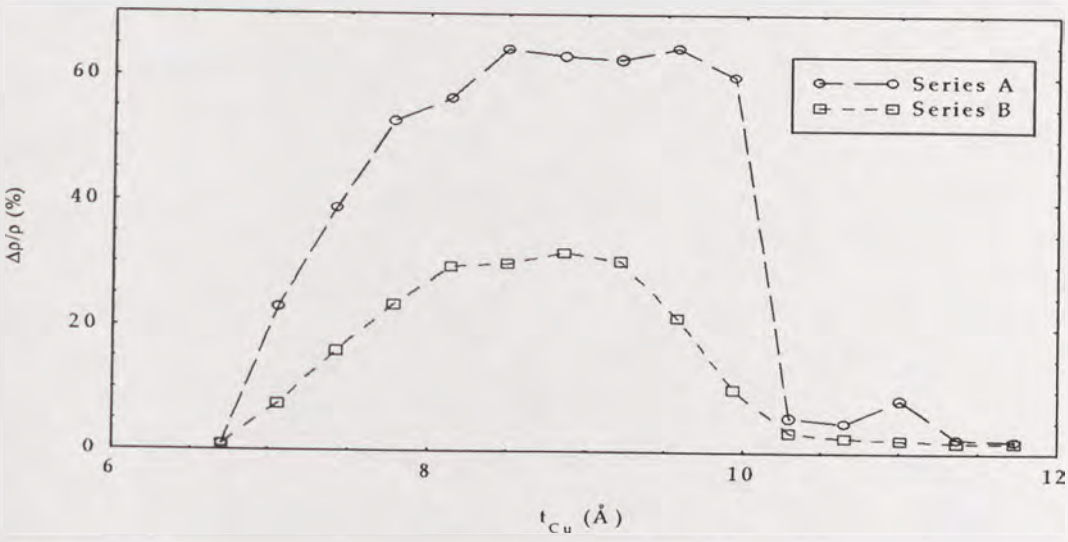

Figure 5.5 The room temperature GMR of Co/Cu multiayer grown with a very short (series A), and a longer pause (series B) in the middle of each Cu spacer layer.

A comparison of the GMR ratios achieved in each series of samples is shown as a function of copper spacer thickness in Fig 5.5. The series A samples with the short breaks in the spacers compare very well with similar Co/Cu multilayer samples where there are no breaks and the spacer layers are of continuous pure copper. In particular both have a peak GMR ratio of a very similar value, ~65%, and very low remanent fractions of <10%. Also both have comparable saturation fields. The shape of the MR curves with field are very similar, with a convex peak. We chose to use series A, rather than a series with unbroken spacers, as our control experiment as the preparation conditions are identical in every way to series B, but for the length of time spent away from the magnetron. However there were no noticeable differences between series A and samples grown without pauses.

The series B samples with 0.1 L of residual gases in each spacer have a significantly lower GMR, close to one-half the value for the first sample at the Cu AF-peak. In addition the shape of the MR curve is significantly different, the sides of the peak around H=0 are concave. The saturated resistivities of these two samples are both 20 ± 1 μΩcm, suggesting that the decrease in GMR ratio is not due to significantly higher spin-independent scattering. MOKE loops for the two samples on the AF peak, show that the series B sample has a significantly higher remanence. Meanwhile that of the series A sample is close to zero, indicating good antiferromagnetic coupling. The different shape of the MR curve suggests that the coupling is of a different form to that seen in a series A sample. If the higher remanence of the sample and the drop in GMR ratio were simply due to a lower antiferromagnetically coupled volume fraction, then the shape of the GMR peak would be the same, but with a smaller height. This suggests that the coupling of the samples is no longer of a pure bilinear form.

When we consider that the GMR depends on -cosΘ, and from the discussion in Chapter 3 we recall that in the absence of symmetry-breaking anisotropies $\Theta=2\theta$ (θ is the angle between magnetisation vector and field), it

can be seen that the zero-field GMR ratio $\Delta\rho_0/\rho_s$ is expected to be proportional to $-(M_0/M_s)^2$ [168]; i.e. the dependence on remanence is parabolic. The common observation that the GMR of an individual sample varies quadratically with the magnetisation is for the same reason; that magnetisation depends on half the angular difference between the moments, which determines the GMR. This parabolic behaviour will only hold for layers which are uniformly magnetised, with the vectors Θ apart, as we have assumed in our model. Suppose we have a sample where a non-zero remanence is achieved by having only a fraction AF-coupled, and the remainder having a parallel alignment. In this case the intralayer exchange stiffness is not sufficient to keep the layers uniformly magnetised, and the GMR ratio will now vary linearly with M if we add the regions in series. This linear type of behaviour has been observed previously in sputtered Co/Cu[169]. We associate the linear behaviour with collinear coupling which is not uniform across the sample, and the parabolic behaviour with non-collinear ordering at zero field.

The value of M_0/M_s for a ferromagnetically coupled sample which exhibits no GMR is 92%. We attribute this to the sample breaking into domains, and so we assign any remanence less than this value to non-ferromagnetic coupling. Such samples will exhibit a GMR. Plotting the remanence against the MR ratio for all the samples of both series A and B (Figure 5.6), we see the expected parabolic dependence is followed fairly well, evidence for non-collinear arrangements of spins in neighbouring Co layers at zero applied field. There are only two samples which fall on the dashed straight line, these are both from series A. These samples are likely to have coupling fluctuations over a longer lateral scale. However it will be noted that every sample from series B appears to follow the solid parabolic curve, showing that the mechanism for reducing the GMR in series B is not adjacent collinear domains forming, but uniformly magnetised layer moments lying at an angle to each other when the field is removed.

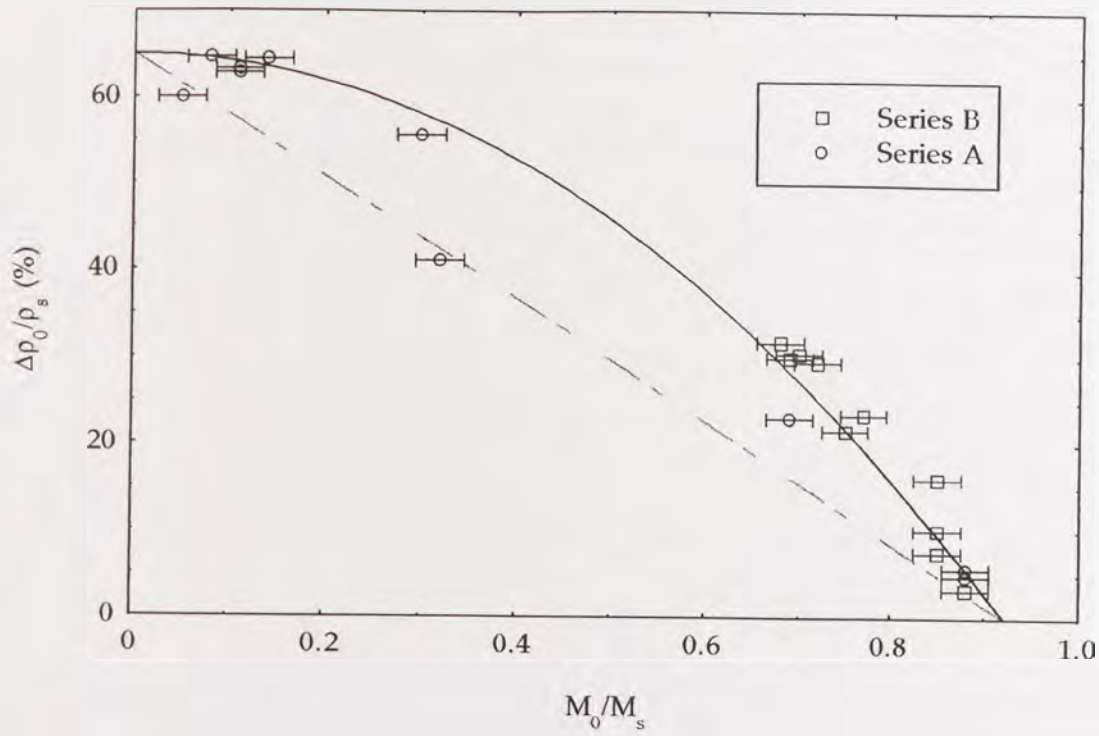

Figure 5.6 - The dependence of zero-field magnetoresistance upon remanence for all the series A and series B samples which exhibit a GMR. The solid line is the parabolic dependence predicted by the biquadratic coupling model with uniformly magnetised layers. The straight line is what would be expected for adjacent collinearly arranged regions separated by domain walls.

In Fig 5.7 we show the results of fitting our MOKE and GMR data and extracting the values of J_1 and J_2, as a function of the Cu spacer layer thickness. In panel (a) we show the results for series A, and we see the expected behaviour for J_1, with a minimum broadly centred near t_{Cu} = 8.5Å, corresponding to the first Cu peak. To either side of the peak mixed coupling occurs. It is likely that in this crossover region there will be parts of the sample which exhibit coupling constants of opposite sign, resulting in a strong biquadratic term. This is very similar to what is observed in the central part of series B. The bilinear term J_1 is very close to zero, but the remnant of the antiferromagnetic peak can still be discerned. Biquadratic coupling overwhelms the antiferromagnetic peak in these samples, similar to

the large values of J_2 seen in the crossover from positive to negative sign coupling in series A. It seems that there are such large coupling-fluctuations over the surface of the samples in series B that it is never possible for strong antiferromagnetic coupling to occur. The best that can be achieved is the very weak AF peak seen in Fig 5.7(b), and biquadratic coupling dominates even at this spacer thickness, just as on the edges of the AF peak in series A.

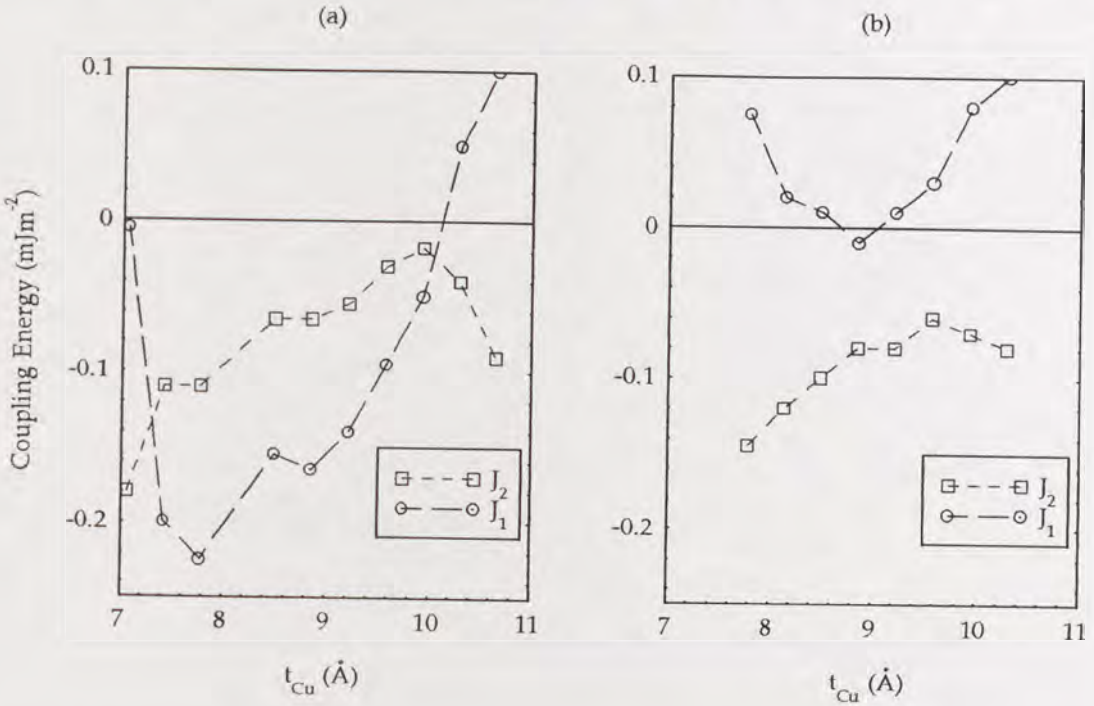

Figure 5.7 The value of the bilinear and biquadratic coupling constants as a function of Cu spacer thickness for (a) series A samples and (b) series B samples, as determined by fitting MOKE and MR loops by following the path of least energy.

Initially one might therefore suppose that the biquadratic coupling is described by the thickness fluctuation model. This would be supported by the fact that when we performed this experiment on two series of samples grown over the 2nd Cu AF-coupling peak at 22Å these samples did not show significant differences: the highest GMR achieved in this series A was 28.8% for {Co(10Å)/Cu(22Å)}×25, with a very short break in growth in the centre of each spacer; for series B, with a 10s break in growth in the centre of

each spacer the highest GMR was 27.2% for a similar sample. The 2nd peak is usually found to be much broader than the first[170], and so small thickness fluctuations will probably lead to very little mixed coupling of the kind which can cause a strong biquadratic term.

However a closer examination of Fig 5.7 reveals that the strength of the biquadratic coupling found from our model is very similar in both panels. The large change is in J_1, which goes from being strong enough to be dominant in the centre of panel (a) so that in the system is just inside the phase AF1. Meanwhile in the central part of panel (b) the value of J_1 is very close to zero. This is subtly different to the results presented in the previous section, where J_2 was much closer to zero in the clean sample. The results in this section seem to indicate more that the damage in the spacer layer does not *cause* the biquadratic coupling, but reduce J_1 to a level where J_2 is dominant.

Therefore it is difficult to reconcile the results shown in Fig 5.7 with the thickness fluctuation model – it is hard to see how there can be the same amount of mixed-sign coupling in both sets of samples when the measured values of the bilinear coupling energies are so different. However no other model offers an easy interpretation of the data – intrinsic models predict coupling orders of magnitude weaker. The temperature dependence of biquadratic coupling due to loose spins is very rapid, and this is examined in the next section.

5.4 Temperature Effects

5.4.1 Temperature dependence of indirect coupling

The theories of indirect exchange coupling described in Chapter 3 have primarily concerned themselves with correctly predicting the oscillatory behaviour, and in particular the period. These theories also often have an associated temperature dependence of the coupling energy, and there have been various predictions of the behaviour of the coupling above the

theoretical ideal of 0K[171,172]. However this aspect has received markedly less experimental attention.

We have been able to locate in the literature studies on the temperature dependence of the coupling of Fe through Cr[173], Al[174], Cu and Ag[175] and Mo[176] spacers, variously reporting the temperature dependence of J_1, and/or J_2. The behaviour of J_1 with temperature has also been measured in the strongly coupled Co/Ru system[177] as well as very recently for Co/Cu[178]. Therefore the temperature dependence of both J_1 and J_2 were investigated in our Co/Cu samples exhibiting both kinds of coupling. A pair of samples from the top of the GMR peak were chosen from series A and series B, both with the same Cu thickness.

5.4.2 Saturation Magnetisation

The magnetisation loops of these two samples were measured using a SQUID magnetometer with the field applied in the layer planes at Michigan State University. The magnetisation loops were measured out to ±4T in order to give a large saturated region where the diamagnetic background signal could be measured. This was fitted by a straight line and subtracted off. The slope of the line was found to be the same at large positive and negative fields.

The measured saturation magnetisation M_s for each of the samples is shown in Figure 5.8. We have fitted the data with a curve of the form $M_s(T)=M_0(1-\alpha T^n)$. We find that M_0 is a little less than the bulk handbook value of 1.422×10^6 A/m. We might attribute this to the microstructure of the Co layers, as revealed by ^{59}Co NMR, where it was found that a fraction of the magnetic layers consisted of a ferromagnetic CoCu alloy. This would reduce the effective moment of those Co atoms in the alloy, although it is difficult to quantify if this exactly explains the reduction in moment. Other intermixture at the interfaces between the large pure Co platelets and also the extreme thinness of the Co layers may play a role here.

Qiu *et al.* [179] predict that an antiferromagnetically coupled multilayer should have $n=2$ in the above expression. Our curve of best fit has $n=2.04$, a

remarkably good agreement, despite us having used a magnetometer to measure M_s, rather than a zero-field technique such as the Mössbauer measurements Qiu *et al.* performed to confirm their prediction. Using the same function to fit the biquadratic sample we find that the value of n is 2.93, very close to a cubic behaviour. Qiu *et al.* predict and measure the normal Bloch law (that n=3/2) for ferromagnetically coupled samples and also find a quasilinear T dependence for M_s in uncoupled layers as predicted[180].

They make no mention of biquadratic coupling, but Brown calculated the properties of a bulk ferromagnet with a biquadratic term in the Hamiltonian over 25 years ago[181]. Although this does not exactly represent our samples a number of qualitative predictions of a general nature are made, in particular that M_s decreases as a significantly higher power than in the normal Bloch law behaviour.

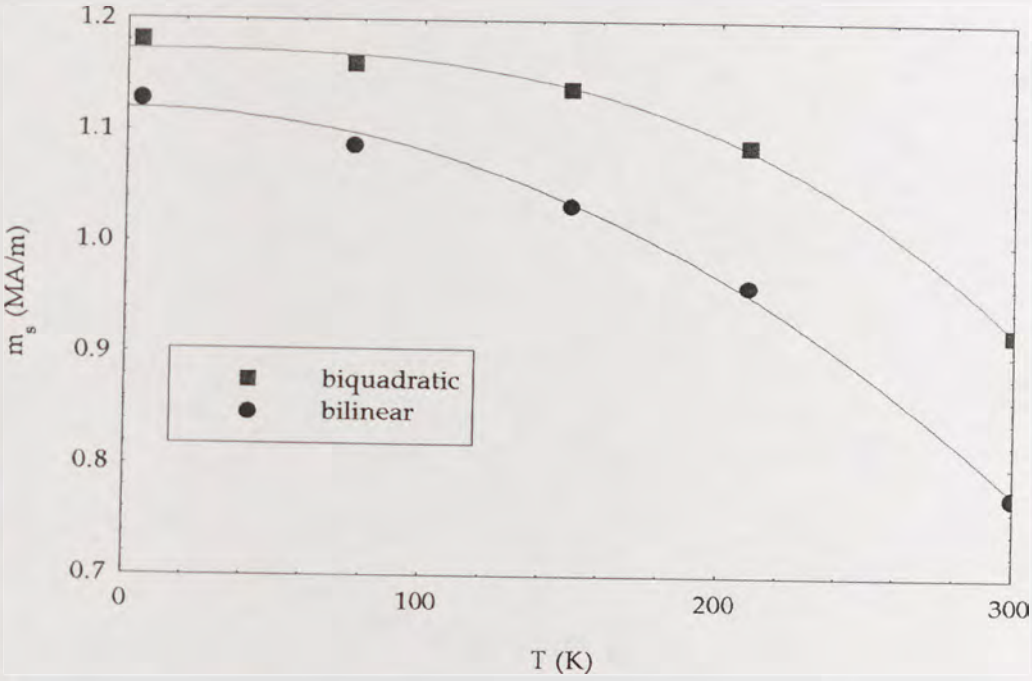

Figure 5.8 Saturation magnetisation of bilinearly and biquadratically coupled Co/Cu multilayers with temperature. The solid lines are curves of best fit.

Although it is not valid to use the above functional form for $M_s(T)$ close to the Curie point, we can estimate it by extending the curve to $M_s(T)$=0. We

find that for the bilinear sample the Curie point is only 540K, less than half the bulk value for Co. This is to be expected for such thin Co layers. For the biquadratic sample we estimate the Curie temperature to be 500K, lower than for the bilinear case, again consistent with Brown's predictions for biquadratic exchange.

5.4.3 Temperature Invariant Magnetisation Loops

A remarkable feature of all these *M-H* loops is that once the magnetisation is normalised and plotted as $M(H)/M_s$, the curves collapse on top of each other for all the temperatures measured. This means that the samples saturate at the same field independent of temperature, and also show a common **remanent** fraction. In order to understand the implications of this result we must first of all examine the various energy terms involved in coupling across a non-magnetic spacer.

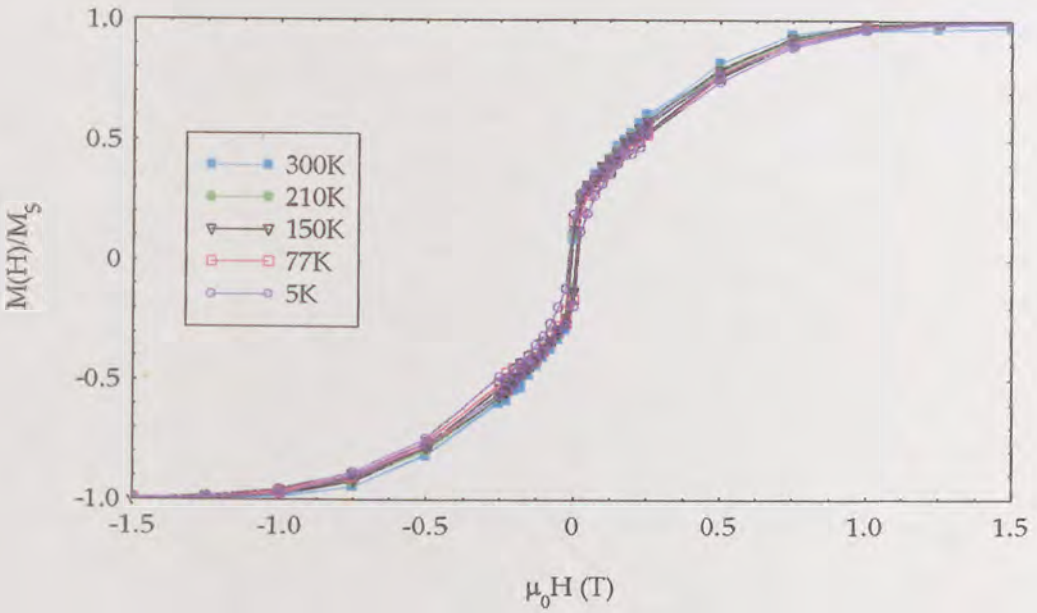

Figure 5.9 Normalised magnetisation loops of bilinearly coupled sample at various temperatures. All loops collapse onto a common curve.

In Fig 5.9 we show the normalised SQUID loops for the bilinear sample at the different temperatures measured. Fig 5.10 shows the same data for the biquadratic sample. The saturation field, **remanent** fraction and shape of the

curve do not change. The only differences are a small amount of hysteresis around zero field at the lowest temperatures. In this field range there is a very rapid rotation of the moments, and if the thermal fluctuations are not sufficient to allow this movement over pinning defects then the energy will have to be found from the applied field. The magnetisation will slightly lag the path of global minimum energy predicted by the model given above. These deviations are not significantly large however.

If the remanent fraction does not vary with temperature then we can see that the ratio of J_1 and J_2 must be a constant with temperature, so that the zero-field angle between adjacent layer moments does not change as the sample is cooled or warmed. The two coupling constants must share a common temperature dependence - meaning that $J_{eff}=(J_1+2J_2)$ has this same dependence on temperature.

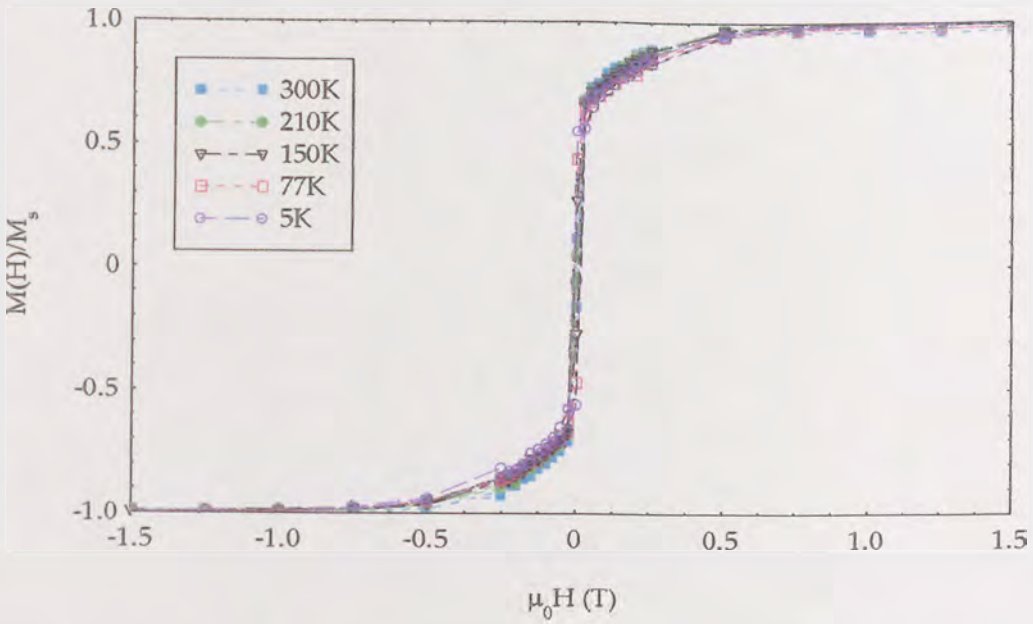

Figure 5.10 Normalised magnetisation loops of biquadratically coupled sample at various temperatures. All the loops collapse onto a common curve.

Celinski *et al.* found a similar linear behaviour of J_2 with J_1 in their Fe/Cu samples[175], and ascribed J_2 to the thickness fluctuation model. At first sight the thickness fluctuation model shows a quadratic behaviour,

$J_2 \propto (J_1^2)$. The full expression for biquadratic coupling in the Slonczewski model (see section 3.2.4.3) approximates to

$$J_2 = \frac{4}{\pi}\Delta J_1 \left(\frac{\Delta J_1 / m_s D}{2Ak^2 / m_s} \right)$$

for the case $D/L \ll 1$, where $k = \pi/L$. The term in brackets that scales down ΔJ_1 contains the ratio of the fluctuating interlayer exchange ($\Delta J_1/M_sD$) to the intralayer exchange ($2Ak^2/M_s$). They argued that so long as these two different exchange interactions have the same temperature dependence, then this bracketed term will be a constant with temperature. This requires a strong dependence of A on T, which, like Celinski *et al.*, we find rather surprising. Again the present data seems not to be consistent with the thickness fluctuation model. This linear behaviour is also seen in recent measurements by Chesman *et al.* on Fe/Cr[182].

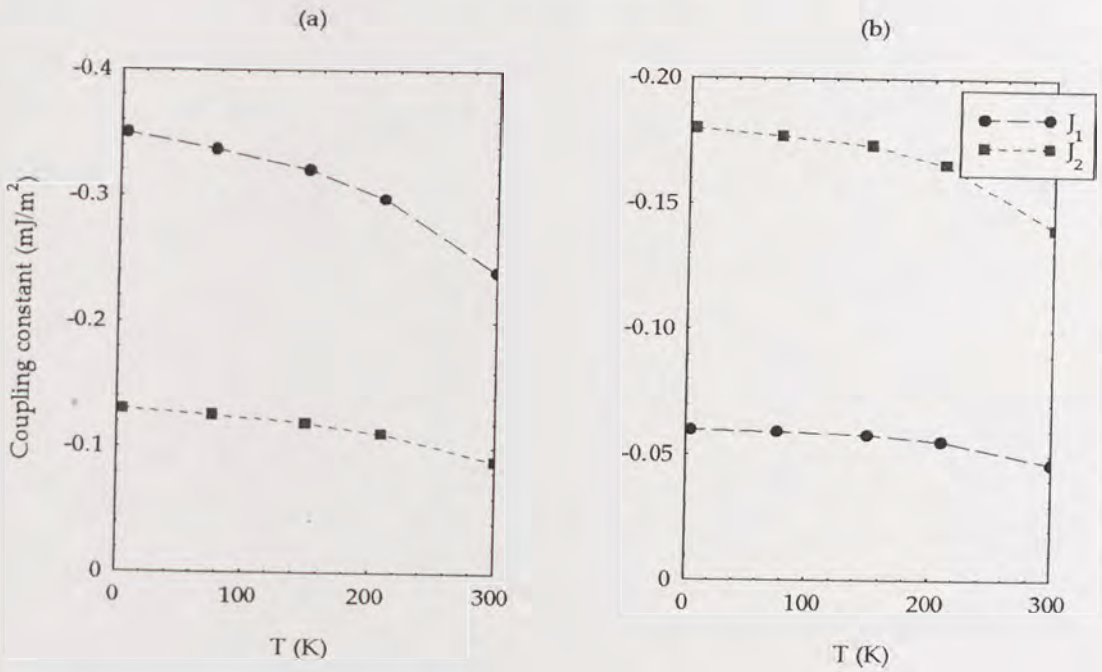

Figure 5.11 Temperature dependence of bilinear (J_1) and biquadratic (J_2) coupling constants in (a) Co/Cu multilayer with good spacers and (b) damaged copper layers. The broken lines merely connect the points.

We have fitted the SQUID loops by following the path of minimum energy in the numerical model, using the measured value of M_s at each temperature. The results of this procedure are shown in Figure 5.11. The coupling

constants are seen to saturate at low temperatures, in common with other studies[18,20]. This was not observed by Chesman *et al.*, and the low temperature saturation region is extremely small in the results of Gutierrez *et al.* This saturation at low temperatures is common to theoretical predictions, and in particular that of d'Albuquerque e Castro *et al*[172]. Here the temperature dependence of the coupling was calculated for a Co/Cu/Co trilayer, and found to be more rapid than would be expected from considering only the smearing of the Fermi surface as the temperature is raised. Since the Fermi level is very close to the top of the potential well, as the temperature is raised the quantum confinement is much less effective, and the coupling energy falls more rapidly. The large drop in the coupling constant on warming from zero to 300K is similar to that we observe. In the weeks whilst this thesis was being written results on the temperature dependence of the bilinear coupling in Co/Cu were published[178], with the results agreeing broadly with ours and with the predictions of d'Albuquerque e Castro *et al.*

The constant saturation field with temperature shows that J_{eff} shares a common temperature dependence with magnetisation so that the ratio J_{eff}/M_s (defining H_s) does not change. Previous measurements of the dependence of the interlayer coupling on magnetic moment have been performed, by Kubota *et al*[183], and by Kubinski and Holloway[184]. Both decreased the moment of the Co layers by alloying, with Ni or with Cu respectively. Both groups observed that the interlayer exchange was proportional to the square of the magnetisation of the layers.

One would normally expect exchange interactions to be independent of magnetisation, and so this seems at first to be surprising. It seems likely that such a common functional form for J_1, J_2 and M_s stems from some common underlying phenomenon, rather than from a direct causal relationship. The underlying mechanism is still unknown.

5.5 CONCLUSIONS

When investigating the effects of residual gases at different parts of he multilayer stack, it was found that the region where the effects of the damage was most severe was not the interfaces between the Co and Cu layers. Residual gases in the middle of each Cu spacer were the most damaging, causing the largest reduction in GMR. Changes in the GMR for such samples were driven by changes in the nature of the coupling, with the remanent fraction being much larger for samples with a smaller GMR.

The nature of the relationship between the remanent fraction and the difference in zero and high field resistivities was found to be parabolic, i.e. $\Delta\rho \propto -(M_0/M_s)^2$. This indicates that the mechanism by which spacer gas damage increases the remanence from a perfect zero is not by breaking the sample up into ferro- and antiferromagnetically coupled fractions, but by causing non-collinear ordering of the moments by means of biquadratic coupling. The magnetisation remains uniform within each Co layer, allowing a simple numerical model to be used to fit the data. The values of the coupling constants were determined, and values of the bilinear coupling constant were found to be in agreement with those in the literature. Values of the biquadratic coupling constant were found to be surprisingly large, although similarly strong orthogonal coupling has been previously observed in a number of other systems.

We have measured the temperature dependence of the saturation magnetisation (intralayer exchange) and indirect interlayer exchange of Co/Cu multilayers exhibiting both predominantly bilinear and biquadratic exchange. We found that the saturation magnetisation does not follow the usual $1\text{-}T^{3/2}$ Bloch law in either case. The antiferromagnetic bilinear sample followed a $1\text{-}T^2$ behaviour, as predicted theoretically. The biquadratically coupled sample followed a $1\text{-}T^3$ curve, consistent with more qualitative predictions by Brown.

Normalised magnetisation loops did not change with temperature, implying a common functional form for the saturation magnetisation, and

both the bilinear and biquadratic coupling constants. The nature of the relationships between these three variables is as yet unknown.

It is also not clear to which theoretical model describes the biquadratic coupling. The magnitude of J_2 is too large for the models of intrinsic coupling to be applicable. Meanwhile, the two extrinsic models proposed also do not correctly fit the data in a number of important ways. The data shown in Fig5.7 seem to indicate that the thickness fluctuation model is not correct, and this is backed up by the linear relationship between J_1 and J_2 as the temperature is varied, which cannot be explained without unreasonable assumptions. This temperature dependence also suggests that loose spins are not the correct model, as one would expect to see a much faster temperature dependence for the biquadratic coupling energy than for the bilinear. This linear relationship is a common observation by others, and further theoretical clarification seems to be needed.

The exact nature of the damage caused by the gas is also unclear. Detailed microstructural analyses, as described in Chapter 4, failed to find any differences between samples grown in different vacuum conditions, with very different magnetic and magnetotransport properties. Others studies reported in the literature describe H_2O and O_2 as very damaging residual gases, causing oxidation of the sample.

It is also possible that the gas atoms which are adsorbing onto the freshly deposited Cu surface during the break in growth are acting as surfactants, modifying the growth mode for additional Cu growth. Such behaviour is in fact commonplace[185]. Gas atoms have been known to affect the growth of thin films quite drastically in the past [186], and to have an effect in this way on the roughness and GMR of delicate magnetic multilayered structures in particular[187].

6. In Conclusion

6.1 Summary

As stated at the beginning of this thesis the primary objective was to build a sputtering system capable of growing a large number of magnetic multilayer samples in a single vacuum cycle. Once the initial design and construction of the required new hardware and software was completed, we set about testing the system by trying to grow samples from one of the most widely studied systems in the field - Co/Cu multilayers.

One of the principle advantages of sputtering over evaporation techniques is the much larger number of parameters which can be adjusted to provide fine control over the properties of the growing film. Naturally in the early stages of process development this leads to a wider variety of possible starting points in the search for the optimal growth conditions. It was the result of many months work to finally produce the first samples with a respectable GMR ratio. The critical factor, beyond having the correct target-substrate distance, sputtering pressure, gas purity, target current and thickness calibrations, was the cleanliness of the initial vacuum. Installation of the liquid nitrogen Meissner trap was found to improve the base pressure by about an order of magnitude, and the GMR increased by more than a similar factor. This is principally due to the trap's effectiveness in the pumping of that most damaging of residual gases, water vapour. However detailed structural analyses were unable to reveal the damage that the background gases were causing. However an unusual microstructure was discovered using X-ray analysis the individual grains showed poor orientation, with {111} directions tilted away from the layer normal with a distribution half-width of 8°. On the other hand, the layering was excellent, with rms roughnesses on the scale of less than an atomic diameter. This implies that the interfaces would have the character of vicinal surfaces, with

miscuts of up to 8°. ^{59}Co NMR analysis confirmed the layer smoothness.

Once the system was reliably growing high GMR Co/Cu samples, a fuller characterisation of the samples was in order. This system traditionally shows strong oscillations as the Cu spacer thickness is increased, and we observed three periods of this oscillation before the layers became uncoupled at large Cu thicknesses. The period of this coupling is determined by spanning vectors across the Cu Fermi surface, which are parallel to the layer normal. Our layers are close to {111} oriented, where the Cu Fermi surface has necks that connect across the Brillouin zone boundary. Since the Fermi surface is highly non-spherical in these regions tilting the spanning vector by only 8° to keep it parallel to the layer normal will affect it s length drastically. The coupling in each grain will therefore oscillate with a different period depending on it's orientation relative to the layers. We propose that these periods will undergo some form of averaging process in order to produce the strong macroscopic oscillation observed.

There have also been predictions, and even one or two observations, of ferromagnetic layer thickness dependent coupling oscillations. Our attempt to observe such oscillations failed - the coupling energy was constant as the Co thickness was varied over a wide range. In terms of one particular model (due to Barnas) this was not at all surprising - for reasonable values of the exchange splitting the oscillations are so severely damped that none can be observed for magnetic layer thicknesses greater than a few Å.

We return now to the question of residual gas damage. Since no structural effects of the damage could be observed, we attempted to at least discover which parts of the structure the gas was damaging. To accomplish this, we used the novel technique of pausing growth under clean conditions part way through the stack, and allowing a small amount of gas to accumulate on the sample surface. This allowed us to selectively damage different points in the sample, and then measure the effects. Contrary to our expectations that the interfaces between Co and Cu would be of paramount importance, it was found that the centre of the spacer layer was the place

where damage was most severe.

Using a simple numerical model we were able to fit the magnetometry and GMR loops of various clean and damaged samples. Most interestingly, whilst a clean sample exhibited near perfect bilinear antiferromagnetic coupling, a sample with a damaged spacer was fitted by assuming that the coupling was almost totally biquadratic in nature. Subsequently examining the GMR vs. remanence curve of a series of such samples indicated that the coupling was indeed of this biquadratic form.

The temperature dependence of the magnetisation and coupling constants was measured in the range of 5 - 300K. The magnetisation was found not to obey the Bloch law, but to fall off like $1\text{-}T^2$ for an antiferromagnetically coupled sample, and like $1\text{-}T^3$ for a biquadratic sample. Both these behaviours were found to be consistent with theory, although specific predictions for a biquadratically coupled multilayer have not been made.

When the magnetisation loops for a particular sample were normalised it was found that for each sample the loop was independent of temperature. Important quantities such as the remanent fraction and the saturation field, as well as the overall shape of the loop, were unchanged throughout the entire temperature range. This has a number of consequences - firstly that the bilinear and biquadratic coupling constants have a linear relationship to one another. This has been observed by others on a number of occasions in other systems, but is in conflict with theoretical predictions. Secondly a plot of interlayer coupling energy vs. saturation magnetisation would yield a straight line - conflicting with both previous observations and the theory. The causes of this behaviour are unknown.

6.2 The Future

There are still a number of aspects of this work which deserve further attention. In particular the exact effects on the microstructure which the residual gas atoms have, and how this affects the coupling remain a deep

mystery. The changes in structure must be very subtle to have escaped detection by detailed NMR and X-ray analysis, yet the effects on the magnetic properties of the samples are drastic. Differentially pumping the RGA head of the sputtering system may allow for real-time background gas measurements during growth, and other structural characterisation techniques such as transmission electron microscopy may be able to shed light on the exact nature of any morphological changes.

The temperature dependence of the magnetisation in a biquadratic sample has yet to be predicted in a quantitative way, and a calculation which predicted the observed behaviour similar to those available for ferro- and antiferromagnetically coupled samples would be most welcome. The observed scaling behaviour between the two coupling constants and the magnetisation as a function of temperature also defies explanation at present.

Of course Co/Cu samples are amongst the oldest types of multilayer, and along with Fe/Cr are doubtless the most widely studied. Nevertheless papers on this system are still being published, and the large GMR available makes Co/Cu promising for simple position sensing applications. For demanding read-head applications however, the vastly superior sensitivity of biased spin-valve structures is required. Basic versions of such structures have been grown already using the sputtering machine, and the development of a usable spin-valve device is an important goal from a technological point of view.

6.3 In conclusion

Sputtered Co/Cu magnetic multilayers have traditionally possessed good magnetotransport properties, and samples grown by that technique over the course of this work have yielded very high magnetoresistances, close to the highest reported values in the literature. However much of the work reported in this thesis has focused on the interlayer coupling in the Co/Cu system. Theoretical models of this coupling usually assume perfect crystallinity, with the layers lying along some set of atomic planes with low

Miller indices. We have shown that in practice such crystal quality is unnecessary, and that smooth layers of well-defined thickness are the necessary condition for good interlayer coupling. This sits well with present broad theoretical ideas, where the multilayer is treated like a Fabry-Perot interferometer, with interfering electron wave-functions giving rise to the oscillatory coupling. There have been attempts to deal with some specific forms of disorder theoretically, but a full and comprehensive treatment is for the future.

Despite the huge research effort invested in the magnetic thin-film field over the previous decade, interest in the area remains as intense as ever. In excess of a thousand papers on some aspect of the topic are published yearly. This is in no small way due it s broad appeal. A number of very fundamental questions about ultrathin magnetic structures remain unanswered. Meanwhile new phenomena such as the GMR, which will celebrate only the tenth anniversary of its discovery next year, will find commonplace technological applications in the data storage and sensor industries with the turn of the millennium. The demand for research in this area remains strong across the board, and doubtless more new physics remains to be discovered.

REFERENCES

1 W Thomson *Philosophic Magazine* London (1858)

2 J C S Kools *IEEE Trans Mag* **32**(4) pp3165-3184 (1996)

3 D W Hone and P M Richards *Annu Rev Mater Sci* **4** pp337-363 (1974)

4 M N Baibich, J M Broto, A Fert, F Nguyen van Dau, F Petroff, P Etienne, G Creuzet, A Frederich and J Chazelas *Phys Rev Lett* **61** p2472 (1988)

5 B Heinrich and J F Cochrane *Advan Phys* **42**(5) pp523-639 (1993)

6 A J Freeman and R Wu *J Magn Magn Mater* **104-107** ppL1-L6 (1992)

7 *Ultrathin Magnetic Structures vols 1 & 2*, eds. J A C Bland and B Heinrich (Springer-Verlag, Berlin 1994)

8 G R Taylor, A Isin and R V Coleman *Phys Rev* **165**(2) pp621-631 (1968)

9 R L White *IEEE Trans Mag* **28**(5) pp2482-2487 (1992)

10 B Dieny *J Magn Magn Mater* **136** pp335-359 (1994)

11 W R Grove *Philos Trans Faraday Soc* **87** (1852)

12 B Window *J Vac Sci Tech* **A11**(4) pp1522-1527 (1993)

13 P F Carcia, S I Shah and W B Zeper *Appl Phys Lett* **56**(23) pp2345-2347 (1990)

14 D M Donnet, K Tsutsumi, P de Haan & J C Lodder *J Appl Phys* **79**(8) pp6243-6245 (1996)

15 F M Penning *Physica* **3**(9) pp873-894 (1936)

16 J S Chapin *Res Develop* **25**(1) p37 (1974)

17 I G Kaeser and V V Pashkova *Sov Phys - Tech Phys* **4** pp254-264 (1959)

18 Another advantage of sputtering is that there is virtually no material which cannot be deposited.

19 I K Schuller & C M Falco *Surface Science* **113** pp443-453 (1982)

20 R E Somekh, K H Huang & W C Shih *Vacuum* **38**(8-10) pp693-697 (1988)

21 S S P Parkin (1996 unpublished)

22 W F Egelhoff Jr, P J Chen, C J Powell, M D Stiles, R D McMichael, J H Judy, K Takano and A E Berkowitz (1997 preprint)

23 e.g. H P Myers (1990) *Introductory Solid State Physics* Taylor & Francis (London) p478

24 W F Egelhoff, P J Chen, C J Powell, M D Stiles, R D McMichael, C-L Lin, J M Sivertsen, J H Judy, K Takano, A E Berkowitz, T C Anthony & J A Brug *J Appl Phys* **79**(8) pp5277-5281 (1996)

25 M H Read & C Altman *Appl Phys Lett* **7** p51 (1965)

26 S Honda, S Ohmoto, R Imada & M Nawate *J Magn Magn Mat* **126** pp419-421 (1993)

27 H Kano, K Kagawa, A Suzuki, A Okabe, K Hayashi & K Aso *Appl Phys Lett* **63**(20) pp2839-2841 (1993)

28 H Zhang, R W Cohrane, Y Huai, Ming Mao, X Bian & W B Muir *J Appl Phys* **75**(10) pp6534-6536 (1994)

29 T Kingetsu & F Yoshizaki Jpn J Appl Phys 33 pp2041-2042 (1994)

30 G R Harp & S S P Parkin *Appl Phys Lett* **65**(24) pp3063-3065 (1994)

31 B A Movchan and A V Demchishin *Phys Met Metallog* **28**(4) pp 83-90 (1969)

32 J A Thornton *J Vac Sci Tech* **11**(4) pp666-670 (1974)

33 J A Thornton *Annu Rev Mater Sci* **7** pp239-260 (1977)

34 R W Smith and D J Srolovitz *J Appl Phys* **79**(3) pp1448-1457 (1996)

35 G S Bales and A Zangwill *J Vac Sci Tech* **A9**(1) pp145-149 (1991)

36 R Messier, A P Giri and R A Roy *J Vac Sci Tech* **A2**(2) p500-504 (1984)

37 R Berisch, Ed. (1981) *Sputtering by Particle Bombardment* Springer, Berlin

38 R E Somekh *Vacuum* **34**(10-11) pp987-990 (1984)
39 R E Somekh *J Vac Sci Tech* **A2**(3) pp1285-1291 (1984)
40 R Frerich *J Appl Phys* **38** pp1898-1899 (1962)
41 L I Maissel and P M Schaible *J Appl Phys* **36**(1) pp237-243 (1965)
42 H F Winters and E Kay *J Appl Phys* **43**(3) pp794-799 (1972)
43 T Kingetsu & F Yoshizaki *Jpn J Appl Phys* **33**(11) pp6168-6172 (1994)
T Kingetsu & F Yoshizaki Jpn *J Appl Phys* **33**(6B) ppL854-L856 (1994)
44 R J Highmore, W C Shih, R E Somekh & J E Evetts *J Magn Magn Mat* **116** pp249-258 (1992)
45 J C S Kools *J Appl Phys* **77**(7) pp2993-2998 (1995)
46 E E Fullerton, D M Kelly, J Guimpel, I K Schuller and Y Bruynseraede *Phys Rev Lett* **68**(6) pp859-862 (1992)
47 J A Thornton and D W Hoffman *J Vac Sci Tech* **A3**(3) pp576-579 (1985)
48 A G Dirks & H J Leamy *Thin Solid Films* **47** pp219-233 (1977)
49 Details of the very early X-ray work may be found in W L Bragg *Proc Cam Phil Soc* **17** pp43-57 (1912). W L Bragg was the son of W H Bragg, Cavendish Professor at Leeds. They jointly received the Nobel Prize for their pioneering work on X-ray crystallography.
50 H Kiessig *Ann Phys* **10**(5) pp769-788 (1931)
51 A Segmüller and M Murakami in *Thin Films from Free Atoms and Particles* (ed. K J Klabunde) Academic Press, New York (1985)
52 A Segmüller *Thin Solid Films* **18** pp287-294 (1973)
53 L Névot and P Croce *J Appl Crystallog* **8** p304-314 (1975)
54 P Croce, G Devant, M G Sere and M F Verhaeghe *Surf Sci* **22** pp173-186 (1970)
55 A Segmüller, P Krishna and L Esaki *J Appl Crystallog* **10** pp1-6 (1977)
56 taken from S M Sze *VLSI Technology 2nd Ed.* p188 (McGraw-Hill, New York) 1988
57 K Fuchs *Proc Cambridge Phil Soc* **34** p100 (1938)
58 K Chopra *Thin Film Phenomena* McGraw-Hill, New York (1969) pp345-355
59 C Maurain *J Phys* **1** pp90-100 (1902), *ibid* p151-156
60 J C Bruyère, G Clerc, O Massenet, D Paccard, R Montmory, L Néel, J Valin and A Yelon *IEEE Trans Mag* **1**(3) pp174-180 (1965)
61 B Dreyfus, R Maynard and A Quattropani *Phys Rev Lett* **13**(11) pp342-343 (1964)
62 O Massenet, F Biraget, H Juretschke, R Montmory and A Yelon *IEEE Trans Mag* **2**(3) pp553-556 (1965)
63 P Grünberg, R Schreiber, Y Pang, M B Brodsky and H Sowers *Phys Rev Lett* **57**(19) pp2442-2445 (1986)
64 S S P Parkin, N More and K P Roche *Phys Rev Lett* **64**(19) pp2304-2307 (1990)
65 J J de Miguel, A Cebollada, J M Gallego, R Miranda, C M Schneider, P Schuster and J Kirschner *J Magn Magn Mater* **93** pp1-9 (1991)
66 A Fuß, S Demokritov, P Grünberg and W Zinn *J Magn Magn Mater* **103** ppL221-L227 (1992)
67 S S P Parkin *Phys Rev Lett* **67**(25) pp3598-3601 (1991)
68 M T Johnson, S T Purcell, N W E McGee, R Coehoorn, J aan de Stegge and W Hoving *Phys Rev Lett* **68**(17) p2688-2691 (1992), also ref 9
69 P M Levy, K Ounadjela, S Zhang, Y Wang, C B Sommers and A Fert *J Appl Phys* **67** p5914 (1990)
70 M van Schilfgaarde and F Herman *Phys Rev Lett* **65** p1923 (1993)
71 H Hasegawa *Phys Rev B* **42** p2368 (1990)
72 D Stoeffler, K Ounadjela and F Gautier *J Magn Magn Mater* **93** p386 (1991)

73 M A Rudermann and C Kittel *Phys Rev* **96** p99 (1954)

74 T Kasuya *Prog Theor Phys* **16** p45 (1956)

75 K Yosida *Phys Rev* **106** p893 (1957)

76 A Bardasis, D S Falk, R A Ferrell, M S Fullenbaum, R E Prange and D L Mills *Phys Rev Lett* **14**(9) pp298-300 (1965)

77 J Friedel *Nuovo Cimento Suppl* 7(2) pp287-311 (1958)

78 C Kittel *Solid State Phys* **22** pp1-26 (1968)

79 C F Majkrzak, J Kwo, M Hong, Y Yafet, D Gibbs, C L Chien and J Bohr *Advan Phys* **40**(20) p99-189 (1991)

80 Y Yafet *J Appl Phys* **61**(8) pp4058-4060 (1987), *Phys Rev B* **36**(7) pp3948-3949 (1987)

81 R Coehoorn *Phys Rev B* **44**(17) pp9331-9337 (1991)

82 P Bruno and C Chappert *Phys Rev B* **46**(1) pp261-270 (1992)

83 D M Edwards and J Mathon *J Magn Magn Mater* **93** pp85-88 (1991)

84 D M Edwards, J Mathon, R B Muniz and M S Phan *Phys Rev Lett* **67**(4) pp493-496 (1991)

85 C Kittel *Introduction to Solid State Physics* 5th edition Wiley, New York (1976)

86 J Mathon, M Villeret and D M Edwards *J Magn Magn Mater* **127** L261-L266 (1993)

87 D M Edwards, J Mathon and R B Muniz *Phys Rev B* **50**(21) pp16066-16069 (1994)

88 J Mathon, M Villeret, R B Muniz, J d' Albuquerque e Castro and D M Edwards *Phys Rev Lett* **74**(18) pp3696-3699 (1995)

89 J d' Albuquerque e Castro, J Mathon, M Villeret and A Umerski *Phys Rev B* **53**(20) ppR13306-R13309 (1996)

90 J E Ortega and F J Himpsel *Phys Rev Lett* **69**(5) pp844-847 (1992)
J E Ortega, F J Himpsel, G J Mankey and R F Willis *Phys Rev B* **47**(3) pp1540-1552 (1993)

91 P Bruno *J Magn Magn Mater* **121** pp248-252 (1993)

92 K B Hathaway and J R Cullen *J Magn Magn Mater* **104-107** pp1840-1842 (1992)

93 J Barnas *J Magn Magn Mater* **111** ppL215-L219 (1992)

94 P Bruno *Europhys Lett* **23** p615 (1993)

95 A Bounouh, P Beauvillain, P Bruno, C Chappert, R Megy, P Veillet *Europhys Lett* **33**(4) pp315-320 (1996)

96 D M Edwards, J M Ward and J Mathon *J Magn Magn Mater* **126** pp380-383 (1993)

97 J C Slonczewski *J Magn Magn Mater* **126** pp374-379 (1993)

98 J C Slonczewski *J Appl Phys* **73**(10) pp5957-5962 (1993)

99 C J Guiterrez, R Selestino, R A Mayanovic and G A Prinz *J Appl Phys* **81**(8) pp5352-5354 (1997) and references therein

100 J C Slonczewski *Phys Rev Lett* **67**(22) pp3172-3175 (1991)

101 E F Shender and P C W Holdsworth *Phys Rev Lett* **76**(14) pp2583-2586 (1996)

102 B Heinrich, Z Celinski, J F Cochrane, A S Arrott, K Myrtle and S T Purcell *Phys Rev B* **47** p5077-5089 (1993)

103 E C Stoner and E P Wohlfarth *Philos Trans Roy Soc London* **A240** pp599-642 (1948) and recently reprinted in *IEEE Trans Mag* **27** pp3475-3518 (1991)

104 C Kittel *Phys Rev* **70**(11&12) pp965-971 (1946)

105 M S Cohen, in *Thin Film Phenomena* by K L Chopra McGraw-Hill, New York (1969) pp659-666

106 T Beier, H Jahrreiss, D Pescia, Th Woike and W Gudat *Phys Rev Lett* **61**(16) p1875-1877 (1988)

107 M Stampanoni, A Vaterlaus, M Aeschlimann and F Meier *Phys Rev Lett* **59**(21) p2483-2485 (1987)

108 C Liu, E R Moog and S D Bader *J Appl Phys* **64**(10) p5325-5327 (1988)

109 H P Oepen *J Magn Magn Mater* **93** pp116-122 (1991)
110 D B Dove *Bell Sys Tech J* **46** pp1527-1559 (1967)
111 A Yelon, J R Asik and R W Hoffman *J Appl Phys* **33**(3) pp949-954 (1962)
112 C M Williams *J Appl Phys* **39** pp4741-4744 (1968)
113 M S Cohen, E E Huber, G P Weiss and D O Smith *J Appl Phys* **31**(5) pp291S-292S
114 H Ono, M Ishida, M Fujinaga, H Shishido and H Inaba *J Appl Phys* **74**(8) pp5124-5128 (1993)
115 W Andrā, Z Màlek, W Schüppel and O Stemme *J Appl Phys* **31** pp442-443 (1960)
116 A A Hirsch, E Ahilea, and N Friedman *Phys Lett* **28A** pp763-764 (1969)
117 J C Slonczewski, in *Magnetism* (ed. G T Rado and H Suhl) vol 1 Academic Press, New York (1963) p205-242
118 L Néel *J Phys Radium* **15**(4) p225-239 (1954)
119 A J Freeman and R Wu *J Magn Magn Mater* **100** pp497-514 (1991)
120 F J A den Broeder, W Hoving and P J H Bloemen *J Magn Magn Mater* **93** pp562-570 (1991)
121 B Heinrich and J F Cochrane *Advan Phys* **42** pp523-639 (1993)
122 P J H Bloemen, H W van Kesteren, H J M Swagten and W J M de Jonge *Phys Rev B* **50**(18) pp13505-13514 (1994)
123 V V Ustinov, N G Bebenin, L N Romashev, V I Minin, M A Milyaev, A R Del and A V Semerikov *Phys Rev B* **54**(22) pp15958-15966 (1996)
124 J-F. Bobo, B. Baylac, L. Hennet, O. Lenoble, M. Piecuch, B. Raquet and J-C. Ousset, J. Magn. Magn. Mater. **121**, 291 (1993).
125 J-F Bobo, L Hennet and M Piecuch *Europhys Lett* **24**(2) pp139-144 (1993)
126 S N Okuno and K Inomata *Phys Rev Lett* **70**(11) pp1711-1714 (1993)
127 S S P Parkin, C Chappert and F Herman *Europhys Lett* **24**(1) pp71-76 (1993)
128 Q Leng, V Cros, R Schäfer, A Fuß, P Grünberg and W Zinn *J Magn Magn Mater* **126** pp367-373 (1993)
129 P Bruno, J Kudrnovský, V Drchal and I Turek *Phys Rev Lett* **76**(23) pp4254-4257 (1996)
130 Y Saito, K Inomata and K Yusu *Jpn J Appl Phys* **35**pt2(1B) ppL100-L103 (1996)
E E Fullerton and S D Bader *Phys Rev B* **53**(9) pp5112-5116 (1996)
131 S Toscano, B Briner, H Hopster and M Landolt *J Magn Magn Mater* **114** ppL6-L10 (1992)
B Briner and M Landolt *Phys Rev Lett* **73**(2) pp340-343 (1994)
132 P Bruno *Phys Rev B* **49**(18) pp13231-13234 (1994)
133 P Bruno *Phys Rev B* **52**(1) pp411-439 (1995)
134 H Fujiwara and M R Parker *J Magn Magn Mater* **135** ppL23-L29 (1994)
135 e.g. W.F. Egelhoff *et al. J Appl Phys* **79**(8) pp.5277-5281 (1996)
136 P. Panissod, J.P. Jay, C. Mény, M. Wójcik and E. Jedryka, *Hyperfine interactions* 97/98 (1996) pp.75-98
137 E. Jedryka, M. Wójcik, S. Nadolski, D.J. Kubinski and H. Holloway, E-MRS meeting, Strasbourg France (1996).
138 S S P Parkin, R Bhadra, K P Roche *Phys Rev Lett* **66**(16) pp2152-2155 (1991)
139 D H Mosca, F Petroff, A Fert, P A Schroeder, W P Pratt Jr and R Loloee *J Magn Magn Mater* **94** ppL1-L5 (1991)
140 M E Tomlinson, R J Pollard, D G Lord and P J Grundy *J Magn Magn Mater* **111** pp79-82 (1992)
141 R J Pollard, M J Wilson and P J Grundy *J Magn Magn Mater* **146** ppL1-L4 (1995)
R J Pollard, M J Wilson and P J Grundy *J Magn Magn Mater* **151** pp139-144 (1995)

142 M Suzuki, Y Taga, A Goto & H Yasuoka *J Mag Mag Mat* **126** pp495-497 (1993)

143 S Honda, S Ohmoto, R Imada and M Nawate *J Magn Magn Mater* **126** pp419-421 (1993)

144 B K Tanner, D E Joyce, T P A Hase, I Pape and P J Grundy, *Adv X-ray Analysis* **40** (1997) in press

145 D M Edwards, J Mathon and R B Muniz *Phys Rev B* **50**(21) pp16066-16069 (1994)

146 Z Q Qiu, J Pearson, and S D Bader *Phys Rev B* **46**(13) pp8659-8662 (1992)

147 P J H Bloemen, M T Johnson, M T H van de Vorst, R Coehoorn, J J de Vries, R Jungblut, J aan de Stegge, A Reinders, and W J M de Jonge *Phys Rev Lett* **72**(5) pp764-767 (1994)

148 S N Okuno and K Inomata *Phys Rev Lett* **72** 1553 (1994)

149 R Schad, P Beliën, J Barnas, G Verbanck, C D Potter, G Gladyszewski, V V Moshchalkov and Y Bruynseraede *J Magn Magn Mater* **156** p341 (1996)

150 Y Kamiguchi, K Saito, H Iwasaki, M Sahashi, M Ouse & S Nakamura *J Appl Phys* **79**(8) pp6399-6401 (1996)

151 L Néel, *Comptes Rendus Acad Sci* **255**, 1545 and 1676 (1962).

152 A. Yelon, *Physics of Thin Films* (Academic Press, New York, 1971) Vol. 6 pp205-300.
T G S M Rijks, R Coehoorn, J T F Daemen, and W J M de Jonge *J Appl Phys* **76** p1092 (1994)

153 J C S Kools *J Appl Phys* **77** 2993 (1995)

154 D H Mosca, F Petroff, A Fert, P A Schroeder, W P Pratt Jr and R Loloee *J Magn Magn Mater* **94** ppL1-L5 (1991)

155 S S P Parkin, R Bhadra, K P Roche *Phys Rev Lett* **66**(16) pp2152-2155 (1991)

156 H A M van den Berg and G Rupp *IEEE Trans Mag* **30**(2) pp809-811 (1994)

157 T S Plaskett and T R McGuire *J Appl Phys* **73**(10) pp6378-6380 (1993)

158 J. Barnas *J Magn Magn Mater* **111** ppL215-L219 (1992)

159 F Yoshizaki and T Kingetsu *Thin Solid Films* **239** pp229-239 (1994)

160 K Kagawa, H Kano, A Okabe, A Suzuki and K Hayashi *J Appl Phys* **75**(10) pp6540-6542 (1994)

161 M N Varma and R W Hoffman *J Appl Phys* **42**(4) pp1727-1729 (1971)

162 I.S. Jacobs and C.P. Bean, "Fine particles, thin films and exchange anisotropy," in *Magnetism*, vol.III, G.T. Rado and H. Suhl, Eds. New York:Academic, 1963, pp.271-350.

163 J-F Bobo, H Fischer and M Piecuch *Mat Res Symp Proc* **313** pp467-472 (1993)

164] R Mattheis, W Andrã and D V Berkov *J Magn Magn Mater* **154** pp24-28 (1996)

165 M Rühig, R Schäfer, A Hubert, R Mosler, J A Wolf, S Demokritov and P Grünberg *Phys Status Solidi (a)* **125** p635 (1991)

166 S Young, B Dieny, B Rodmacq, J Mouchot and M H Vaudaine *J Magn Magn Mater* **162** pp38-42 (1996)

167 Z J Yang and M R Scheinfein *IEEE Trans Mag* **31** (6) pp3921-3923 (1995)

168 B Rodmacq, K Dumesil, P Mangin and M Hennion *Phys Rev B* **48** (5) pp3556-3559 (1993)

169 G Rupp and H A M van den Berg *IEEE Trans Mag* **29** (6) pp3102-3104 (1993)

170 D H Mosca, F Petroff, A Fert, P A Schroeder, W P Pratt Jr and R Loloee *J Magn Magn Mater* **94** ppL1-L5 (1991)

171 J R Cullen and K B Hathaway *Phys Rev B* **47**(22) p14998-155005 (1993)

172 J d'Albuquerque e Castro, J Mathon, Murielle Villeret and A Umerski *Phys Rev B* **53**(20) pp306-309 (1996)

173 A Barthélémy, A Fert, M N Baibich, S Hadjouj, F Petroff, P Etienne, R Canabel, S Lequienm F Nguyen van Dau and G Creuzet *J Appl Phys* **67**(9) pp5908-5913 (1990)

174 C J Gutierrez, J J Krebs, M E Filipowski and G A Prinz *J Magn Magn Mater* **116** ppL305-L310 (1992)

175 Z Celinski, B Heinrich and J F Cochran *J Magn Magn Mater* **145** ppL1-L5 (1995)

176 M L Yan, W Y Lai, L Yin and S H Liou *J Appl Phys* **81** (8) pp4782-4787 (1997)

177 Z Zhang, L Zhou, P E Wigen and K Ounadjela *Phys Rev B* **50** (9) pp6094-6112 (1994)

178 N Persat and A Dinia *Phys Rev B* **56**(5) pp2676-2679 (1997)

179 Z Q Qiu, J E Mattson, C H Sowers, U Welp, S D Bader, H Tang and J C Walker *Phys Rev B* **45**(5) pp2252-2257 (1992)

180 R Navarro and L J Dejongh *Physica B+C* **98B** pp1- (1979)

181 H A Brown *Phys Rev B* **4**(1) pp115-121 (1971)

182 C Chesman, A Azevedo, S M Rezende, F M de Aguiar, X Bian and S S P Parkin *J Appl Phys* **81** (8) pp3791-3793 (1997)

183 H Kubota, S Ishio, T Miyazaki and Z M Stadnik *J Magn Magn Mater* **129** pp383-388 (1994)

184 D J Kubinski and H Holloway *J Appl Phys* **82**(1) pp322-325 (1997)

185 W F Egelhoff Jr, and D A Steigerwald *J Vac Sci Tech* **A7**(3) pp2167-2173 (1989)

186 M H Read and C Altman *Appl Phys Lett* **7** p51 (1965)

187 W F Egelhoff Jr, P J Chen, C J Powell, M D Stiles, R D McMichael, J H Judy, K Takano and A E Berkowitz (preprint 1997)

188 M T Johnson, P J H Bloemen, F J A den Broeder and J J de Vries *Rep Prog Phys* **59** pp1409-1458 (1996)